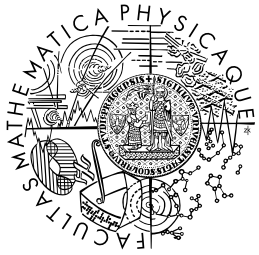

FACULTY
OF MATHEMATICS
AND PHYSICS
Charles University

MASTER THESIS

Jan Dittrich

Investigation of deformation mechanisms in textured magnesium alloy by advanced in-situ methods

Department of Physics of Materials

Supervisor of the master thesis: RNDr. Peter Minárik, Ph.D.

Study programme: Physics

Study branch: Physics of Condensed Matter and Materials

Prague 2021

I declare that I carried out this master thesis independently, and only with the cited sources, literature and other professional sources. It has not been used to obtain another or the same degree.

I understand that my work relates to the rights and obligations under the Act No. 121/2000 Sb., the Copyright Act, as amended, in particular the fact that the Charles University has the right to conclude a license agreement on the use of this work as a school work pursuant to Section 60 subsection 1 of the Copyright Act.

In ..... date ....

Author's signature

There are many people to whom I am grateful for their help in the endeavour leading to this thesis.

First of all, I would like to thank my supervisor, RNDr. Peter Minárik, PhD., for his patient guidance, great advice, and the overall positive and motivating role in all of my efforts throughout the last three years. I would also like to thank RNDr. Gergely Farkas, PhD., for the neutron diffraction and acoustic emission measurements presented in this thesis, as well as his patience during the socially distanced explaining of the data processing. Many thanks also belong to RNDr. Daria Drozdenko, PhD. and RNDr. Peter Harcuba, PhD., for their help with the in-situ EBSD experiments and to RNDr. Michal Knapek, PhD., for his help with the high-speed camera experiments. I would also like to express my gratitude to the whole community of the Department of Physics of Materials, Charles University, for creating an inspirational and supportive working environment.

Furthermore, I would like to appraise the never-ending and unconditional support from my close ones with a special mention for my partner, Julie. From the bottom of my heart, thank you all for making this happen.

Finally, I would like to acknowledge the financial support of the Grant Agency of Charles University in the form of project no. 1172120.

Title: Investigation of deformation mechanisms in textured magnesium alloy by advanced in-situ methods

Author: Jan Dittrich

Department: Department of Physics of Materials

Supervisor: RNDr. Peter Minárik, Ph.D., Department of Physics of Materials

Abstract: This thesis aims to investigate the correlation between texture and the activation of particular deformation mechanisms during the deformation of a rolled magnesium alloy AZ31. A combination of advanced in-situ techniques, providing complementary information about the processes within the material during its deformation, was employed to achieve this goal.

The combination of neutron diffraction and acoustic emission measurements allowed to investigate both rapid and continuous processes related to changes of the material microstructure resulting from its deformation. The in-situ loading of the sample inside the chamber of a scanning electron microscope, coupled with the electron backscatter diffraction analysis, provided more direct observations of the microstructural evolution. Furthermore, the high-speed camera imaging of the deformed sample surface enabled a direct, real-time view of the occurring rapid processes.

The results of the experiments confirmed the anisotropy of the mechanical behaviour of samples oriented diversely with respect to the experimentally detected texture of the rolled metal sheet. Based on the complementary data obtained from the various experimental techniques, this mechanical anisotropy was linked to distinct differences in the preferred activation of individual deformation mechanisms. Moreover, significant inhomogeneities of the plastic deformation within the samples were observed and discussed.

Keywords: magnesium alloys, texture, deformation mechanisms, in-situ

Contents

Introduction

The increasing emphasis on fuel economy and limitation of environmentally harmful emissions in recent years has lead to an increase in demand for lightweight construction materials. Besides the low weight, other characteristics of these desired materials, such as high specific strength (i.e., strength to density ratio), good formability, corrosion resistance, low price, recyclability etc., play an important role in their potential adoption as well. Therefore, it is vital to examine the plastic behaviour of such lightweight materials in order to gain an insight into the relationship between various internal parameters and overall mechanical performance. Only with sufficient understanding of these relations can a lightweight construction material meeting all of the mentioned requirements (and many more) be tailored.

The lightest of structural metals is magnesium, whose density of 1.74 g/cm^3 at room temperature (RT) is about two thirds and one quarter of those of aluminium and steel, respectively, i.e. other widely used structural materials [1]. Apart from the lightweight character, magnesium and its alloys exhibit high specific strength, vibration damping capability, high thermal conductivity and good castability. Therefore, magnesium-based materials are intensively researched for weight-critical applications (e.g. in the automotive and aerospace industry). Despite the qualities mentioned above, its applications are still limited to specific components such as gearbox housings, steering wheels and steering columns, seats etc. [2].

The reason for its limited use is mainly the inherent anisotropy of its mechanical properties and lack of readily activable deformation mechanisms at room temperature, arising from its hexagonal close-packed (hcp) lattice and resulting in poor formability and somewhat limited ductility. Apart from the complicated deformation behaviour, there are several other drawbacks of magnesium and its alloys limiting their application, such as low elastic modulus, high chemical reactivity and limited corrosion resistance [2]. Some of these issues can, however (to a certain degree) be suppressed by suitable alloying or mechanical processing of the material leading to changes in its microstructure.

Magnesium materials having a strong texture (i.e., having a preferential orientation of the crystallites) exhibit a significant anisotropy of the mechanical properties inherited from the nature of the hcp lattice. This is the case of many commercial semi-finished products, such as rolled sheets or extruded rods [3, 4]. Understanding the influence of texture on the mechanical properties of wrought magnesium and its alloys is, therefore, a key to enhancing the mechanical performance and thus enabling their wider practical application.

This work aimed to apply advanced in-situ methods, such as acoustic emission, neutron diffraction or electron backscatter diffraction, to investigate the influence of texture on the activity of various deformation mechanisms, determining the mechanical behaviour of a commonly used rolled magnesium alloy.

1. Theoretical background

1.1 Magnesium and its alloys

Magnesium ($_{12}$Mg) is the second alkali earth metal. Due to its high reactivity, pure elementary magnesium is not found in nature. On the other hand, as a Mg^{2+} cation, it is widespread in the earth's crust (mostly in minerals, such as magnesite, dolomite or carnallite), being the 8th most common element there. It is also ample in seawater as a dissolved mineral with the density of the Mg^{2+} roughly 1,1 kg/m^{-3} [1, 5].

Magnesium has a hcp crystal lattice (Fig. 1.1) with lattice parameters for pure magnesium at 25 °C being $a = 3.210$ Å and $c = 5.211$ Å [6], giving it a c/a ratio of $\approx 1,623$, which is very close to the ideal (in terms of close packing, i.e. obtaining maximally filled volume fraction) value of $\sqrt{8/3} \approx 1,633$ for hcp structure [7]. The most densely packed plane in the hcp structure is the basal (0001) plane. In the three dimensional lattice, the stacking of the hcp basal planes transpires so that the centre points of atoms in the basal planes have only two alternating positions in the stacking sequence (denoted A and B) so that the sequence can be described as ABABAB.... [7].

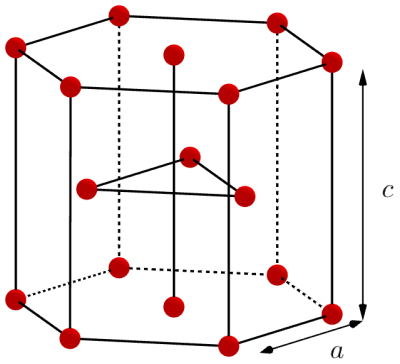

Figure 1.1: Schematic representation of the hcp crystal lattice

Magnesium, being chemically active, tends to react with other metallic alloying elements leading to the formation of intermetallic compounds. The intermetallic phases (which are observed in most of the magnesium alloys) can influence the microstructure, hence altering the properties of the alloy. The most common effects of alloying, enhancing the mechanical properties, are solid solution and precipitation hardening [1, 8].

There exists a globally used system for the designation of magnesium alloys. In this system, the letters indicate the dominant alloying elements and are followed by numbers indicating the wt. % of the corresponding elements rounded to the nearest whole number [9]. Using this designation system, the most common magnesium alloys with increased specific strength compared to pure magnesium are the AZ (wrought applications) and AM (die-casting applications) alloys, where

the main alloying elements are aluminium (A), zinc (Z) and manganese (M) [10]. The material used in this thesis is part of the AZ alloy family; specifically, it is the AZ31 alloy.

1.2 Plastic deformation of magnesium

There are two distinct types of deformation mechanisms, playing key roles in the deformation of magnesium at room temperature – dislocation slip and deformation twinning [11].

1.2.1 Dislocation slip

Dislocation slip denotes the sliding of planes of atoms over one another, resulting in a displacement of one part of the crystal relative to another part. The crystallographic planes, on which the slip occurs (slip planes) and directions of the shear (slip directions) are characteristic for the given type of crystal structure – typically, the slip planes are close-packed (i.e., with the greatest planar density of atoms) and the slip directions are also close-packed (i.e., with the greatest linear density of atoms). The magnitude of the shear displacement is equal to an integral number of interatomic distances, which means that the crystal lattice remains unaltered. The sliding of planes is mediated by the movement of dislocations (this linear crystallographic defect can be interpreted as a boundary between the slipped and unslipped portions of the plane) [11]. Two types of dislocation movement can be differentiated – dislocation glide, where the dislocation moves in a plane defined by the dislocation line and the Burgers vector, and dislocation climb, where the movement is assisted by point defects and occurs in the perpendicular direction to the glide plane [12].

The main slip systems in magnesium are shown in Fig. 1.2 and listed in Tab. 1.1.

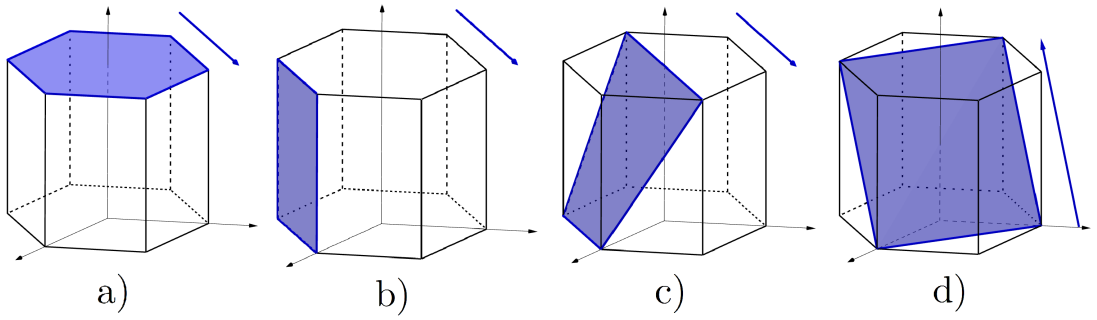

Figure 1.2: Slip systems in hcp metals: a) basal slip, b) prismatic slip, c) 1st order pyramidal slip, and d) 2nd order pyramidal slip. Slip planes are indicated by shading; arrows indicate slip directions.

The preference in activation of a particular deformation mechanism during plastic deformation strongly depends on the c/a ratio of the given hcp metal due to differences in planar atomic densities [14]. Because the c/a ratio of magnesium

Table 1.1: Slip systems in hcp metals [13]

Plane	Slip system	Direction	Number of independent modes
Basal	$\{0002\} < 11\bar{2}0 >$	$< a >$	2
Prismatic	$\{1\bar{1}00\} < 11\bar{2}0 >$	$< a >$	2
1st Pyramidal	$\{1\bar{1}01\} < 11\bar{2}0 >$	$< a >$	4
2nd Pyramidal	$\{11\bar{2}2\} < 11\bar{2}3 >$	$< c + a >$	5

is close to the ideal value, there is no significant preference (based on the planar densities) of either the basal slip (preferred in hcp metals with higher c/a ratios) or slips in the prismatic plane (which are preferred in hcp metals with lower c/a ratios) [13, 14].

Slip, as a result of externally applied force, occurs only when the shear stress acting on the slip plane in the slip direction reaches a specific value, called the critical resolved shear stress (CRSS) [12]. The activation of any given slip system is heavily dependent on the mutual orientation of the applied force, the slip plane and the slip direction. This effect arises from the geometrical aspect of the crystal structure. The relationship between the force exerted on the slip plane, and the CRSS value for the corresponding slip system is described by Schmid's law [15], according to which the stress σ necessary to activate a slip system with a CRSS value of τ_{CRSS} equals:

$$\sigma = \frac{\tau_{CRSS}}{\cos\theta \cos\varphi}, \tag{1.1}$$

where the meaning of angles θ and φ is illustrated by Fig. 1.3. The ratio of shear to applied stress, known as Schmid factor (SF) and denoted m, is then:

$$m = \frac{\tau_{CRSS}}{\sigma} = \cos\theta \cos\varphi \tag{1.2}$$

Since we assume that $\varphi, \theta \in [0°, 90°]$, the value of m for dislocation slip lies between 0 and 0.5. The maximum value corresponds to both $\varphi = \theta = 45°$ and therefore $\omega = 0°$, i.e. the axis of slip plane $\vec{a}$ being parallel to the slip direction $\vec{s}$. The other limit cases, in which $m = 0$, occur either if $\theta = 90°$ (i.e., the slip plane is perpendicular to the loading direction) or $\varphi = 90°$ (i.e., the slip plane is parallel to the loading direction).

The values of CRSS for different deformation mechanisms in magnesium were found to vary significantly. Furthermore, the ratios of the CRSS values for individual deformation mechanisms in polycrystalline magnesium alloys are heavily influenced by the presence of neighbouring grains [16], alloying atoms [17] and are also significantly temperature-dependent [18].

Due to the complexity of CRSS values determination for the specific combination of material and deformation environment, only the following qualitative comparison was taken into account in this thesis. Based on the data presented

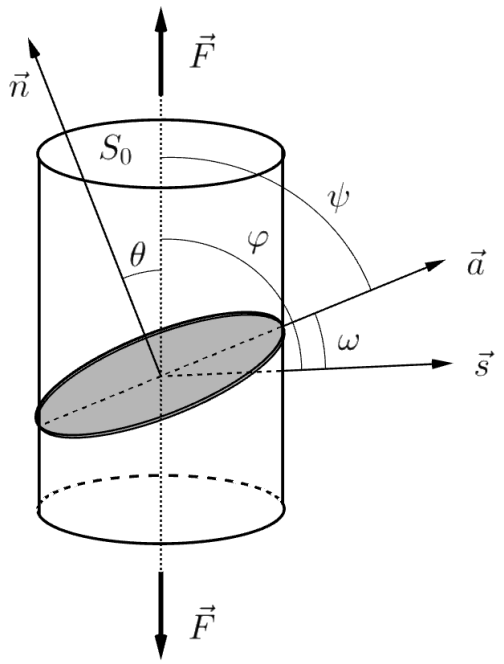

Figure 1.3: Slip conditions in cylindrical Mg monocrystal. $\vec{F}$ denotes the applied force, S_0 the initial diameter of the crystalline cylinder, $\vec{n}$ the normal direction of the slip plane, $\vec{a}$ is the axis of the slip plane, $\vec{s}$ is the slip direction, θ is the angle between the loading direction and the normal of the slip plane, φ denotes the angle between the loading direction and the slip direction and ψ denotes the angle between the loading direction and the axis of the slip plane. The slip plane is indicated by shading.

in [18] (and in accordance with similar approximation in [19]), the magnitudes of the CRSS values of the $\{0002\} < 11\bar{2}0 >$ basal slip, $\{1\bar{1}00\} < 11\bar{2}0 >$ prismatic slip, $\{11\bar{2}2\} < 11\bar{2}3 >$ 2^{nd} order pyramidal slip, $\{10\bar{1}2\} < 10\bar{1}1 >$ extension twinning and the $\{10\bar{1}1\} < 10\bar{1}\bar{2} >$ contraction twinning were considered as follows: basal slip $\sim$ extension twinning $<$ prismatic slip $<<$ 2^{nd} order pyramidal slip $\sim$ contraction twinning.

According to the von Mises criterion [20], at least five independent slip systems are necessary to sustain a homogenous plastic deformation of a polycrystalline material. The easily activated basal slip system, however, provides only two independent slip systems. Should the prismatic system be activated as well, there are still only four combined independent systems, falling short of meeting the criterion. This is because both of these systems provide elongation only along the $< a >$ direction. To meet the criterion, a mechanism providing elongation in the $< c >$ direction also needs to be activated. The $\{11\bar{2}2\} < 11\bar{2}3 >$ 2^{nd} order pyramidal system has a very high CRSS at RT and is thus very difficult to activate at lower stresses. Another such mechanism (i.e., providing elongation in the $< c >$ direction) is the $\{10\bar{1}2\} < 10\bar{1}1 >$ extension twinning, which, at room temperature, has a significantly lower CRSS value compared to the 2^{nd} order pyramidal system. It is, therefore, extension twinning, which (at RT) most often provides the elongation along the c axis and enables to fulfil the von Mises criterion [13].

1.2.2 Twinning

Twinning represents the second fundamental mechanism providing plastic deformation. It is defined as a reorientation of a part of the crystal lattice in such a manner that the original lattice (called "parent" or "twin parent") and the rotated lattice (called "twin" or "twin daughter") have the same structure but different orientation. The reorientation can be described by a mirror reflection on a defined, so-called twinning plane. This plane is shared by both parent and twin lattices and separates them, forming what is called a twin boundary. Twin boundaries (similarly to grain boundaries) present an obstacle for dislocation motion. Furthermore, the reorientation of grains during twinning may facilitate (or suppress) the activation of slip mechanisms. Considering these aspects, as well as the formation of stress field around the twin, twinning plays an important role in the deformation behaviour, ductility and the hardening capability of the material [21].

Schematic representation of the lattice reorientation during twinning is shown in Fig. 1.4. In Fig. 1.4b) the plane B undergoes a shear displacement relative to plane A. Then, in Fig. 1.4c) the plane C undergoes the same relative shear displacement with respect to plane B and finally, in Fig. 1.4d), the plane D shears relative to plane C, finishing the reorientation. Plane A, along which is the twin lattice mirrored, is the twinning plane.

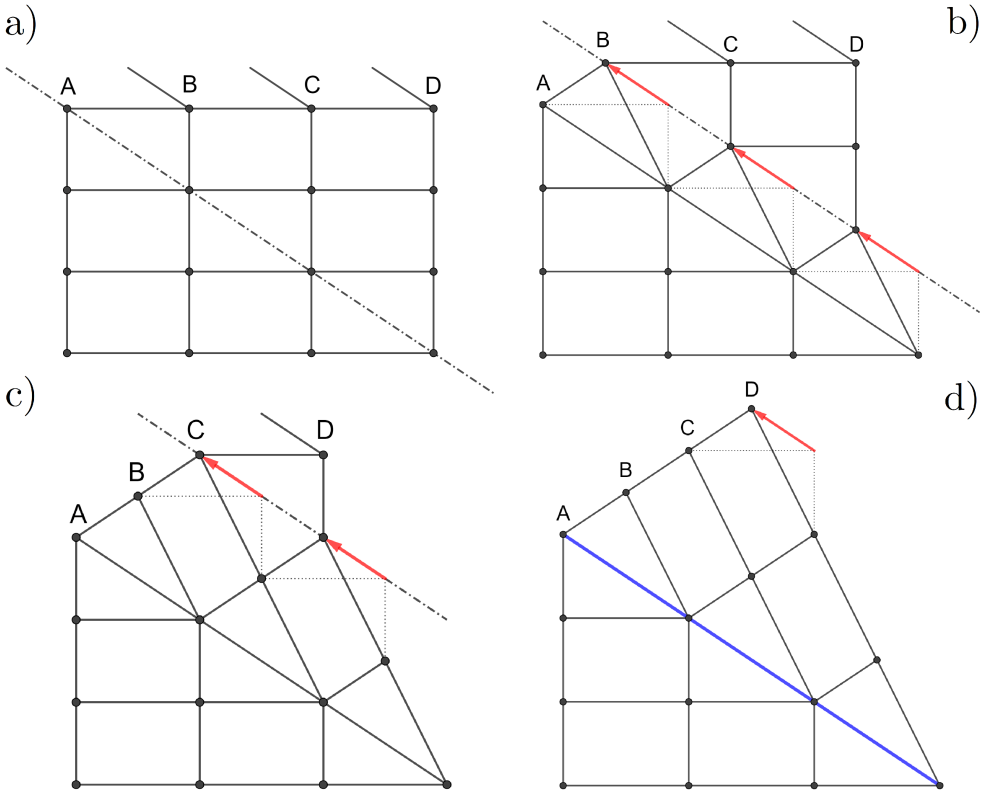

Figure 1.4: Scheme of lattice reorientation during twinning. The shear of planes relative to the twinning plane is marked by red arrows; the twinning plane is marked by a blue line in d).

There are several fundamental differences between deformation twinning and deformation slip which can be summarised as follows [11]:

i) The magnitude of shear displacement during slip varies; however it is always an integral multiple of the Burgers vector magnitude. The dislocation slip occurs only on certain planes. In contrast, during twinning, the shear displacement is, generally speaking, a fraction of the Burgers vector magnitude and every atomic plane shears relative to its neighbour (cf. Fig. 1.4).

ii) Twinning has a polar character, i.e., it is dependent on the orientation of loading. On the contrary, dislocation slip can occur in both directions, which can lead to the activation of the same slip system in the same grain during opposite directions of loading.

iii) While the lattice rotation during slip is gradual, twinning causes an abrupt reorientation of the lattice when the twin daughter is formed.

There exists a formal notation used to describe twinning. In this notation, each deformation twinning mode is described by four invariants, denoted K_1, K_2, η_1 and η_2 (cf. Fig. 1.5). It holds that only two of those (either K_1 and η_2 or K_2 and η_1) are independent. The invariants K_1 and η_1 denote the twinning plane and the shear direction, respectively. The parent and twin lattice can be perceived as mirror images along the plane K_1 (twinning plane) or as a result of a 180° rotation around the axis η_1. The second undistorted plane is the so-called conjugate plane K_2, and the direction in this plane from the centre of the sheared unit hemisphere is called the conjugate shear direction η_2. After the deformation, the plane K_2 rotates to the plane K_2' forming the same angle θ with the twinning plane K_1 as K_2 did. The plane of the shear P is perpendicular to both K_1 and K_2, and in Fig. 1.5, it is the plane of the paper, as is visualised in Fig. 1.6. Since we consider a unit hemisphere, the shear magnitude is $g = 2\cot\theta$ [21, 22].

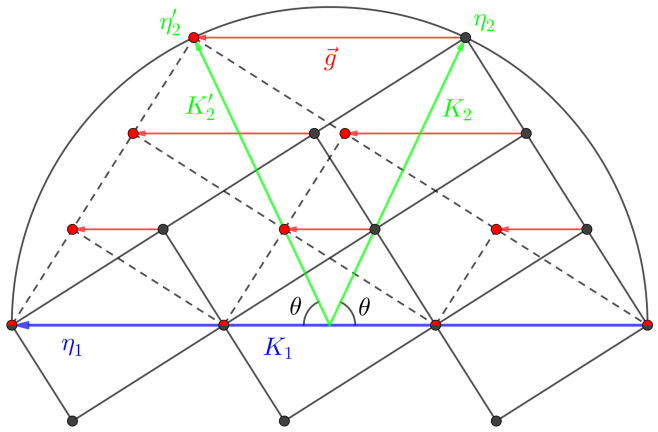

Figure 1.5: Schematic representation of a plane in the sheared unit hemisphere. K_1 is the twinning plane, η_1 the shear direction, K_2 and η_2 are the conjugate planes and the conjugate shear direction, $\vec{g}$ denotes the shear vector and θ the angle between K_1 and K_2.

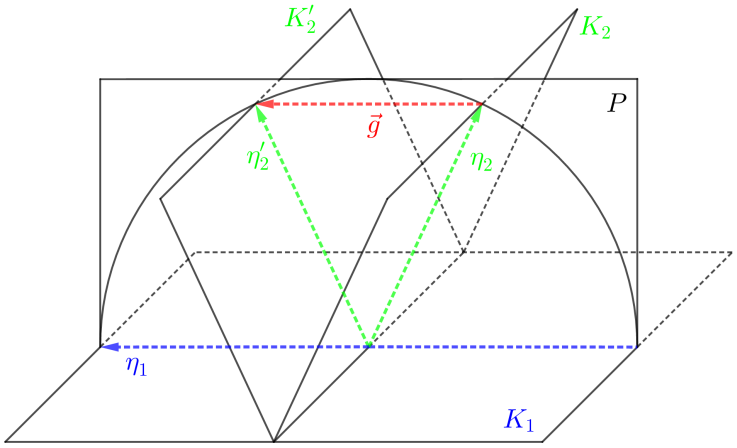

Figure 1.6: Scheme of twinning invariants in space including the shear plane P

The four most commonly observed twinning modes in hcp metals are listed in Tab. 1.2. The most important factors deciding whether the particular mode will be activated or not are the following [21]:

i) The magnitude of shear g has to be small.

ii) The twinning mode needs to require only simple shuffles (i.e., small non-affine displacements of the internal degrees of freedom [23]).

Each twinning mode has a corresponding value of shear magnitude dependent on the c/a ratio (usually denoted as γ), which therefore plays an important role in deformation twinning of various materials. Due to the polar character of twinning, the direction of applying shear stress decides whether the given twinning mode will be activated or not. Twinning modes can thus be divided into two groups – modes causing contraction along the c axis of the parent grain (these are called "contraction twins") and modes causing elongation along the parent grain c axis (these are called "extension twins"). The character of the twins can be determined from the $g(\gamma)$ plot (i.e., the dependency of shear magnitude on the c/a ratio) – tensile twins have a negative slope, compression twins have a positive slope [21].

Table 1.2: Commonly observed twinning modes in hcp metals [13]

K_1	K_2	η_1	η_2
$\{10\bar{1}2\}$	$\{10\bar{1}2\}$	$\pm < 10\bar{1}\bar{1} >$	$\pm < 10\bar{1}\bar{1} >$
$\{10\bar{1}1\}$	$\{10\bar{1}\bar{3}\}$	$< 10\bar{1}\bar{2} >$	$\pm < 30\bar{3}2 >$
$\{11\bar{2}2\}$	$\{11\bar{2}\bar{4}\}$	$\frac{1}{3} < 11\bar{2}\bar{3} >$	$\frac{1}{3} < 22\bar{4}3 >$
$\{11\bar{2}1\}$	$\{0002\}$	$\frac{1}{3} < \bar{1}\bar{1}26 >$	$\frac{1}{3} < 11\bar{2}0 >$

The most commonly observed twinning system in magnesium and its alloys is the $\{10\bar{1}2\} < 10\bar{1}1 >$ extension twinning, depicted in Fig. 1.7. It leads to reorientation of the lattice by ca. 86.3° and extension along the c axis, associated

with tensile strain along it (or compressive strain perpendicular to the c axis). While twinning itself can accommodate strain up to 6.4%, the reorientation of the lattice may increase the likelihood of activation of basal or prismatic slip systems, which can enhance the ability of the material to accommodate plastic strain [21, 24].

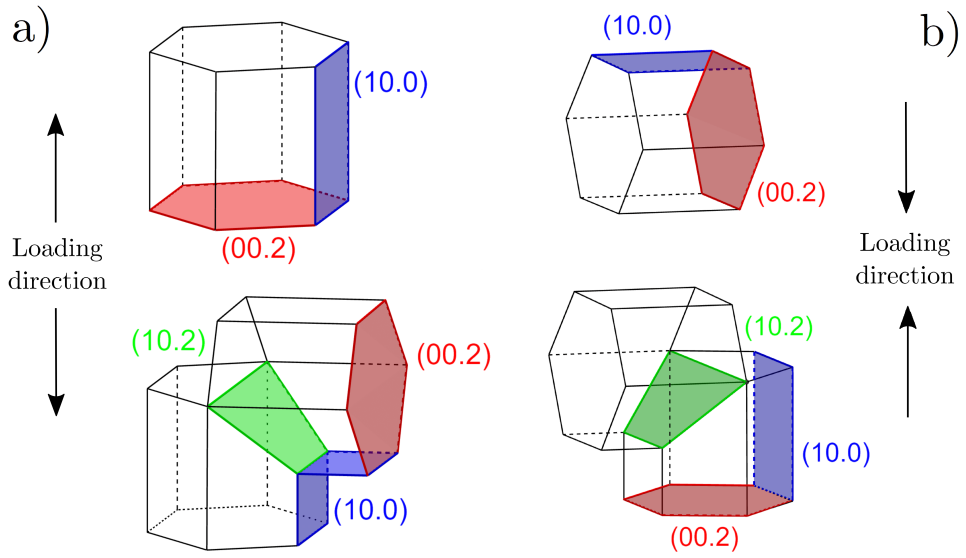

Figure 1.7: $\{10\bar{1}2\} < 10\bar{1}1 >$ extension twinning in a) tension and b) compression

Other twinning modes, e.g. the $\{10\bar{1}1\} < 10\bar{1}2 >$ and $\{10\bar{1}\bar{3}\} < 30\bar{3}2 >$ contraction twins are observed in magnesium as well. They result from an applied compressive strain in the c axis direction and lead to lattice reorientation by ca. 56.2° and 64°, respectively [25, 26]. Another twinning mechanism observed in magnesium and its alloys is the $\{10\bar{1}1\} - \{10\bar{1}2\}$ double twinning, in which case the $\{10\bar{1}1\}$ contraction twinning is followed by the $\{10\bar{1}2\}$ extension twinning in the previously formed twin. The resulting twin is then reoriented by 37.5° with respect to the basal planes of the initial crystal, which may lead to subsequent activation of the basal slip in the twinned material, enhancing the ability of plastic straining [26, 27].

The values of CRSS for twinning systems are obtained similarly to those of slip systems, i.e., by deformation of magnesium single crystals or strongly textured polycrystals [27]. The values for the $\{10\bar{1}2\} < 10\bar{1}1 >$ extension twinning are similar to those of basal slip and are mostly independent of temperature. However, their dependence on grain size is much stronger than those of slip systems (albeit the character of this dependence is the same) [28].

During the twinning process, there are three distinct phases (Fig. 1.8). Nucleation, with which the process starts, occurs due to a local stress state once the projection of stress to the η_1 direction reaches the critical value [29]. In the next phase, the twin rapidly propagates through the grain in the direction of η_1. Once propagation is finished, the twin grows (thickens) in a transversal direction. This growth results from long-range stress states across the grains, which is caused by the movement of twin boundaries in a direction perpendicular to the twinning

plane K_1. It should be noted that the velocity of growth is by several orders of magnitude smaller than the velocity of propagation [30].

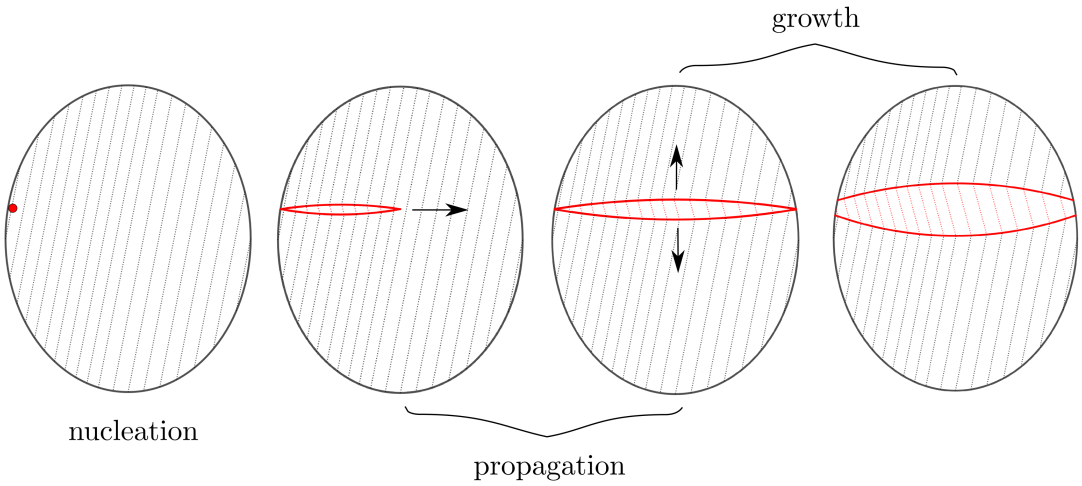

Figure 1.8: Schematic representation of the phases of twinning. The parent grain is black; the twin is marked red, and arrows indicate the direction of movement in each phase.

1.3 Influence of rolling on magnesium alloys

Rolled magnesium sheets present a widespread semi-finished product enabling further processing for numerous applications. Sheet metal-formed parts exhibit better mechanical properties (namely improved strength due to grain refinement) and surface quality without pores compared to die-cast components [31]. During rolling, the material undergoes deformation between the rolls, resulting in a sheet with uniform thickness and a large area, cf. Fig. 1.9.

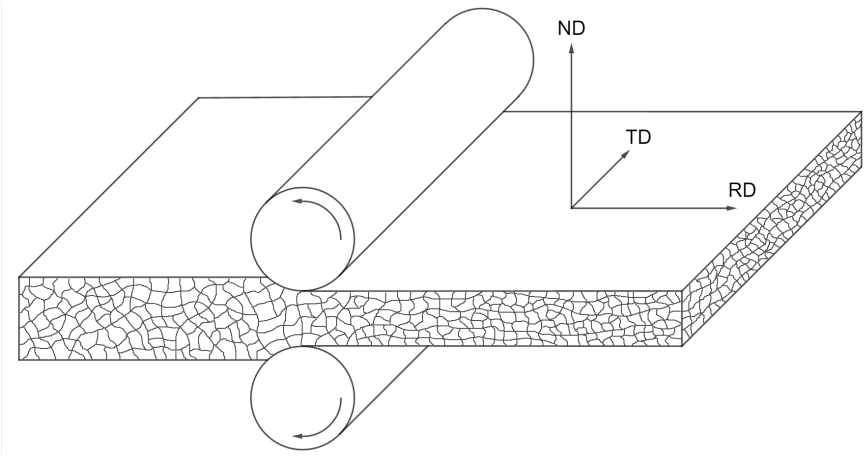

Figure 1.9: Schematic representation of sheet rolling. The significant directions in the produced sheet are marked by arrows and abbreviated. RD stands for rolling direction, TD transversal direction (to RD, within the sheet plane), and ND denotes the normal direction to the sheet plane.

However, in magnesium, due to its hcp lattice, the ductility and formability are somewhat limited (at least compared to cubic metals). This presents a problem for the production and forming processes as well as applications of magnesium sheet-based parts. Numerous studies are, therefore, currently conducted to improve the formability of the magnesium rolled sheets due to a better understanding of the influence of rolling parameters (e.g., initial microstructure, temperature or rolling reduction) on the resulting sheet texture. The choice of magnesium-based sheet alloys is currently very limited, with mostly the AZ31 alloy sheets being commercially available. [31].

Typical magnesium sheets, such as those of the AZ31 alloy, develop a strong texture during rolling. The preferred orientation of the basal planes is parallel to the sheet plane, cf., Fig. 1.10. Due to this texture, the anisotropy of the hcp unit cell translates into a significant anisotropy of mechanical properties in different sheet directions, which negatively affects the formability of the magnesium sheets [32].

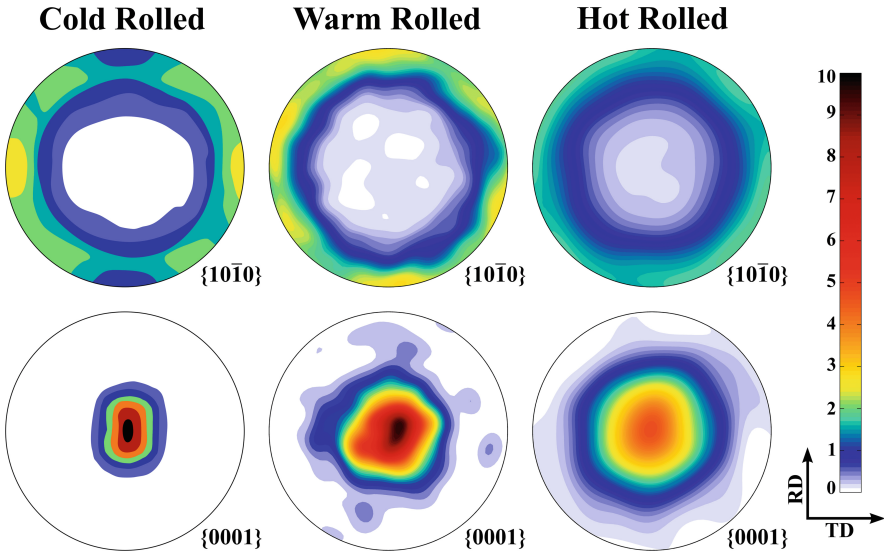

Figure 1.10: The $\{10\bar{1}0\}$ and $\{0001\}$ pole figures of the cold-rolling, warm-rolling and hot-rolling textures in the AZ31 alloy [3]

The rolling texture is heavily influenced by the specific thermomechanical processing routes used during the material preparation. The rolling temperature affects not only the strength of the $\{0001\}$ basal poles but also the distribution of the $\{10\bar{1}0\}$ pole. In the case of the AZ31 alloy, after cold-working (i.e., below ca. 200 °C), the $\{0001\}$ is strongly aligned along the normal direction with a weak splitting along the RD of approximately 5°. The $< 11\bar{2}0 >$ crystal directions then preferentially point along the rolling direction. This cold-working texture is known as the $\{0001\} < 11\bar{2}0 >$ texture [3].

The warm-rolling (i.e., at the temperatures of ca. 200 – 250 °C) of the AZ31 alloy leads to the formation of the so-called $\{0001\} < 10\bar{1}0 >$ texture. In this case, the $\{0001\}$ texture remains strong, and its peak exhibits no apparent splitting. The $\{10\bar{1}0\}$ poles align preferentially along the rolling direction. Steiner et al. [3]

state that the $\{0001\} < 10\bar{1}0 >$ texture commonly appears in as-received commercial AZ31 sheets, which have likely undergone thermomechanical processing similar to warm-rolling.

Hot-rolling (i.e., at temperatures above ca. 250 °C) of the AZ31 leads to weakening of the $\{0001\}$ basal texture and at the same time to a random distribution of the $\{10\bar{1}0\}$ poles within the sheet plane (cf. Fig. 1.10) [3]. The texture of the $\{10\bar{1}0\}$ poles is also significantly influenced by the recrystallisation of the deformed alloy, which occurs readily above 250 °C [33]. The recrystallisation typically leads to a 30 ° rotation of the crystallographic texture around the $< 0001 >$ axis, which means that the $\{0001\} < 10\bar{1}0 >$ texture, resulting from warm-rolling, effectively transforms to the $\{0001\} < 11\bar{2}0 >$ "cold-working" one [3].

2. Aims of the thesis

The main goal of this work is to employ mutually complementing experimental techniques to gain a thorough understanding of the influence of texture on the activity of slip and twinning based deformation mechanisms in a magnesium-based alloy.

The material selected for this study, a rolled magnesium alloy AZ31, was investigated utilising advanced in-situ methods, such as neutron diffraction, acoustic emission, electron backscatter diffraction and high-speed camera imaging.

To achieve the set goal, the following tasks were completed:

- The initial microstructure and texture of the rolled AZ31 alloy were evaluated based on electron backscatter diffraction (EBSD) measurements, providing a sufficient statistical dataset of the studied material.
- A sufficient number of samples with specific orientations was prepared based on the previously determined texture. These samples were suited both for compressive and tensile deformation and machined with respect to their particular application.
- Sets of samples of all selected orientations were deformed both in compression and tension, providing statistical data based on which the mechanical properties were evaluated.
- The neutron diffraction spectra were collected at selected points during the compressive deformation of the samples. Concurrently, the acoustic emission (AE) signal was recorded. The obtained data were analysed with an emphasis on revealing the relation between the parameters of AE events and the evolution of the neutron diffraction spectra.
- A high-speed camera imaging of the sample surfaces was captured during the compressive deformation of a number of specimens with selected sample orientations.
- The EBSD was measured at selected points during the deformation of samples inside the chamber of a scanning electron microscope. An analysis of the obtained data, focusing on the correlation of the results achieved by all the employed techniques and the detected microstructural changes, was performed. A quantitative analysis of the Schmid factor distribution and the twinned volume fraction was also implemented.

3. Experimental methods

3.1 Deformation tests

The data obtained from the deformation test are the time-resolved values of applied load and the position of the loading device frame. The deformation in the elastic region can be described by engineering stress σ and engineering strain ε, defined as follows [12]:

$$\sigma = \frac{F}{S_0}, \tag{3.1}$$

where F is the applied load and S_0 is the initial cross-section of the active zone of the sample; and:

$$\varepsilon = \frac{\Delta l}{l_0} = \frac{l - l_0}{l_0}, \tag{3.2}$$

where l_0 is the initial and l the actual gauge length. The engineering stress and strain are defined only in the elastic region of deformation, where the changes of the cross-section and the length are negligible, and the values are thus considered to be constant. However, in the plastic region of deformation, their changes become significant. To accurately describe the plastic deformation, true stress σ_t and true strain ε_t are introduced using differential terms [12]:

$$d\varepsilon_t = \frac{dl}{l} \tag{3.3}$$

The true strain is then:

$$\varepsilon_t = \int_{l_0}^{l} \frac{dl}{l} = \ln \frac{l}{l_0} = \ln \left(\frac{l_0 + \Delta l}{l_0} \right) = \ln(1 + \varepsilon) \tag{3.4}$$

The true stress is defined as:

$$\sigma_t = \frac{F}{S} = \frac{F}{S_0} \frac{S_0}{S}, \tag{3.5}$$

where S denotes the actual cross-section. Taking the conservation of volume during plastic deformation into account, the expression $\frac{S_0}{S}$ can be expressed as follows:

$$S_0 l_0 = S l \Rightarrow \frac{S_0}{S} = \frac{l}{l_0} = \frac{l_0 + \Delta l}{l_0} = (1 + \varepsilon) \tag{3.6}$$

By combining the result with 3.5 and using equation 3.1, we therefore obtain:

$$\sigma_t = \sigma(1 + \varepsilon) \tag{3.7}$$

Therefore, the response of the material on uniaxial straining and its mechanical properties was interpreted based on the true stress - true strain (often called "flow") curves. During the evaluation of the measurements, the elastic part of the deformation was subtracted.

There are two significant points on the stress-strain curve. The first of them is the yield point, further on denoted as $\sigma_{0.2}$. Its definition is related to the continuous transition between the elastic and plastic part of the deformation, called yielding. The yield point corresponds to the stress, at which the plastic strain after unloading of the material would be 0.2%. In practice, it is obtained as an intersect of the line parallel with the linear part of the curve (corresponding to the elastic region of deformation) shifted along the strain axis by 0.2%.

Beyond the yield point, the stress needed to maintain plastic deformation increases (this phenomenon is called strain hardening) until it reaches the other significant point – the maximum of the flow curve, denoted as $\sigma_{\max}$ and called ultimate tensile (compressive) strength (depending on the mode of deformation). The strain at which $\sigma_{\max}$ is attained is called the uniform strain and denoted ε_u. Beyond the uniform strain, the deformation becomes unstable, the cross-section of the specimen locally rapidly decreases whilst the so-called "neck" is formed. This is shortly afterwards followed by fracture [12].

The deformation tests were used for the quantitative assessment of the mechanical properties of the samples. They were carried out both in compression and tension using sets of four samples machined in all the selected sample orientations. The deformation tests were performed using the Instron 5882 universal testing machine combined with the Blue Hill 2.6 software. The deformation of all samples was performed at room temperature, and the initial strain rate of 10^{-3} s^{-1} was used. The same strain rate was used in all the experiments presented in this thesis to maximise the comparability of the deformation data measured during different experiments. For the evaluation of applied load, a 100 kN capacity load cell was used. The sampling rate of data storing was set to 50 Hz.

3.2 Neutron diffraction and acoustic emission

Combination of the neutron diffraction and acoustic emission techniques enables concurrent investigation of the dynamical processes within the material during its deformation, such as twin nucleation or avalanche-like motion of dislocations (acoustic emission), as well as the effect of more gradual processes in the bulk of the material, such as twin growth (neutron diffraction). These two methods, therefore, complement each other and offer an extensive insight into the mechanisms of the material deformation [34].

3.2.1 Neutron diffraction

The analysis of neutron diffraction spectra can reveal crystallographic changes, which the studied material undergoes during its deformation. This is possible due to the wave-like characteristics of neutrons arising from the wave-particle duality. For the purpose of investigating the atomic arrangement of solids, the wavelength of the utilised radiation needs to be comparable within an order of magnitude with the spacings between the atoms (typically units of Å) [35].

According to the wave theory, the wavelength λ equates to [35]:

$$\lambda = \frac{h}{mv}, \tag{3.8}$$

where h denotes the Planck constant, m the mass of the particle (in this case neutron and thus further denoted m_n) and v its velocity. If we consider so-called thermalised neutrons (i.e., neutrons that underwent a large number of collisions inside a reactor at a given temperature T), then according to the Maxwell-Boltzmann distribution, they have a root-mean-square velocity corresponding to the temperature T:

$$\frac{1}{2}m_n v^2 = \frac{3}{2}k_B T, \tag{3.9}$$

where k_B denotes the Boltzmann constant. Combining the equations 3.8 and 3.9, we obtain the relationship:

$$\lambda = \frac{h}{\sqrt{3m_n k_B T}}, \tag{3.10}$$

This means that, for example, at 100 °C (i.e., 373.15 K), the wavelength of neutrons is approximately 1.3 Å. Due to this fact, beams of neutrons, slowed down by a moderator and extracted from the nuclear reactor, can be utilised to study the structural properties of solid materials [35].

The principle which allows insight into the structure of solids exposed to a beam of neutrons was described by Bragg [36]. The incident neutrons scatter on the periodically spaced lattice planes. The path difference of neutrons scattered coherently and elastically on neighbouring planes is dependent on the interplanar distance d and the angle of incidence θ. When this path difference equals to an integral multiple of their wavelength λ, constructive interference occurs, which is described by the Bragg equation:

$$2d \sin\theta = n\lambda, \tag{3.11}$$

where $n \in \mathbb{N}$ denotes the order of diffraction. The schematic representation of Bragg diffraction is shown in Fig. 3.1.

If the wavelength of the incident neutrons is a known constant (the waves are monochromatic), the interplanar distance can be calculated from the diffraction peak position (i.e., the angle of incidence for which the neutron waves have interfered constructively). The distance d_{hkl} between planes with Miller indices $(hk.l)$ (where the $i = -(h + k)$ index is omitted and marked "." for simplicity) is determined by the formula 3.12 [37]. This allows determining the plane family to which the detected diffraction peak corresponds.

$$\frac{1}{d_{hkl}^2} = \frac{4}{3a^2}(h^2 + k^2 + hk) + \frac{l^2}{c^2}, \tag{3.12}$$

where a and c are the lattice parameters. The difference between the incident and scattered wave vectors $\vec{k_i}$ and $\vec{k_f}$ is called the diffraction vector and is denoted $\vec{Q}$:

$$\vec{Q} = \vec{k_i} - \vec{k_f} \tag{3.13}$$

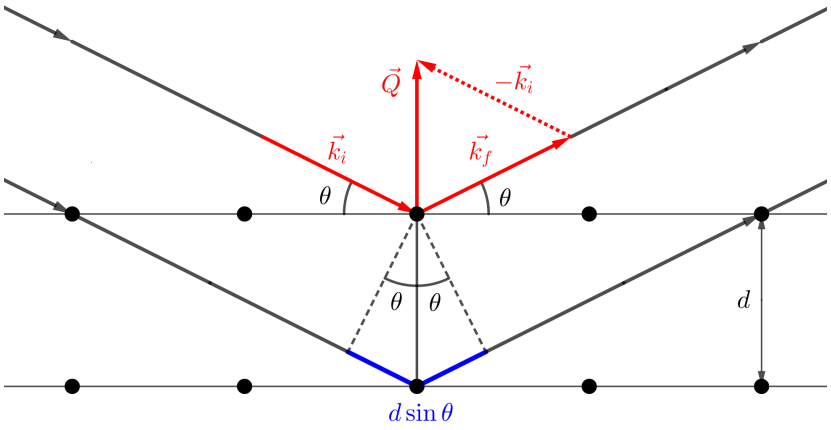

Figure 3.1: Schematic representation of Bragg diffraction on crystallographic planes with interplanar spacing d. Blue segments denote the path difference, while the incident wave vector, scattered wave vector and diffraction vector are coloured red.

$$|\vec{Q}| = \frac{4\pi \sin\theta}{\lambda} \tag{3.14}$$

Diffraction, therefore, provides information about planes perpendicular to the diffraction vector, as is illustrated in Fig. 3.1.

The neutron diffraction spectra are influenced by the presence of internal stresses in the sample. Typically, the internal stresses are classified into three types [38]:

i) Type I stresses, called macrostresses. These stresses are self-equilibrated across the whole sample and are assumed to be continuous across the grain and phase boundaries. They typically arise from macroscopic misfits generated by plastic deformation of the sample or its quenching. The type I stresses lead to shifts of the diffraction peaks.

ii) Type II stresses are self-equilibrated over a scale comparable with grain sizes and are discontinuous across grain boundaries. The origin of type II stresses is related to the different response of individual grains to applied pressure due to their varying elastic and thermal properties. Regarding the neutron diffraction spectra, type II stresses lead to varying degrees of peak shift and peak broadening.

iii) Type III stresses self-equilibrate on scales smaller than grain sizes and originate from misfits such as crystal defects. The type III stresses typically include stresses caused by dislocation stress fields and incoherent interfaces and lead to peak broadening and shape change. Type II and III stresses are collectively called microstresses.

The external loading of the sample leads to lattice strain causing a change of the diffracted angle, as is illustrated in Fig. 3.2. By differentiating of the Bragg

equation 3.11, we obtain the following expression describing the lattice strain for a given grain family $(hk.l)$:

$$\varepsilon_{hkl} = \frac{d_{hkl} - d_{0,hkl}}{d_{0,hkl}} = \frac{\Delta d_{hkl}}{d_{hkl}} = -\cot\theta_{0,hkl}\Delta\theta_{hkl}, \tag{3.15}$$

where ε_{hkl} denotes the lattice strain in question and the values of interplanar distances d, and diffraction angles θ indexed with the subscript 0 correspond to the stress-free state.

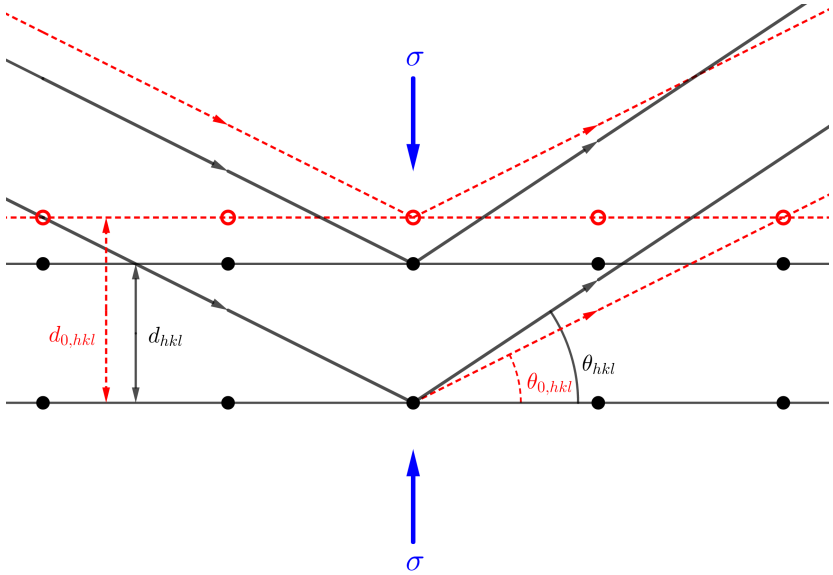

Figure 3.2: Schematic representation of lattice strain under loading. The red-dashed lattice points, planes and rays correspond to the stress-free state, while the black ones correspond to the state under applied stress. The loading direction is marked by blue arrows.

The evolution of lattice strain can be used to investigate the onset of plastic deformation in various orientations (e.g., [39]). In the elastic region of deformation the lattice strain should be linearly dependent on the applied stress following the Hooke's law. The deviation from this linear dependence then marks the onset of plastic deformation for the given grain family. So-called "soft" and "hard" orientations of grain can therefore be differentiated – the dependency of lattice strain on applied stress in the "soft-oriented" grains deviates above the linear line (for example, as a result of suitable orientation for extension twinning mediating plastic deformation) as they undergo plastic deformation and slow their elastic loading, while for the "hard-oriented" grains the curve deviates below the elastic regime line (in order to accommodate the remainder of elastic loading) [40]. The linear dependencies slopes are determined by the values of Young's moduli E. The specific values used in this thesis are those experimentally obtained in the study [41], which investigated samples of the AZ31 alloy oriented in the RD, ND and 45 directions.

The most significant change of the diffraction pattern during plastic deformation mediated by twinning is illustrated in Fig. 3.3. The evolution of the

integrated intensities of particular peaks is induced by the texture evolution during plastic deformation. In this specific study, the neutron diffraction spectra were measured during compressive deformation. The grains oriented favourably for the $\{10\bar{1}2\} < 10\bar{1}1 >$ extension twinning were the ones with their $(10\bar{1}0)$ prismatic planes oriented perpendicular to the loading direction. Once they underwent the twinning process, the prismatic planes in the twinned parts of grains have been reoriented out of the diffraction condition (i.e., they became practically parallel to the diffraction vector $\vec{Q}$). On the other hand, the (0002) basal planes of the twinned parts of grains have moved to the diffraction condition (i.e., perpendicular to $\vec{Q}$), as is illustrated on the right-hand side of Fig. 3.3. This behaviour is caused by the fact that the lattice reorientation, connected with the $\{10\bar{1}2\} < 10\bar{1}1 >$ extension twinning, amounts to 86.3°, which is near 90° and therefore effectively transforms the planes perpendicular to the diffraction vector to parallel positions and vice versa.

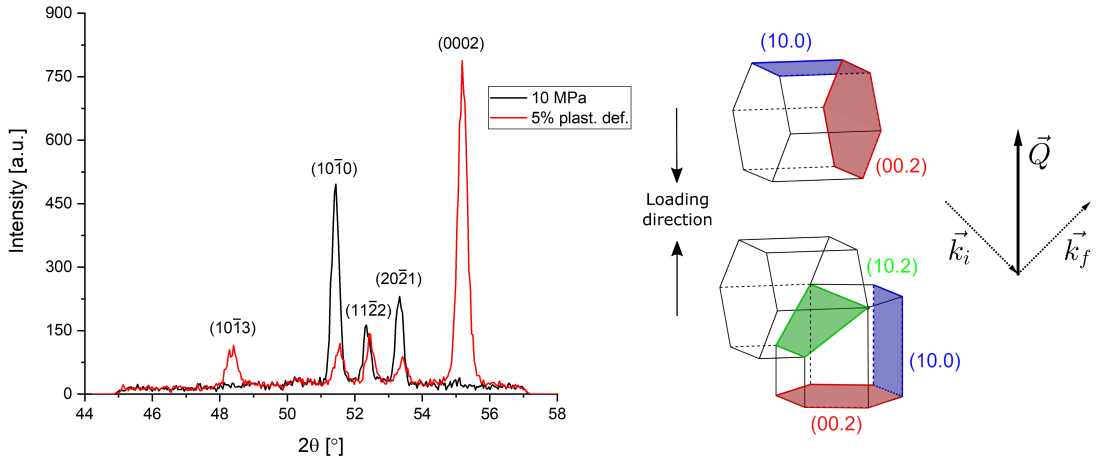

Figure 3.3: Evolution of the diffraction pattern due to extension twinning of the RD sample during compression. The black line represents the diffraction pattern measured at 10 MPa (i.e., within the early stages of elastic deformation). The red line then shows the pattern collected after 5 % of plastic deformation. For illustration, the scheme of extension twinning during compression and the orientation of diffraction vector relative to the crystallographic planes is included.

Therefore, the above-described process leads to a significant decrease in the integrated intensity of the $(10\bar{1}0)$ diffraction peak and, at the same time, an increase in the integrated intensity of the peak corresponding to the (0002) planes. The fraction of the integrated intensities of these two peaks can therefore be used to assess the evolution of the twinned volume fraction within the studied sample during plastic deformation. Similar changes can be expected regarding the $(11\bar{2}0)$ and $(10\bar{1}3)$ intensities, respectively, determined by the $\{11\bar{2}0\}-\{10\bar{1}3\}$ parent-daughter grain relation also resulting from the $\{10\bar{1}2\} < 10\bar{1}1 >$ extension twinning [42].

The elastic scattering of neutrons by atomic nuclei (neutron diffraction) and of X-rays by electrons (X-ray diffraction) can be described by similar equations

based on the same theory. However, there are several important differences between the two techniques leading to differences in the suitability of the two for different experiments [43]. The main advantages of neutron over X-ray diffraction are the following [43, 44, 45]:

- The penetration depth of neutrons is typically 2-3 orders of magnitude higher than that of X-rays (ca. 10 mm compared to 10^{-2} mm). Neutron diffraction technique can therefore be used to obtain statistically significant results even for polycrystalline samples with extensive grain sizes.
- The energy of thermal neutrons with a wavelength of 1 Å is ca. 0.08 keV, much lower than that of X-rays of the same wavelength (ca. 12 keV). This limits possible radiation damage and enables to monitor the changes in internal stresses during loading.
- The scattering amplitudes of neutrons vary irregularly with their atomic number Z, in contrast with X-rays, for which the scattering amplitude grows linearly with the number of electrons (and thus Z). This means that neutron diffraction is better suited for studying systems containing elements with similar atomic numbers or very light elements.
- The scattering amplitude of neutrons is independent of the diffraction angle θ, whereas for X-rays, it significantly decreases for higher θ values.

The most notable disadvantage of neutrons compared to X-rays are the longer acquisition times during diffraction experiments, caused by the lower luminosity of the neutron sources. This, however, does not cause any significant problems in the application for this study and neutron diffraction is, therefore, the preferred technique of the two in this case.

3.2.2 Acoustic emission

The acoustic emission phenomenon is defined as transient elastic waves within the material arising from a rapid release of localised stress energy [46]. The sources of AE are related to dynamic changes in the material structure (e.g. dislocation motion, twinning, cracking or various martensitic transformations) and are activated by external forces. The elastic waves travel through the material to the surface, where their perpendicular component can be detected by a piezoelectric device, transforming the surface displacement to an electric signal ("AE signal"), which is amplified and further processed by measuring devices. In this thesis, the AE technique was employed to study signals originating from twinning and the collective ("avalanche-like") motion of dislocations [47].

Various AE signals can be generally separated into two distinct categories – burst and continuous emission. Continuous emission occurs when many different sources simultaneously generate the elastic waves, and the separation of individual pulses is impossible. In this case, the amplitude of the signal remains above the threshold level (cf. Fig. 3.5) for an extended period of time. Continuous emission is closely related to plastic deformation mediated by dislocation slip (generation of dislocations by Frank-Read sources, their mutual interaction, piling

up at obstacles and subsequent releasing [46]). The burst type of AE signal, on the other hand, consists of distinct, well-separated pulses characterised by a rapid decay of the signal amplitude. This sort of signal occurs due to instabilities in plastic deformation, most notably (for the purposes of this thesis) as a result of twin nucleation (the twin growth is not rapid enough to be detectable) [48, 49]. Examples of both emission types are shown in Fig. 3.4.

There are two basic approaches to the processing of the AE signal. In the hit-based approach, each AE event (i.e., a single dynamic process during which a certain amount of energy is released) is processed individually in real-time. The alternative approach is based on data streaming. This technique consists of recording the entire signal and its ex-post parametrisation, which enables modifying the event parametrisation based on inspection of the recorded signal to optimise it for the specific experimental setup. On the other hand, this approach leads to large quantities of recorded data and time-consuming post-processing. [50]. It is thus applicable only when the measurement does not last too long. In this thesis, however, the AE signal is recorded concurrently with acquiring the neutron diffraction spectra. This process is rather long, and the whole experiment spans across multiple hours. The hit-based approach is, therefore, the only feasible option in this case.

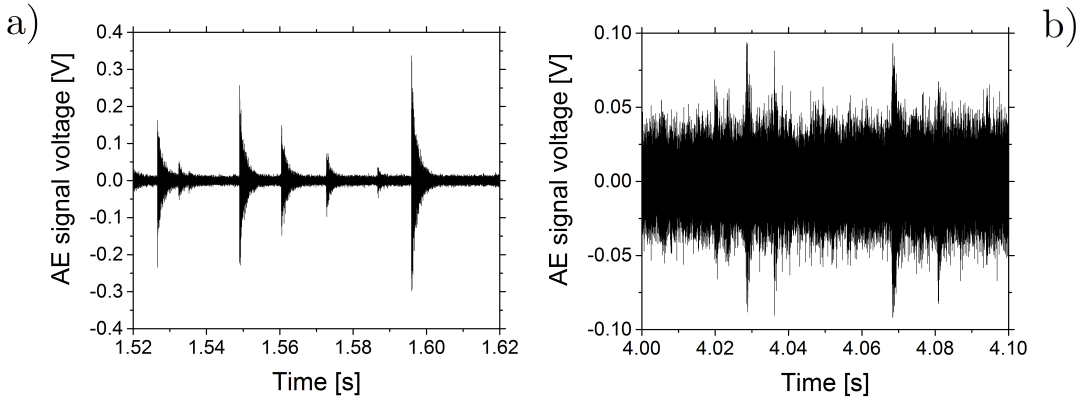

Figure 3.4: Examples of AE signal types – a) burst emission and b) continuous emission [50]

The hit-based approach relies on a set of parameters, which are preset before the experiment in order to define potential AE events. These parameters are listed below, along with Fig. 3.5 providing their illustration.

- Threshold level – once this voltage is exceeded, the AE event is considered to have started.
- Hit definition time (HDT) – the event is considered to have ended if the signal does not exceed the threshold voltage for this amount of time.
- Hit lockout time (HLT) – marks the time period during which no new events are detected. This serves to avoid echoes of the original event.

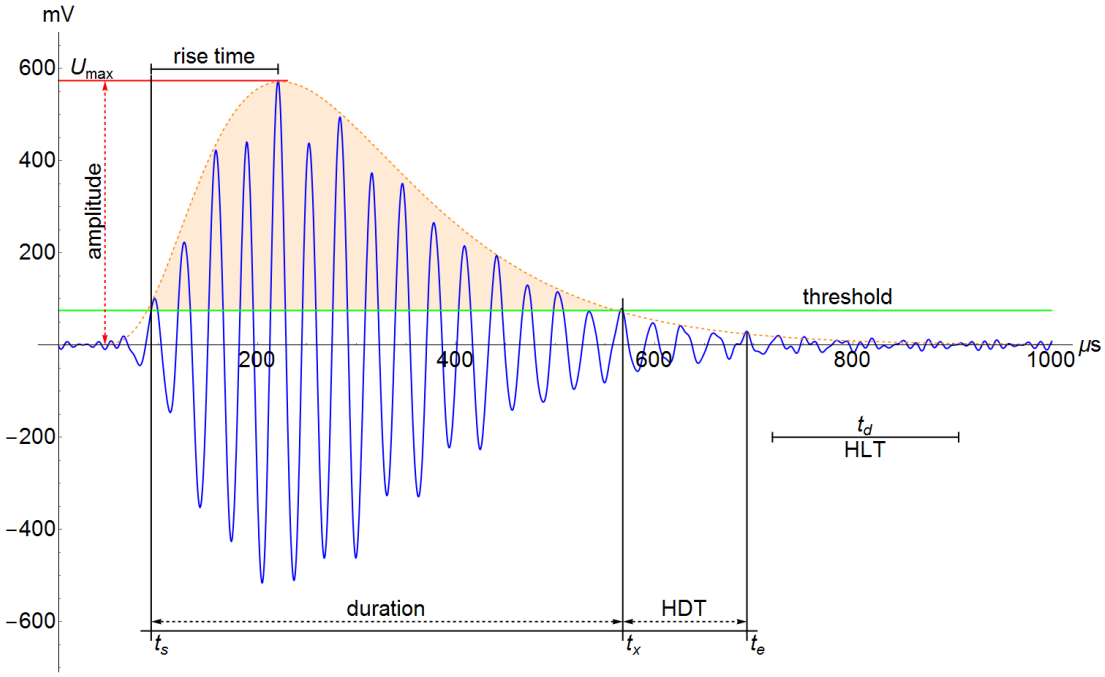

Figure 3.5: Parametrisation of the AE signal [51]

The HLT is often called “dead time”. The sum of HDT and HLT marks the minimal time difference between the end of the previous AE event and the start of a new one. In some cases, the maximum duration of an AE event is also set. The choice of the threshold level, HDT and HLT influences the identification of AE events and, therefore, the resulting statistical distribution of their characteristics [50, 51].

The most important parameters characterising each AE event are the following [51]:

- Amplitude – the maximum voltage during the AE event
- Rise time – the time between the threshold level is first exceeded, and the peak voltage is reached
- Duration – the time difference between the first and last crossing of the threshold level
- Counts – the total number of times the threshold level is crossed during the event
- Count rate – the number of counts per unit time
- Energy – the area under the envelope curve (shaded area in Fig. 3.5)

The AE signal is heavily dependent on the deformation behaviour of the samples and, as such, provides a possibility to analyse the influence of various experimental and material parameters on this behaviour. Examples of such analyses in Mg single crystals and the AZ31 alloy can be found in [52] and [53]. However,

there are drawbacks to the hit-based AE recording. The main problem is caused by the absence of any direct link between the specific source mechanism and the characteristics of the resulting AE signal [51]. In contrast, if the data streaming approach is employed, this problem can be, at least to a certain extent, resolved by applying a spectrum-based analysis (based on the difference in AE waveforms produced by different mechanisms [54]), such as the adaptive sequential k-means procedure [55] (this, however, falls beyond the scope of this thesis). Even if such techniques are adopted, the AE analysis identifies only the preferential deformation mechanism. Other mechanisms may also be active but end up obscured by the dominant one.

The analysis of the acoustic emission signal, therefore, provides a sensitive and non-destructive method of insight into the deformation behaviour. However, to avoid uncertainty in conclusions, the AE analysis should be combined with other experimental methods providing more direct observations.

3.2.3 Experimental setup

The neutron diffraction experiments coupled with acoustic emission monitoring were performed in-situ during compressive deformation of the AZ31 magnesium alloy samples at the Neutron Physics Laboratory of the Nuclear Physics Institute in Řež. The biaxial diffractometer TKSN-400 installed in the HK-9 horizontal neutron channel of the LVR-15 research reactor was used in this study. The scheme of the diffractometer is shown in Fig. 3.6, together with the scheme illustrating the neutron optics of the TKSN-400 diffractometer. The axial geometry (i.e., the parallel orientation of the diffraction vector and loading axis) was used for this study. The TKSN-400 diffractometer is optimised to study internal stresses in polycrystalline solids and provides a resolution $\frac{\Delta d}{d}$ of $\approx 2 \times 10^{-3}$.

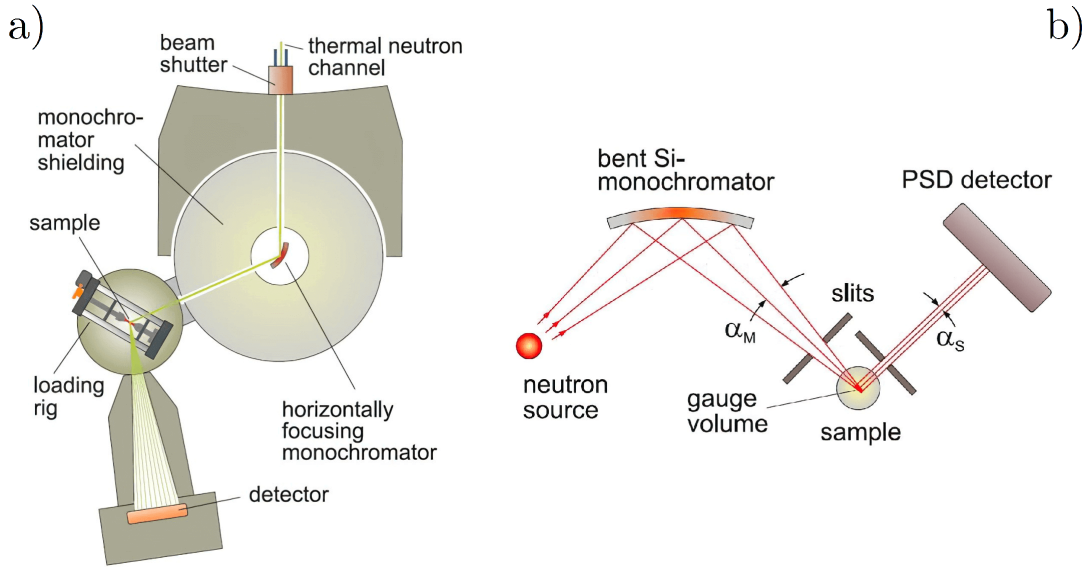

Figure 3.6: a) Scheme of the biaxial TKSN-400 diffractometer, b) scheme of the neutron optics used in the TKSN-400 diffractometer [56]

The diffracted neutrons had a wavelength of 2.4 Å, which was selected by a bent Si-monochromator. In this monochromator, only the neutrons scattered on the (220) planes are selected. The curvature then helps to focus the monochromatised beam on the sample, which improves the angular resolution [56]. The neutron flux was approximately 10^5 particles per cm^2/s.

The diffractometer was equipped with a 2D He positive sensitive detector (detecting the excess energy originating from the reaction: $n + {}^3\mathrm{He} \rightarrow p + 3\mathrm{H} + 0.77\,\mathrm{MeV}$ [56]) with an active window of $220 \times 220\,\mathrm{mm}^2$ and the spatial resolution of $0.8 \times 0.8\,\mathrm{mm}^2$. The detector was set up so that its centre was in the position $2\theta = 51°$, which enabled detection of diffraction spectra within the angular range of ca. 44.2° to 58°. The slit between the monochromator and the sample selected a gauge volume of $3 \times 5 \times 6\,\mathrm{mm}^3$ within the sample. For better resolution, a $3 \times 5\,\mathrm{mm}^2$ slit was placed between the studied sample and the detector.

The loading of the samples was performed by an uni-axial loading rig with a maximum force of $\pm 100\,\mathrm{kN}$. The deformation of each sample was stopped at preselected values of stress (in stress-control mode) or strain (in strain-control mode) to collect the diffraction patterns. The data acquisition time in each measured point was set to 1 hour. The strain was measured by an extensometer. The specific setup of the experiment is shown and described in Fig. 3.7.

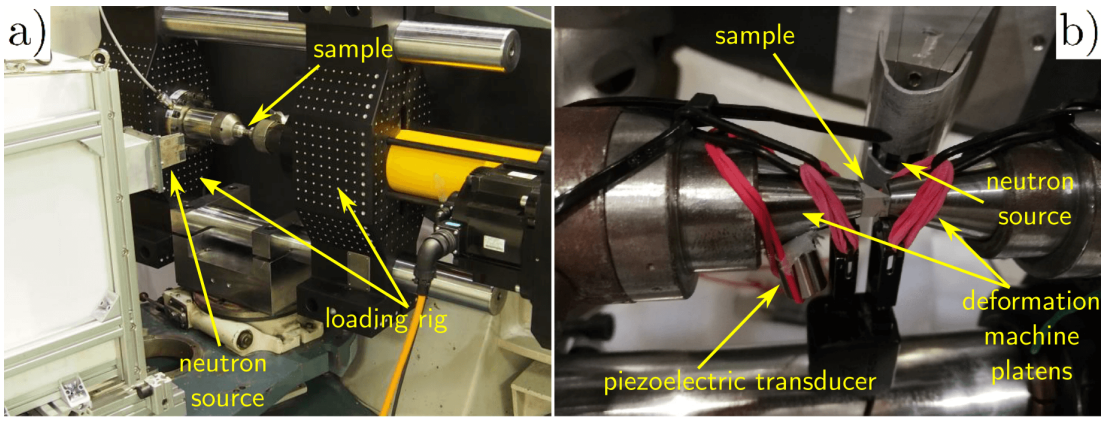

Figure 3.7: a) The uniaxial loading rig [56], b) detail of the sample mounting (here it is shown after breaking of the sample) and the AE measuring device

During the experiments, it was revealed that the load cell in the loading rig was miscalibrated. The subsequent calibration experiments with known loads unveiled a discrepancy between the actual and indicated load (denoted F_a and F_i respectively), exhibiting an exponential decrease in their ratio. The experimentally obtained values of this ratio were therefore fitted with the exponential decay function (using the Origin 2019 software):

$$y = y_0 + Ae^{-\frac{x}{t}}, \tag{3.16}$$

where y_0 denotes the asymptote value, while A and t determine the shape of the curve. The fitted values, together with the approximate values of load corresponding to yields stresses in different sample orientations (aiming to illustrate

the magnitude of the discrepancy with regard to the stage of deformation) are shown in Fig. 3.8.

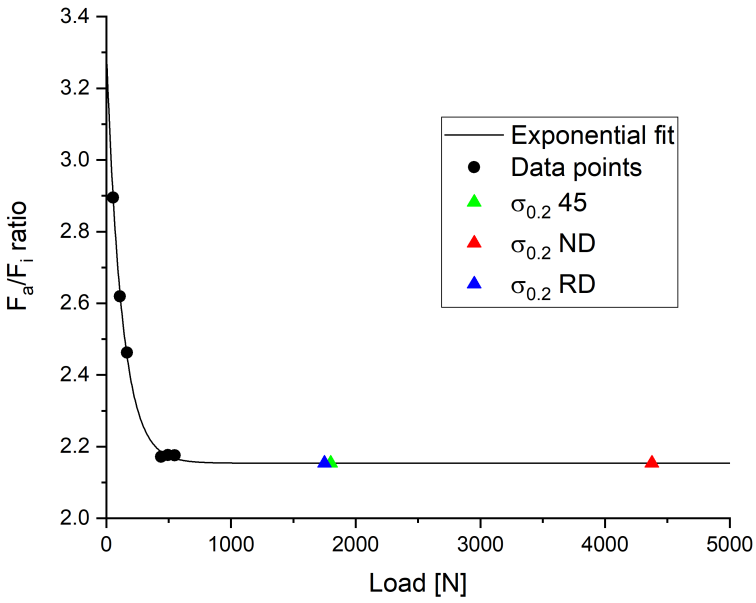

Figure 3.8: The exponential fit of the ratio between the actual and indicated load by the load cell. The respective yield points for the sample orientations 45, ND and RD are also displayed.

The diffraction data were analysed by the single peak fitting method using the Origin 2019 software. Based on the symmetrical and moderately broad profiles of the peaks, a simple Gauss function was fitted to the peaks:

$$y = y_0 + \frac{A}{w\sqrt{\frac{\pi}{2}}} e^{-2\frac{(x-x_c)^2}{w^2}}, \tag{3.17}$$

where y_0 denotes the offset (caused by the background radiation), x_c the centre of the peak, w the width of the peak and A its area. The full width at half maximum (FWHM) is then equal to $\sqrt{2\ln(2)}w$. The Gaussian profile tends to fit the peak profiles well unless the broadening due to Type III internal stress (mainly due to increased dislocation density) is significant. In that case, the shape tends to be more Lorenzian-like [56].

During the loading interrupted by the neutron diffraction spectra collection, the acoustic emission was concurrently monitored. The schematic representation of the experimental setup used to acquire and process the AE signal is shown in Fig. 3.9. The piezoelectric transducer transforms the oscillations of the sample surface, caused by the mechanical waves, to an electric signal. The signal is preamplified and enters the processing unit, where it is amplified, converted from analogue to digital and analysed. Once processed, the signal is then passed to the computer equipped with a corresponding, specialised software.

The acoustic emission data were collected during interrupted compressive loading of samples of all selected orientations. During the interruptions, the neu-

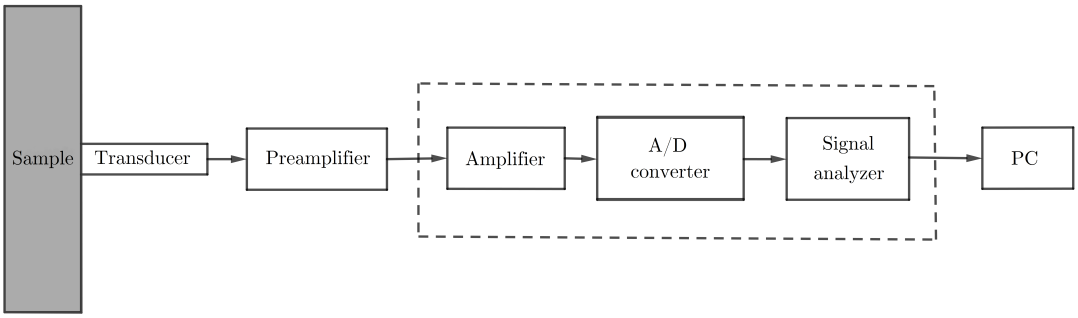

Figure 3.9: Scheme of AE signal acquisition and processing

tron diffraction spectra were collected. The AE was monitored by a computer-controlled system PAC PCI-2 (Physical Acoustic Corporation). In this setup, the Dakel MICRO 2006 (Dakel - ZD Rpety) transducer with a flat response between 50 and 650 kHz and the PAC 2/4/6 preamplifier with a gain of 40 dB were incorporated.

The recorded acoustic emission signal necessitated filtering during its post-processing in order to gain datasets with the most relevant information possible. The initial filtering was performed by scripts executed by the Python 3.9 software. The three basic filtering parameters were AE energy (which was required to be non-zero), counts (only the events with more than 20 counts were permitted) and amplitude (the threshold level was set above the permanent background noise, i.e., to 28 dB). Further filtering was performed manually based on the AE events timestamps. This was done to eliminate events originating during the respective, one hour long diffraction spectra collection periods. During these, the loading rig motor would sometimes "buzz" (despite the stationary state of the rig), emitting vibrations interfering with the AE measurement. AE event corresponding to these vibrations were therefore removed from the evaluated datasets.

3.3 Scanning electron microscopy

Scanning electron microscopy (SEM) is an imaging technique that provides resolution capabilities far beyond optical microscopes. This is because the angular resolution is proportional to the wavelength, with the values for the visible light (used in optical microscopes) ranging from ca. 380 to 760 nm [57]. In contrast, an electron accelerated to 15 keV (such electrons were used in this study) has a wavelength of approximately 0.01 nm (cf. Eq. 3.8). SEM, therefore, enables a detailed, highly magnified observation of the sample microstructure.

The scheme of a scanning electron microscope is depicted in Fig. 3.10, together with an illustration of the different types of signals, which can originate from the interactions of an accelerated electron within different areas of the sample. These electrons are produced in a field emission gun (FEG) as a result of emission due to intensive external electric field. The emitted electrons (further on called primary electrons) are accelerated by applying high voltage, and their beam is collimated

by an electro-magnetic lens (so-called condenser lens). After passing through an adjustable aperture, the beam is periodically deflected by a set of so-called scanning coils so that it continually scans the selected area of the sample surface. The deflected beam is then focused by the objective lens and interacts with the sample.

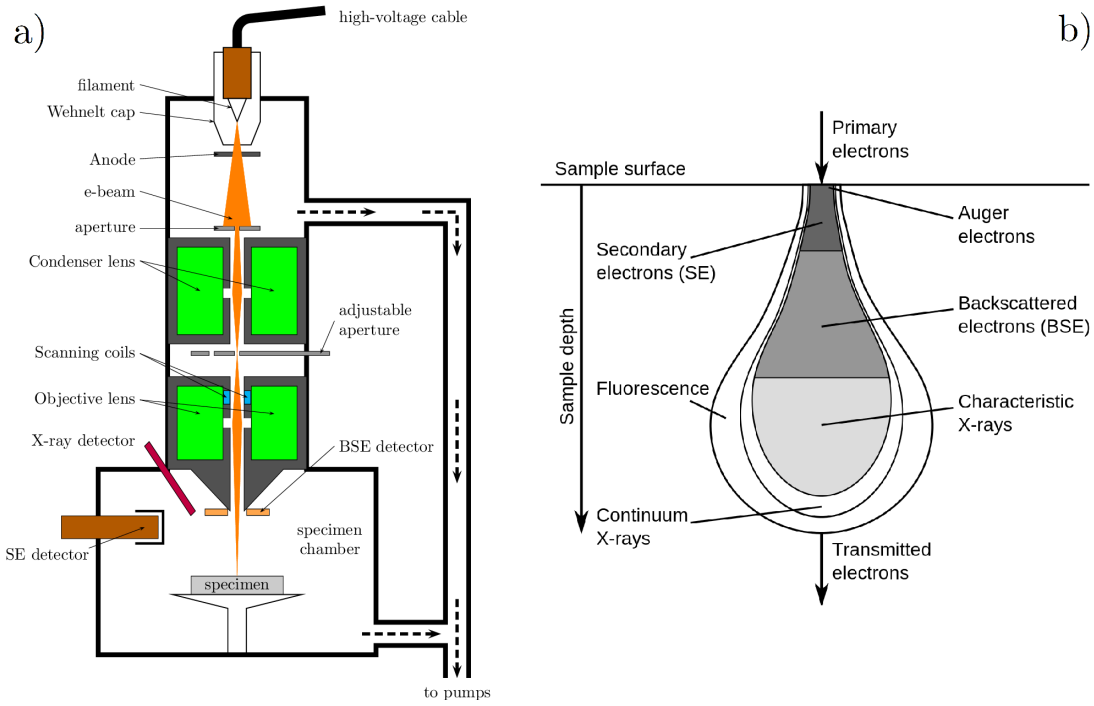

Figure 3.10: a) Scheme of the scanning electron microscope [58], b) schematic representation of the interaction volumes from which the specific signals in SEM originate [59]

The interaction of the primary electrons with the sample may lead to different types of radiation originating from various depths under the sample surface, cf. Fig. 3.10. The most important types of signal for this work are the secondary electrons (SE) and the backscattered electrons (BSE). Apart from these, the characteristic X-rays are often used to determine the local chemical composition of the sample (this technique is called energy-dispersive X-ray spectroscopy). The essential characteristics of SE and BSE are the following [57]:

- Secondary electrons are knocked out of the electron shells of sample atoms by primary electrons. Due to their low energy ($E < 50\,\mathrm{eV}$), the layer of the sample from which they originate is only $\sim 1\,\mathrm{nm}$ in metals. The SE signal is sensitive to surface orientation, which leads to a topography contrast used in surface observations.

- Backscattered electrons are (near) elastically scattered on the atomic nuclei within the sample under angles so acute that they escape the sample through its surface. Their interaction volume in metals is typically hundreds of nm due to their higher energy compared to SE. As a result of scattering amplitude variation with the nucleus atomic number Z, the BSE signal

forms the composition contrast. Another information in the BSE signal comes from the channelling contrast caused by the variation of penetration depths in the specimen based on its local crystallographic orientation.

3.4 Electron backscatter diffraction

Electron backscatter diffraction is a microstructural diffraction technique enabling to study the structure of the sample material. By scanning across the selected sample surface area and determining the local crystallographic orientations, characteristics such as grain boundaries, grain size distribution, texture, misorientation between individual grains, and many others can be examined both qualitatively and quantitatively [57].

The principle on which EBSD is based is the diffraction of previously inelastically scattered electrons. Upon entering the sample, the primary electrons interact with the scattering centres, which may result in their inelastic scattering. The angular distribution of the intensity of inelastically scattered electrons has a maximum in the original direction of the beam and decreases with the scattering angle. Some of the omnidirectionally scattered electrons are bound to meet the Bragg diffraction condition (Eq. 3.11) with the diffraction angle θ for any given set of planes (hkl), cf. Fig. 3.11. The electrons diffracted to higher angles with regard to the direction of the primary beam cause local excess of intensity compared to the undisturbed distribution and vice versa, the electrons diffracted to lower angles cause local deficiency of intensity. These disturbances in the intensity of electrons coming to the viewing screen cause the phenomenon called Kikuchi lines [60].

In three dimensions, the diffracted electrons form a surface of so-called Kossel cones, which are symmetrical with respect to the diffracting plane and have an apex angle $(\pi - 2\theta)$. The intersections of the Kossel cones and the viewing screen are theoretically hyperbolae, yet since the angles θ are typically minimal, the intersections appear line-like, hence the origin of the term Kikuchi "lines" [60].

To obtain the crystal orientation from the diffraction patterns, the positions of the Kikuchi lines are analysed by specialised software using the Hough transform [62]. Their mutual angles are calculated from the line positions and compared with a list of interplanar angles for the studied crystal structure. The best match of all the comparisons is then accepted as the orientation of this point of the sample surface [63]. The extent of agreement between the experimentally obtained and theoretically calculated line positions is characterised by a value called confidence index (CI). The systematic and automatised analysis of the diffraction patterns in all examined points on the sample surface then yields the resulting EBSD map.

To maximise the BSE yield, the sample is typically tilted by 70° towards the EBSD camera. The accelerating voltage needs to be optimised – higher voltage leads to higher BSE yield; however, it negatively influences the resolution [57]. In this study, the accelerating voltage of 15 keV was used.

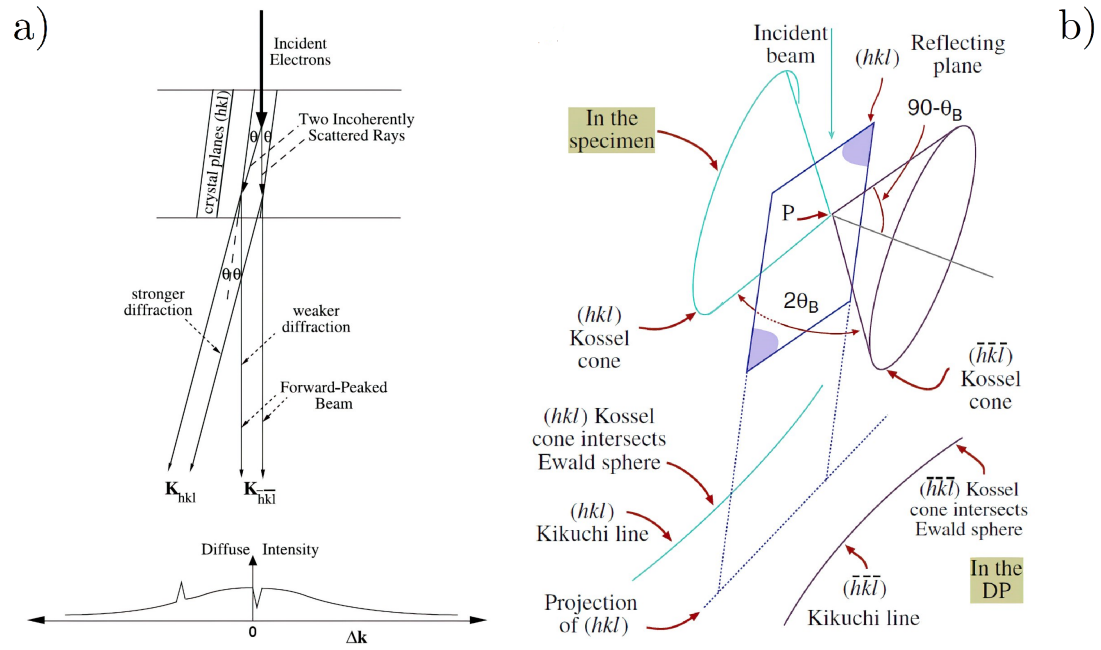

Figure 3.11: a) Scheme of the Bragg diffraction of inelastically scattered electrons [60]. θ marks the Bragg angle, and Δk denotes the magnitude of the diffraction vector $\vec{Q} = \vec{k_i} - \vec{k_f}$, b) schematic representation of the intersection of the Kossel cones and the diffraction pattern (DP), forming Kikuchi lines [61]. The Bragg angle is denoted θ_B here.

The SEM and EBSD measurements for this thesis were performed using the Zeiss Auriga Compact scanning electron microscope with a Schottky type field emission gun, equipped with an EDAX EBSD camera. The results presented in section 4.5 are based on the EBSD measurements performed during the in-situ deformation of the samples inside the vacuum chamber using the MTI SEMTester 1000 deformation table. Described photographs of the experimental setup for the in-situ EBSD measurements during compressive deformation are shown in Fig. 3.12. A secondary electron image of the sample before the deformation process is shown in Fig. 3.13.

During the EBSD data collection, which took ca. 20 minutes for each data point, some of the samples exhibited stress relaxation of ca. 5 MPa. In these cases, the presented stress values are those at the end of the data collection.

For collecting the EBSD data, the TSL-OIM Data Collection software was used. The analysis of the results was performed using the TSL-OIM Analysis 8.0 software. The raw data were partially cleaned, using the CI Standardization (setting the CI of all pixels within the grain to the maximum value of CI found in this grain) and Grain Dilation (assigning the pixels not belonging to any grain to the grain with which the pixel in question has the most neighbours and setting the CI of this pixel equal to the CI of the grain) processes, which were performed on all the datasets before further evaluation. The misorientation angle for high angle grain boundaries was set to be 15°. The grain tolerance angle was set to 5° (lower misorientation angles are caused by internal strain within the grain,

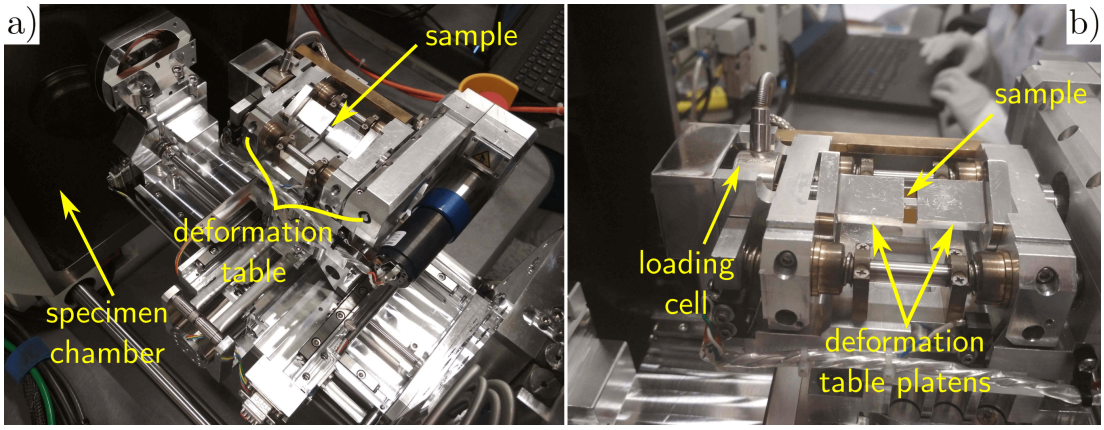

Figure 3.12: a) Setup of the in-situ EBSD deformation experiment, b) detail of the deformation table with a compressive sample

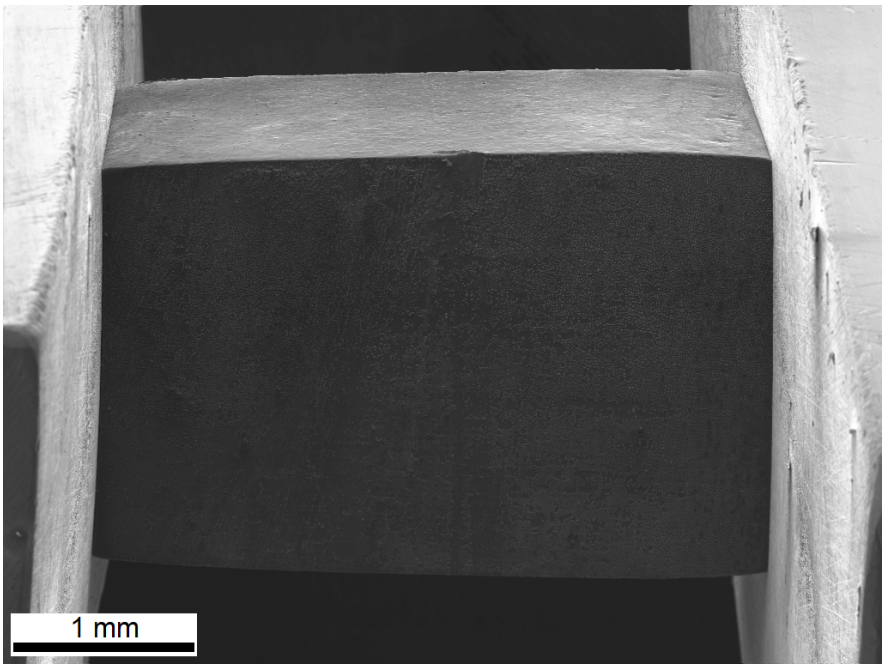

Figure 3.13: SE image of the sample captured during the compressive deformation

higher angles mark low angle grain boundaries) and the minimum grain size to 50 px. Areas smaller than 50 px and with CI lower than 0.1 were excluded from the further evaluation (due to the insufficient quality of the diffraction pattern).

All the EBSD maps shown in section 6.1 have the dimensions of $300 \times 300\,\mu m^2$ and were measured with the step size of $0.3\,\mu m$. The maps presented in section 4.1 represent an area of approximately $2.5 \times 2\,mm^2$ and were measured using the step size of $2\,\mu m$.

The results of the EBSD based microstructural analysis are presented in this thesis using the following representations:

- Pole figures (PF), displaying the distribution of selected crystallographic direction with respect to the sample coordinates.

- Inverse pole figures (IPF), displaying the distribution of crystallographic planes parallel with the observed sample surface for the specific sample direction.
- Inverse pole figure orientation maps, displaying the crystallographic orientation of grains using the IPF colour coding.
- Twin parent-daughter grain relation maps, displaying the parent and twin grains (of selected twinning mode) based on the reorientation analysis.

3.5 High-speed camera imaging

The high-speed camera imaging of the sample surface during deformation can provide valuable insight into the rapid processes during deformation. Potential macroscopic inhomogeneities in the deformation behaviour, as well as the collective behaviour of deformation twinning, may be observed by combining suitable magnification optics with a camera capable of capturing the sample surface with sufficient time resolution.

The surfaces of the samples undergoing compressive deformation were observed using the combination of a Photron FastCam SA-Z 2100K high-speed camera and a Questar QM-100 distance optical microscope. For the deformation of the samples, the MTI SEMTester 1000 deformation table was employed. The sample surface micrographs were captured with the frequency of 50 Hz and subsequentially exported with the time difference between the frames corresponding to the frequency of 5 Hz (due to data storage limitation).

3.6 Sample preparation

The samples for compressive deformation were machined using the ATM Brillant 220 cutting machine into cuboids. Their dimensions differed according to the specific deformation machine in which they would be used. The samples for the separate deformation tests and those for the interrupted deformation tests coupled with the acquisition of the neutron diffraction spectra and recording of the acoustic emission signal were machined with the initial dimensions of $5 \times 5 \times 7.5\,\mathrm{mm}^3$. The samples deformed by the MTI SEMTester 1000 deformation table during the in-situ EBSD measurements and high-speed camera imaging had the initial dimensions of $2.5 \times 2.5 \times 4\,\mathrm{mm}^3$. The samples for tensile testing were machined using the ATM Brillant 220 cutting machine and CNC milling machine to have an active zone with the dimensions of $1.5 \times 1.5 \times 4.5\,\mathrm{mm}^3$. The samples for the EBSD measurements of the initial microstructure and texture were cut to have a surface area of ca. $10 \times 10\,\mathrm{mm}^2$

The surfaces of the samples used for the acquisition of the neutron diffraction spectra were ground using watered abrasive SiC paper graded 1200. The surfaces of the samples for EBSD experiments and high-speed camera imaging were ground using a sequence of watered abrasive SiC papers graded 1200, 2400 and 4000 and then mechanically polished using a sequence of diamond suspensions

with the grain sizes of 3, 1 and 0.25 µm. The surfaces of the samples prepared for the initial microstructure EBSD observations were subsequently electropolished using the Struers LectroPol 5 machine with the AC2 solution. As the final step of the surface treatment prior to the in-situ EBSD measurements, the sample surfaces were ion polished using the Leica EM RES 102 machine. The mechanically polished samples for high-speed camera imaging were etched for ca. 3 seconds by a solution of ethanol, distilled water, acetic acid and picric acid (with the ratio of 50 ml : 9 ml : 4 ml : 6 g) to enhance the grain boundary contrast.

4. Results

4.1 Experimental material characterisation

The material used in this study was a commercial magnesium alloy AZ31 (96 wt. % Mg, 3 wt. % Al, 0.8 wt. % Zn, 0.2 wt. % Mn). It was received in the form of a 15 mm thick rolled sheet.

To illustrate the initial microstructure in the longitudinal (i.e., the RD × TD plane) and transversal (i.e., the ND × TD) planes, their IPF orientation maps are shown in Figs 4.1 and 4.2, respectively. Although most of the grains in the transversal plane are of similar diameters, several significantly larger grains are present, presumably as a remnant of the original microstructure not entirely refined by the rolling process. This, however, does not have a significant influence on the overall resulting grain size distribution, yielding similar results as the one evaluated in the longitudinal plane. Similarly coarse grains were not observed during any other studies using this experimental material.

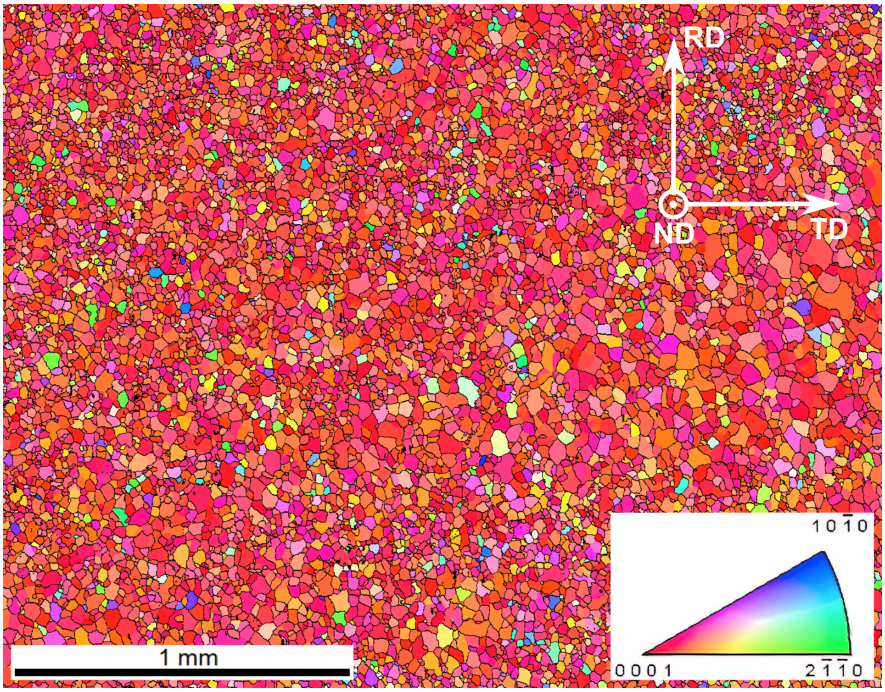

Figure 4.1: IPF orientation map of the original microstructure in the longitudinal plane of the AZ31 sheet

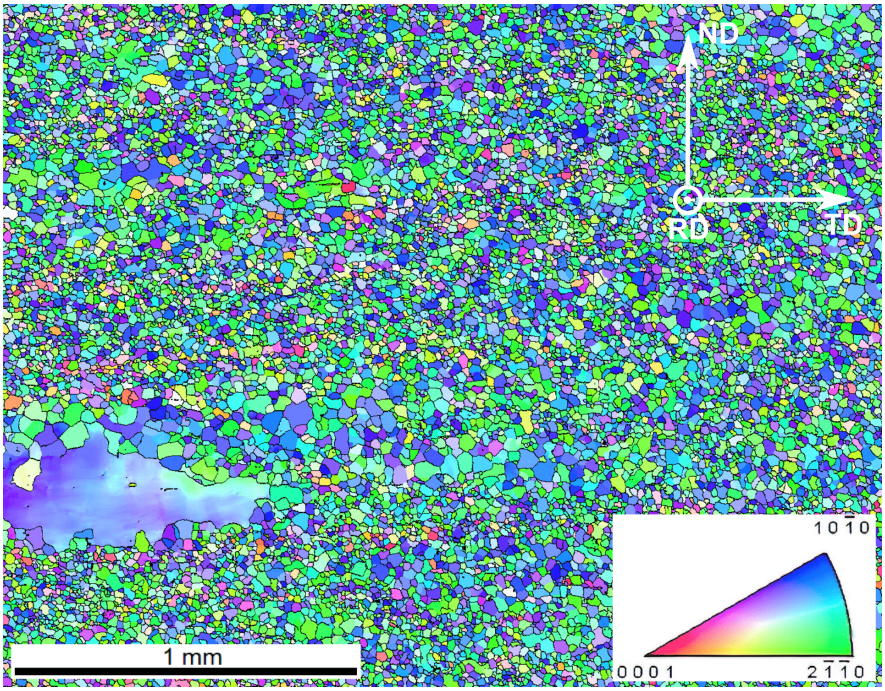

Figure 4.2: IPF orientation map of the original microstructure in the transversal plane of the AZ31 sheet

The average grain size diameter d was evaluated based on the EBSD measurements of the longitudinal sheet plane as $d = (31 \pm 13)\,\mu\text{m}$ (distribution mean $\pm$ distribution standard deviation). The grain size diameter distribution in this plane is shown in Fig. 4.3.

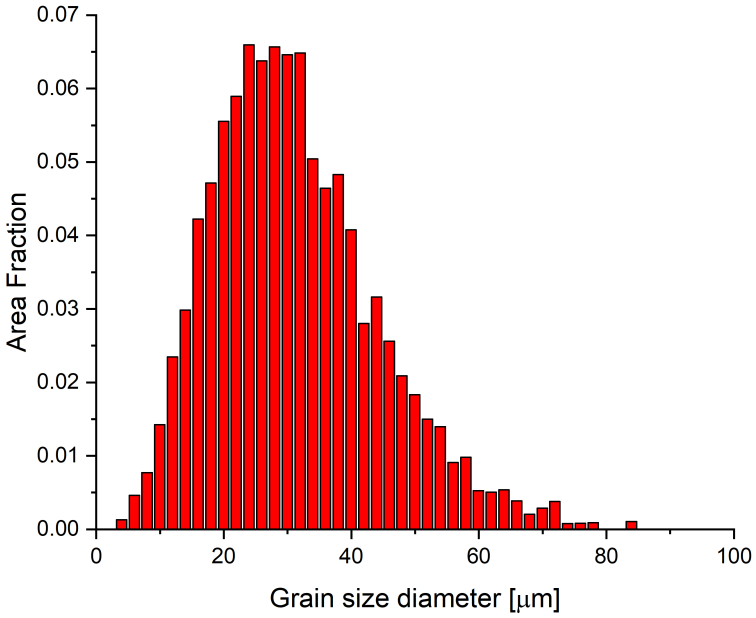

Figure 4.3: Grain size diameter distribution of the studied AZ31 alloy

The EBSD analysis of the sheet revealed the typical texture for rolled magnesium sheets (not containing rare-earth metals [31]), i.e., basal planes preferentially

oriented parallel to the sheet plane; cf. the pole figures in Fig. 4.4. The analysis was conducted on a dataset consisting of more than 9500 grains.

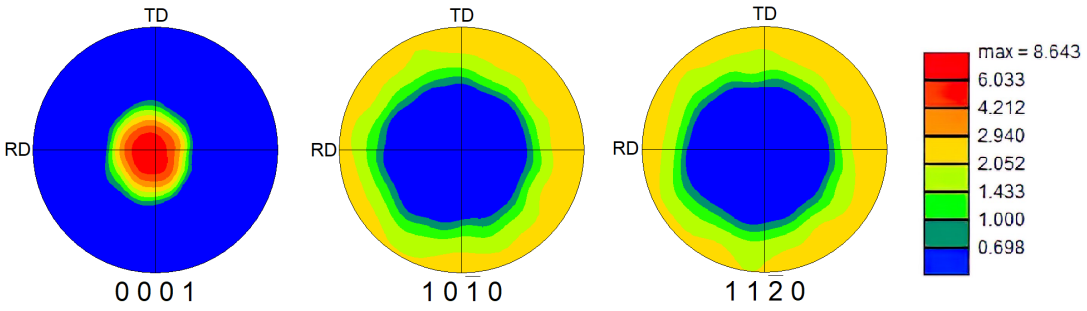

Figure 4.4: Pole figures of the AZ31 sheet texture

Based on the detected texture, three distinct orientations of samples with respect to the sheet coordinate system (cf. Fig. 1.9) were selected in order to provide a range of orientations regarding the identified basal texture:

- samples oriented in the sheet normal direction, further on denoted as ND
- samples oriented in the sheet rolling direction, further on denoted as RD
- samples oriented in the direction of 45° between RD and ND, further on denoted as 45

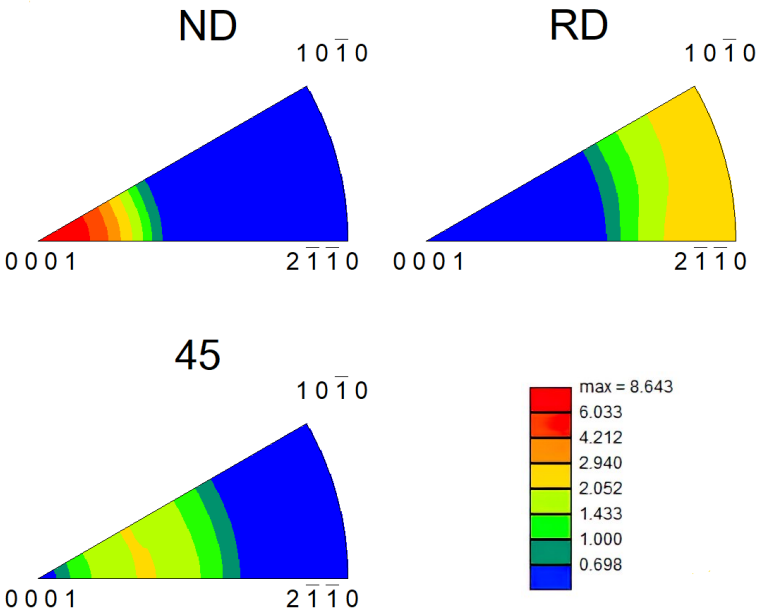

Figure 4.5: Inverse pole figures in the selected sample orientations

4.2 Deformation tests

The true stress - true strain curves measured for the samples of all the selected orientations during both compressive and tensile deformation are shown in Fig. 4.6. Only the plastic regions of these deformation curves are shown. For each combination of loading mode and sample orientation, only one curve is depicted, although four separate tests were carried out in order to confirm the repeatability of the experiments.

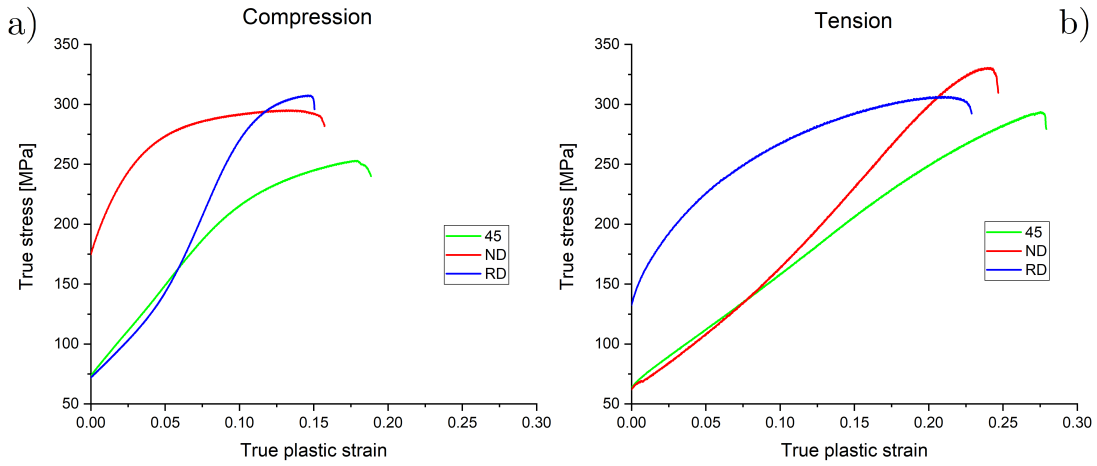

Figure 4.6: True stress - true strain curves of a) compressive and b) tensile deformation

The values of yield stresses $\sigma_{0.2}$ and true fracture stresses $\sigma_{t_{max}}$ calculated from the measured data for both loading modes and samples of all orientations are listed in table Tab. 4.1.

Table 4.1: Measured yield ($\sigma_{0.2}$) and true fracture $\sigma_{t_{max}}$ stresses for samples of all selected orientations deformed in compression and tension

	Compression		Tension	
Orientation	$\sigma_{0.2}$ [MPa]	$\sigma_{t_{max}}$ [MPa]	$\sigma_{0.2}$ [MPa]	$\sigma_{t_{max}}$ [MPa]
45	72 ± 7	251 ± 9	61 ± 6	291 ± 10
ND	175 ± 7	295 ± 4	61 ± 6	335 ± 14
RD	70 ± 6	315 ± 8	141 ± 8	315 ± 8

There are significant differences in the measured values of yield stresses. One can observe a distinct differentiation, where for a given loading mode, certain orientations of samples yield at values of stress more than twice those of other, easier yielding orientations. In compression, the only outlier is the ND sample, whereas, in tension, the RD sample exhibits high yield stress. The behaviour of these samples follows the suitability for activation of the $\{10\bar{1}2\} < 10\bar{1}1 >$ extension twinning (cf. Fig. 1.7 and 4.5) as the mechanism mediating the onset of plastic deformation. The yield stresses measured for the 45 sample are among

the low ones in both modes of deformation, indicating twinning and basal slip activity in these samples, deformed both in compression and tension.

To gain further insight into the specific deformation mechanisms causing the observed behaviour, more direct in-situ methods were employed. Their respective results were further compared and discussed with the aim to comprehensively understand the mechanisms mediating deformation of the samples. The measured values of the true stress - true strain dependence were used to determine the levels of stress, up to which the samples (with given orientation and loading direction) would be deformed prior to the in-situ observations (namely, the neutron diffraction spectra collection and the in-situ EBSD measurements).

4.3 Neutron diffraction

The in-situ neutron diffraction experiments were executed during the compressive loading of the samples. For each sample orientation, points in various stages of deformation, in which the diffraction spectra would be collected, were selected based on the previously performed deformation tests. The aim was to capture the neutron diffraction spectra in several different loads during the elastic deformation and then in various points during plastic deformation, with multiple data points in the vicinity of yield points and then spread further apart during the later stages of deformation. The position of the data points in the elastic region would be determined by the values of true stress (i.e., stress-controlled) and in the plastic region of deformation by the values of true strain (i.e., strain-controlled). The true stress and true plastic strain values corresponding to points where the neutron diffraction data were acquired are listed in Tab. 4.3. The deformation curves (calibrated according to the description in subsection 3.2.3) are shown in Fig. 4.7.

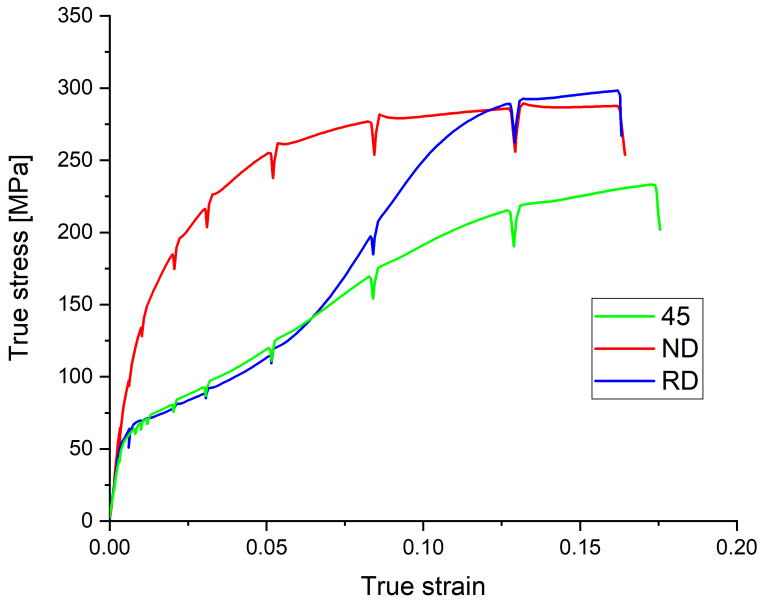

Figure 4.7: The true stress - true strain curves of the samples deformed in compression during the neutron diffraction experiments

The detector setup (cf. subsection 3.2.3) enabled the identification of five different diffraction plane reflections listed in Tab. 4.2. An example of the neutron diffraction spectra with labelled peaks is shown on the left-hand side of Fig. 3.3.

Table 4.2: List of reflections detectable by the specific setup of the neutron diffraction experiment. Besides the Miller indices of the reflecting planes, the corresponding wavelengths λ and the diffraction angles 2θ are also listed.

Reflection	λ [nm]	2θ [°]
$(10\bar{1}3)$	1.2	48.21
$(10\bar{1}0)$	2.4	51.32
$(11\bar{2}2)$	1.2	52.25
$(20\bar{2}1)$	1.2	53.25
(0002)	2.4	55.00

The difference in apparent wavelengths is caused by the fact that the $(10\bar{2}0)$ and (0002) reflections came from the first harmonic, while the $(10\bar{1}3)$, $(11\bar{2}2)$ and $(20\bar{2}1)$ reflections originated from the second harmonic, which appeared during the monochromatisation of the neutron waves. It should be noted that not all of these reflections were always detectable above the background radiation along the course of deformation.

Table 4.3: The values of true stress σ_t and corresponding true plastic strain values ε_{t_p} of the points selected for neutron diffraction spectra acquisition for each sample

	45		ND		RD	
Point No.	σ_t [MPa]	ε_{t_p} [%]	σ_t [MPa]	ε_{t_p} [%]	σ_t [MPa]	ε_{t_p} [%]
1	2	0	3	0	3	0
2	23	0	23	0	23	0
3	43	0	43	0	43	0
4	64	0.2	50	0	64	0.1
5	67	0.6	64	0	67	0.4
6	76	1.4	95	0	69	0.6
7	86	2.4	129	0	76	1.4
8	112	4.5	177	0.8	86	2.5
9	155	7.8	205	1.8	110	4.6
10	194	12.3	241	3.9	189	7.8
11	205	16.9	258	8.4	271	12.3
12			263	11.6	276	15.7
13			267	15		

The variation of diffraction peak intensities associated with texture changes resulting from the $\{10\bar{1}2\}$ extension twinning can be used to monitor the activity of this deformation mechanism. During compressive deformation and using the axial detector geometry (the case of this study), the change in peak intensity associated with the $\{10\bar{1}2\}$ twinning is related to the $\{10\bar{1}0\} - \{0002\}$ and $\{11\bar{2}0\} - \{10\bar{1}3\}$ parent-daughter grain relation. In particular, the intensities of the $(10\bar{1}0)$ and $(11\bar{2}0)$ peaks decrease, and at the same time, the (0002) and $(10\bar{1}3)$ peak intensities increase [42]. However, the $(11\bar{2}0)$ reflection falls just beyond the angular range of the employed detector setup (with its corresponding diffraction angle $2\theta = 44.05°$). As a result, the extension twinning activity was studied based on the increment of the (0002) and $(10\bar{1}3)$ peak intensities and only the $(10\bar{1}0)$ peak intensity decrement.

The values of the above-described peak intensities are shown for each sample orientation individually in Fig 4.8. The specific presented values are the dependences of normalised integrated intensities (i.e., the ratio of areas under the diffraction peaks of the given, and the first data point where the peak was clearly detectable above the background radiation, thus representing the initial state) on the true stress. For each data point, the error bars are also displayed, although they can not be distinguished in many cases since they are smaller than the mark of the data point. For easier orientation, the baselines marking the normalised integrated intensity value of 1 are also provided. In the ND oriented sample, the peak corresponding to the $(10\bar{1}0)$ planes was undetected along the whole deformation process, hence the absence of corresponding data points.

One can observe that in the samples exhibiting a significant change of the peak intensities (i.e., 45 and RD), this behaviour onsets around the yield point. The manner of the normalised integrated intensities change meets the expectation with the (0002) and $(10\bar{1}3)$ intensities increasing and the $(10\bar{1}0)$ intensity decreasing as a result of texture changes caused by the $\{10\bar{1}2\}$ extension twinning.

In both the samples exhibiting notable changes, the peak intensity increase is more pronounced on the (0002) plane reflections than the $(10\bar{1}3)$ ones. The magnitude of the normalised integrated intensity change, which is proportional to the relative twinned volume fraction [34], is significantly higher for the RD sample compared to the 45 oriented one with the difference as high as an order of magnitude at similar stress levels in the later stages of deformation. The increase in the integrated intensities in these samples saturates at the true stress values of 189 and 155 MPa, respectively, corresponding to ca. 7.8% of plastic deformation in both the RD and 45 oriented samples.

The ND sample, oriented unfavourably for the extension twinning under compressive loading, exhibits significantly less pronounced changes in the peak intensities. After reaching its yield point (which is considerably higher than those of the 45 and RD samples, cf. Tab. 4.1), the intensity of the peak corresponding to the diffraction on the $(10\bar{1}3)$ plane slightly decreases. This being the only notable change in peak intensities further proves that the $\{10\bar{1}2\} < 10\bar{1}1 >$ extension twinning does not play any major role in the deformation of the ND oriented samples.

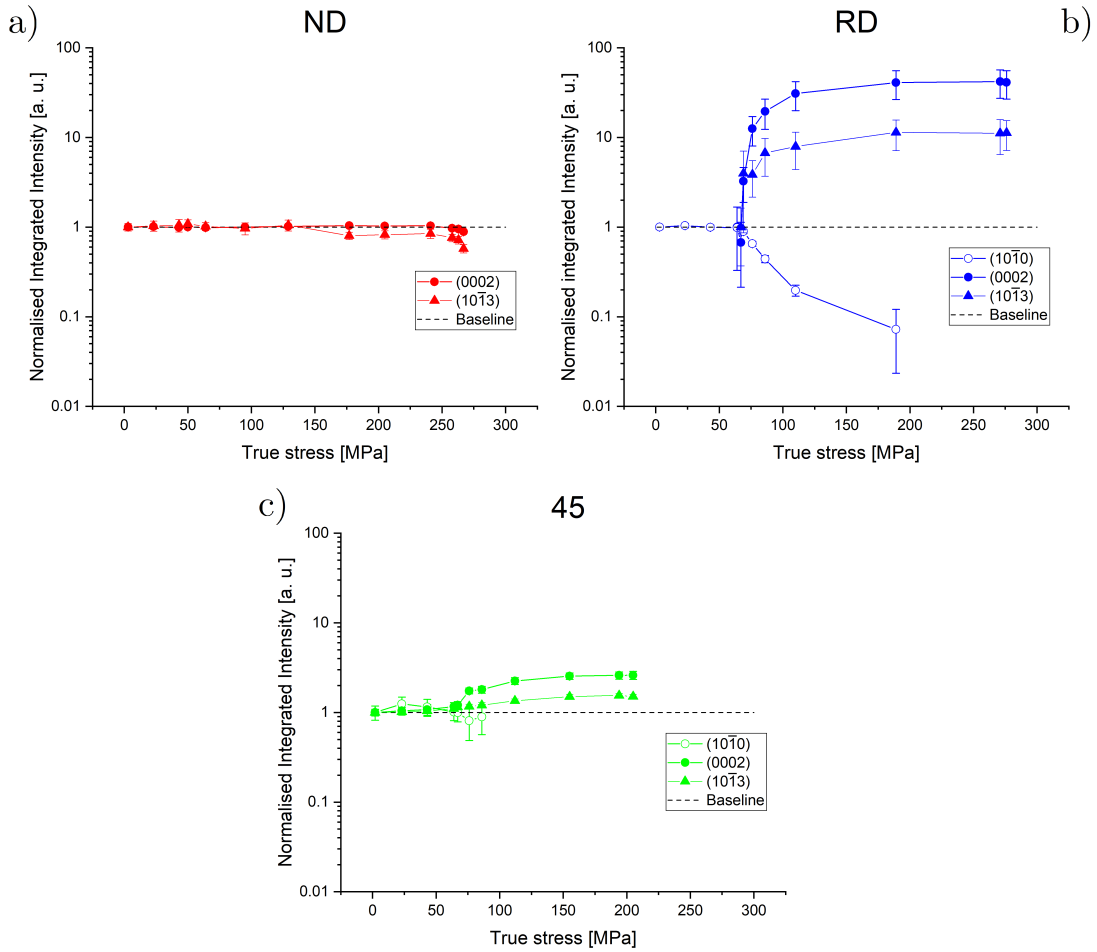

Figure 4.8: Evolution of the normalised integrated intensities of selected diffraction peaks during compressive deformation of the a) ND, b) RD and c) 45 oriented samples

The evolutions of lattice strains with the increase in the true stress are shown in Fig. 4.9 for all three sample orientations. For each data point, the error bars are displayed (although in some cases, they are smaller than the marker of the point). For comparison with the linear dependence of the lattice strains on the true stress, predicted by the Hooke's law, dashed lines representing this linear behaviour are included.

For evaluating lattice strains, the peak positions of the stress-free state of the material have to be measured. For this purpose, the peak positions measured in the initial data points, corresponding to the preload of ca. $2-3$ MPa, were used. Only the evolutions of the lattice strains corresponding to reflections with detectable peaks at these low-stress values (and thus providing a reasonable approximation of stress-free state) were studied.

For the RD sample, only the lattice strains on the $(10\bar{1}0)$, $(11\bar{2}2)$ and $(20\bar{2}1)$ planes were available for evaluation. The following behaviour can be observed – the $(10\bar{1}0)$ and $(20\bar{2}1)$ planes lattice strain approximately follows the theoretical elastic response line across the range of their peaks detectability. However, the

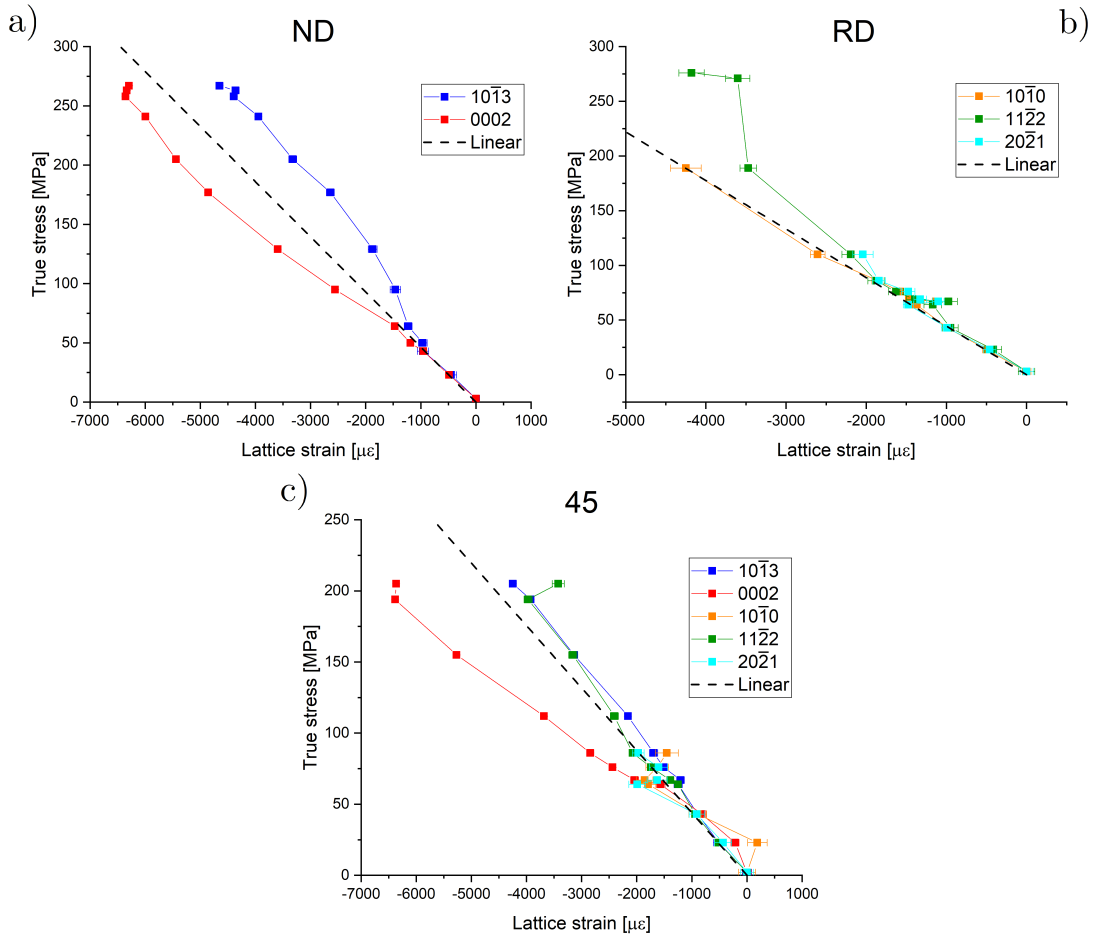

Figure 4.9: Evolution of the lattice strains with true stress and their comparison with linear behaviour predicted by Hooke's law for the a) ND, b) RD and c) 45 oriented samples

lattice strain on the (11$\bar{2}$2) plane deviates above the linear dependence above ca. 100 MPa.

In the diffraction spectra of the ND sample, only the reflections of the (10$\bar{1}$3) and (0002) planes were detectable above the background. Their lattice strain evolution follows the theoretical elastic response up to the data point corresponding to the true stress of 64 MPa. After that, the (10$\bar{1}$3) lattice strain deviates above the linear dependence, indicating its "soft" orientation, while the (0002) lattice strain falls below the line of elastic response. Since there is only limited evidence of the $\{10\bar{1}2\} < 10\bar{1}1 >$ extension twinning activity during the deformation of this sample (cf. Fig. 4.8 c)), the explanation of this phenomena is likely more complex, cf. section 5.2.

The 45 oriented sample is the only one for which the evolution of lattice strains of all the planes with reflections within the detector range could be followed. The most significant deviation from the theoretical elastic response can be observed in the (0002) plane, which falls below the linear dependence once the macroscopic yield point is reached. This is an expected behaviour as a result of the $\{10\bar{1}0\}$ –

{0002} grain reorientation due to extension twinning – the "soft" oriented $(10\bar{1}0)$ grains start to behave plastically, and their lattice strain curve deviates above the straight line (unfortunately, in this case, its peak ceases to be detectable rather briefly after the point of deviation). The conjugate lattice strain curve of the (0002) plane, being the "hard" oriented grain, needing to accommodate a larger portion of the elastic loading, falls below the straight line [42]. One would expect the lattice strain evolution of the $(10\bar{1}3)$ to exhibit similar behaviour as the (0002) (following the same line of reasoning); however, that is not the case here. The deviation of the $(11\bar{2}2)$ plane above the theoretical elastic response line is consistent with its behaviour in the RD oriented sample.

The neutron diffraction experiments were coupled with a concurrent monitoring of the acoustic emission, providing insight into the dynamics of the processes, the results of which were observed in the sample volume with the neutron diffraction techniques.

4.4 Acoustic emission

The evolution of the AE events amplitudes with the true strain is shown for all sample orientations simultaneously in Fig. 4.10. The logarithmic scale is used in order to improve the differentiability of individual depicted events. For an illustration of the relative location of AE events and the respective macroscopic yield points, vertical lines intersecting the true strain axis at the corresponding values $\varepsilon_{0.2}$ for each sample are also displayed.

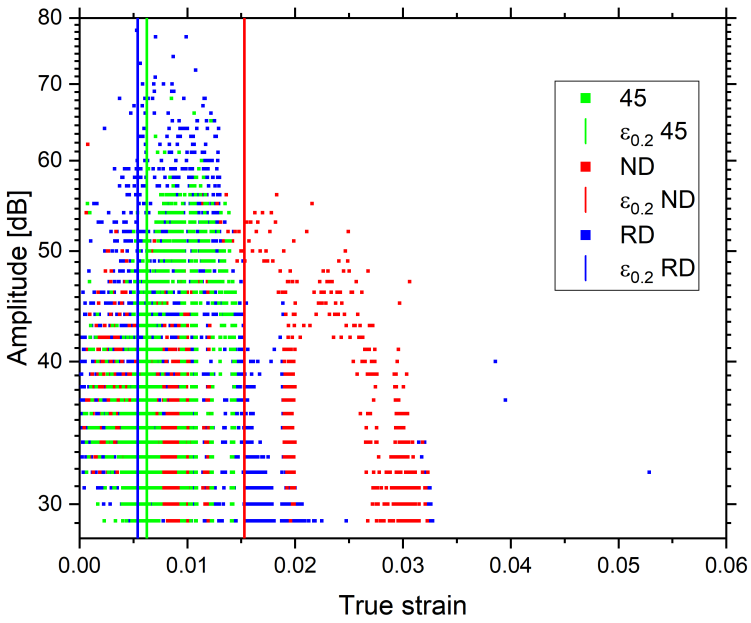

Figure 4.10: Dependence of the AE events amplitudes on true strain for all sample orientations. Vertical lines illustrate the true strain values of macroscopic yield points of each sample.

The minimal value of the depicted amplitudes is 29 dB because of the threshold eliminating the background noise. The maximal values (for all three sample

orientations) are attained in the vicinity of the macroscopic yield point and in the early stages of plastic deformation. The onset peaks are related to the rapid dislocation multiplication and their avalanche-like movement at the beginning of plastic deformation and the twin nucleation (if present). The rather abrupt consequent decay of the AE activity is caused by the reduction of the flight path of dislocation lines due to the increase in the density of immobile dislocations and exhaustion of the (AE detectable) twinning activity [52, 34].

The different AE signal amplitudes measured for different sample orientations indicate a difference in the activated deformation mechanisms. The sample oriented favourably for the $\{10\bar{1}2\} < 10\bar{1}1 >$ extension twinning (i.e., RD) exhibits higher AE signal amplitudes than the unfavourably oriented sample (ND) with the 45 sample behaviour somewhere between these two extremes. This behaviour is in accordance with the results of other works, such as [52], which concluded that in Mg single crystals, the activation of slip mechanism led to lower amplitudes of AE signal compared to the cases where extension twinning was active.

To illustrate the correlation of the AE response and the deformation curves, the AE count rate dependencies on the true strain are plotted together with the flow curves in Fig. 4.11 separately for all three different sample orientations. The presented values of count rates are, in fact, the summed values of count rates within equidistant strain windows with a fixed with of 0.05% of true strain. For easier orientation, the yield points are marked on each flow curve.

The presented figures clearly demonstrate the culmination of the AE response in the vicinity of the macroscopic yield point for all the sample orientations, followed by a rapid decline. The evolution of the AE count rate for the RD oriented sample exhibits peak values comparable with the 45 sample; however, the AE response in the RD sample declines more gradually, eventually falling below the detectable level around 5% of plastic deformation. In contrast, in the 45 sample, it ceased to be detectable significantly earlier, around 2.5% of plastic deformation. One can observe a distinct spike in the AE count rate related to the reloading of the sample after the neutron diffraction spectra were collected at the true stress value of 110 MPa. All of the samples exhibited a detectable AE signal long before their macroscopic yield points, this effect being more pronounced in the RD and 45 samples. The most distinct behaviour was that of the ND sample. The peak values of the AE count rate were lower compared to the other samples (by a factor of approximately 3), and the evolution of its values exhibited a more gradual increase during the elastic region of deformation. This was followed by a rapid decrease once the maximum values were attained near the macroscopic yield point.

To investigate the microstructure of the samples undergoing deformation and thus specify and expand the observations based on the acoustic emission signal analysis, the in-situ EBSD measurements were performed.

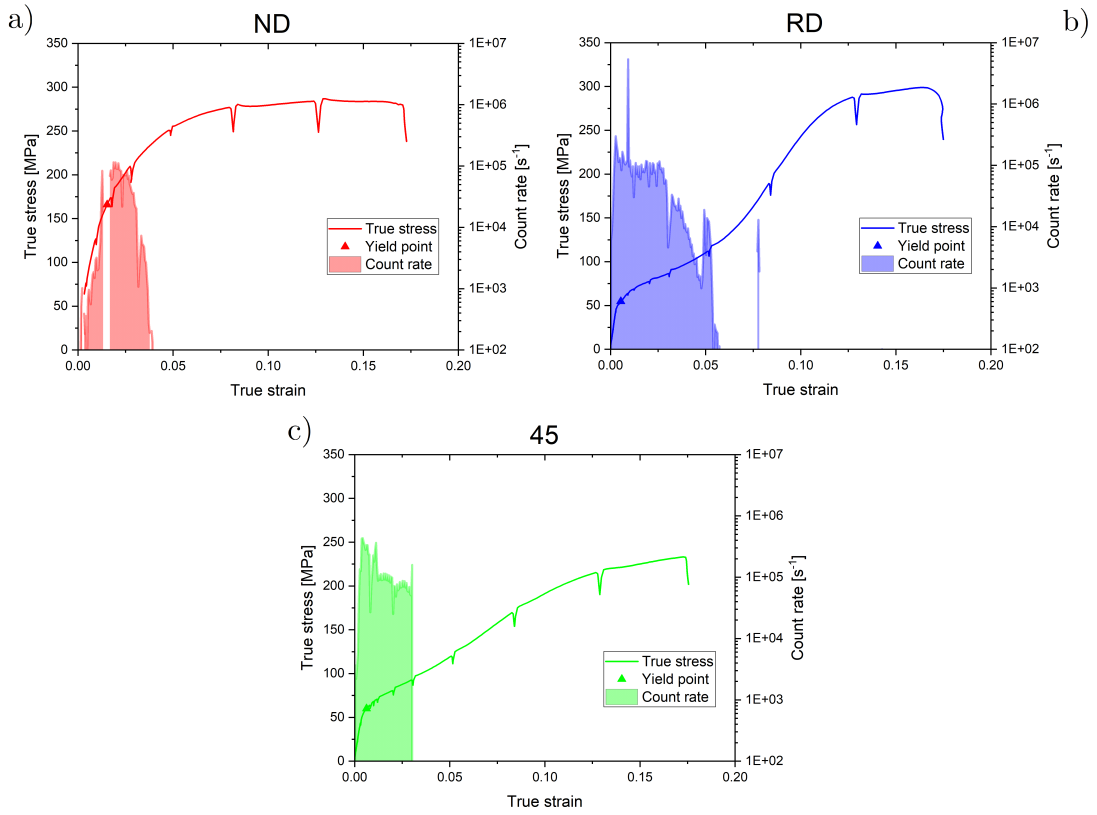

Figure 4.11: Comparison of the AE count rates and the respective flow curves for the a) ND, b) RD and c) 45 oriented samples

4.5 In-situ EBSD

The EBSD measurements were performed during the compressive deformation of the samples inside the specimen chamber of the scanning electron microscope. At the beginning of each experiment (i.e. after installing the sample to the deformation machine, its preloading to an initial stress level and adjusting the whole experimental setup within the microscope chamber), a reference EBSD map corresponding to the initial state of the sample was acquired.

Subsequentially, a progression of sample loading up to pre-selected stress values and performing EBSD measurements of the equivalent sample surface area at these stress levels was performed. The stress values of individual data points were selected based on the values from deformation tests presented in section 4.2. For each sample orientation, 3 to 5 data points were chosen so that the data could be compared with those from the neutron diffraction and high-speed camera imaging experiments. Furthermore, the emphasis was on gaining an insight into the microstructural evolution in the early stages of plastic deformation and possible evaluation of twinning activity in this stage. More data points were therefore measured for the RD and 45 samples compared to the ND one. The data points (including the ones corresponding to the initial sample states) are listed in Tab. 4.4.

Table 4.4: True stress (σ_t) and corresponding true plastic strain values ε_{t_p} of the data points selected for the in-situ EBSD measurements for each sample

	45		ND		RD	
Point No.	σ_t [MPa]	ε_{t_p} [%]	σ_t [MPa]	ε_{t_p} [%]	σ_t [MPa]	ε_{t_p} [%]
1	7	0	9	0	11	0
2	77	2.2	163	1.5	77	2.3
3	106	6.2	188	3	102	5.4
4	129	9.5	206	4.6	127	7.9
5	170	14.6			190	12.9
6					230	17.3

4.5.1 Microstructural evolution

To comprehensively illustrate the microstructural evolution during loading, IPF orientation maps of the samples with given orientation corresponding to increasing stress levels are presented in attached Figs. 6.1, 6.2 and 6.3.

The initial states of all the samples exhibit similar grain size distributions. They contain no deformation twins (which could potentially originate from the sample preparation), and, therefore, all of the deformation twinning observed in the samples originated during the actual loading process. The microstructural evolution of the sample oriented favourably for the $\{10\bar{1}2\} < 10\bar{1}1 >$ extension twinning, i.e. RD, is shown in Fig. 6.2. The RD sample exhibits a significant twinning activity in the first plastically deformed state, corresponding to 77 MPa (ca. 2.3% of plastic deformation and therefore rather briefly after the macroscopic yield point). This supports the claim that the transition to plastic deformation in these samples is mediated by twinning. All of the twins visible in Fig. 6.2b) are those of the $\{10\bar{1}2\} < 10\bar{1}1 >$ type (as was confirmed by the reorientation analysis, cf. subsection 4.5.2) and have nucleated in the grains oriented favourably to do so (cf. subsection 5.3).

The maps of the states after an increase in the stress level in this sample, namely 102 and 127 MPa (Figs. 6.2 c) and d)), corresponding to ca. 5.4 and 7.9 % of plastic deformation, respectively, exhibit an increase in the twinned volume fraction. This is mediated both by further nucleation of twins and also by the growth of the already nucleated ones. The reorientation analysis of these sample states revealed only negligible activity of the $\{10\bar{1}1\} < 10\bar{1}\bar{2} >$ contraction twinning or possible subsequent $\{10\bar{1}1\} - \{10\bar{1}2\}$ double twinning (often observed in magnesium alloys [64]). The heavily deformed RD sample states, loaded to 190 and namely 230 MPa, then contain areas of low confidence index (visualised by black colour), located preferentially along the original grain boundaries.

The orientation of the 45 sample also partially favours the $\{10\bar{1}2\} < 10\bar{1}1 >$ extension twinning, which means that a considerable twinning activity during the deformation can be expected. During the evolution of the microstructure

with increased load, illustrated in Fig. 6.3, the extension twinning was indeed observed, albeit less pronounced compared to the RD oriented sample. In the first examined state after the macroscopic yield point, i.e., after loading to 77 MPa, corresponding to ca. 2.2% of plastic deformation, the $\{10\bar{1}2\} < 10\bar{1}1 >$ twins have not nucleated uniformly. The observed twins tended to aggregate into bands oriented perpendicularly to the loading direction – an example of such a twinning band is visible in the bottom right corner of Fig. 6.3 b). During further loading, the preferred orientation of the twins remained perpendicular to the loading direction (cf. Figs 6.3 c), d)), although numerous exceptions are observable. There is a distinct difference in the manner of the twinned volume fraction increase during the deformation process. Until the state shown in Fig. 6.3 c), corresponding to ca. 6.2% of plastic deformation, the twinned volume fraction seems to increase preferentially by twin nucleation. In the later stages of deformation, virtually no further nucleation was detected – instead, the already nucleated twins tended to grow. Regarding other twinning modes, the reorientation analysis revealed almost no $\{10\bar{1}1\}$ contraction or $\{10\bar{1}1\} - \{10\bar{1}2\}$ double twins.

The microstructural evolution of the ND oriented sample within the studied interval is illustrated in Fig. 6.1. Considering the unfavourable orientation of the majority of grains for possible activation of extension twinning, this mechanism was not expected to significantly influence the plastic deformation of this sample. The macroscopic yielding of this sample is expected to be mediated mainly by the $\{11\bar{2}2\} < 11\bar{2}3 > 2^{\text{nd}}$ order pyramidal slip. These expectations were mostly met – extension twins were observed only in the few favourably oriented grains out of line with the measured basal texture (cf. Fig. 6.4 b)). The extension twins observable in 6.4 b) had nucleated before the macroscopic yield point was reached due to microyielding in the grains oriented favourably to do so. This is related to the significantly lower value of CRSS for $\{10\bar{1}2\} < 10\bar{1}1 >$ extension twinning compared to that of the $\{11\bar{2}2\} < 11\bar{2}3 > 2^{\text{nd}}$ order pyramidal slip, which governs the macroscopic yielding of the sample. Despite the favourable sample orientation for the activation of the $\{10\bar{1}1\} < 10\bar{1}\bar{2} >$ contraction twinning, very few twins of this type (as per reorientation analysis) were observed. This can be explained by the high CRSS value of contraction twinning.

4.5.2 Twinned volume fraction

The twinned volume fraction (TVF) was evaluated using the twin-parent grain relation calculation performed by the TSL-OIM Analysis 8.0 software. In this mode, the program automatically detects the defined twin boundaries and assigns the twin parent or daughter role to sample surface regions enclosed (at least partially) by this specific boundary, cf. Fig. 6.5. The resulting twinned volume fraction is then obtained from the ratio of the area corresponding to the twin daughters to the whole examined sample surface area.

The presented results correspond to all of the studied sample states of the ND and 45 samples; however, in the case of the RD sample, only the first two plastically deformed states were evaluated. Beyond these, the microstructure was too heavily deformed, and the twinned volume fraction analysis has failed. Only

the twinned volume fraction results corresponding to the $\{10\bar{1}2\} < 10\bar{1}1 >$ extension twinning are presented because the $\{10\bar{1}1\} < 10\bar{1}\bar{2} >$ contraction twins were so scarce that the results could be significantly skewed by the limited statistical significance of the examined dataset.

The results are shown in Fig. 4.12 as a dependence of the twinned volume fraction on the true plastic strain. The RD oriented sample exhibits a rapid increase in the twinned volume fraction in the early stages of plastic deformation, reaching 35% at the true plastic strain of 5.4%. In comparison, the TVF increase in the 45 sample is much more gradual, exhibiting values lower by the factor of ca. 6 at a similar strain level. This, however, enables observation of the TVF increase even in the later stages of deformation, eventually reaching 12% at the true plastic strain of 14.6%. The TVF of the extension twinning-wise unfavourably oriented ND sample saturates on values roughly an order of magnitude lower than those of the RD oriented one. In the ND sample, the $\{10\bar{1}2\}$ twins have nucleated only in the few favourably oriented grains (cf. Fig.6.4 b)) and subsequently grew until saturation by the 3% plastic deformation mark. The 45 oriented sample, in contrast, exhibits a TVF value increase even in the later stages of deformation. This leads to the eventual twinned volume fraction in the 45 sample being ca. four times higher than the ND one despite their similar values at the onset of plastic deformation.

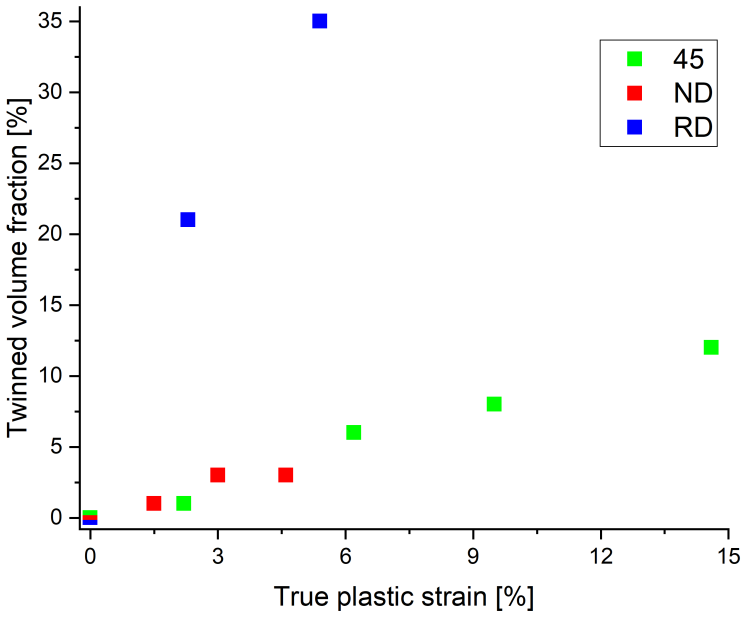

Figure 4.12: Results of the twinned volume fraction analysis. Overlaying data points are marked by a combination of their respective colours.

While the in-situ EBSD experiments provide an important qualitative and quantitative insight into the deformation behaviour of the studied samples, the nature of this technique does not enable observation of rapid processes – it rather represents a method of analysis of their results. To observe these rapid processes, high-speed camera imaging of the deformed sample surface was employed.

4.6 High-speed camera imaging

The behaviour observed via high-speed camera imaging during the compressive deformation of the samples is illustrated by figures attached in subsection 6.4.

The initial state of the RD sample, corresponding to the true compressive stress of ca. 16 MPa, is shown in Fig. 6.6 a). During the subsequent elastic deformation, no sample surface changes were observed (besides the permanent defocusing necessitating manual refocusing, which was common to all of the conducted high-speed camera experiments). The first notable microstructural change was a number of twins nucleating in a localised area at 72 MPa of true compressive stress. These newly nucleated twins (or rather the points at the twin-lens vertices – this form of presentation was selected in order to optimise the detectability of the marked twins whilst avoiding cluttering the figures trying to highlight the whole twin lenses) are marked with blue dots in Fig.6.6 b). Shortly afterwards, further bands of twin nucleation were observed, cf. Figs 6.6 c) and d) separated from the initial appearance of twin nucleation by 0.8 and 1.2 seconds, respectively (corresponding to less than 1 MPa of stress difference).

The stress level at which the first twin nucleation was observed is in a reasonable agreement with the value of compressive yield stress of the RD samples presented in Tab. 4.1. This further supports the hypothesis that the yielding of the samples oriented favourably to do so (such as the RD sample in compression) is mediated predominantly by the activation of $\{10\bar{1}2\} < 10\bar{1}1 >$ extension twinning. The fact that the twin propagation process itself was not detected (which is, in fact, true for all of the experiments presented in this thesis) is not surprising, given the very low effective used frame rate, the grain size of the studied material and the fact that the twin propagation velocity was recently (experimentally based) estimated to be tens of ms^{-1} [30].

The trend of twin nucleation occurring within separated bands perpendicular to the loading direction and the propagation of these nucleated twin bands along the loading direction with the increase in load (specifically from the bottom to the top of the monitored surface area in this case) continued to be observed during further loading beyond the macroscopic yield point, cf. Figs 6.7 a) and b), corresponding to 75 and 81 MPa, respectively. Beyond 103 MPa, corresponding to ca. 2.4% of plastic deformation and presented in Fig. 6.7 c), further twin nucleation was not observed. The prevailing trend in this region of plastic deformation was twin growth and also the formation of a relief leading to (and thus being indicated by) partial defocusation. This phenomenon was again observed in bands perpendicular to the loading direction, as is illustrated by Fig. 6.7 d), where only a horizontal band of the sample surface (forming a "valley" in the relief) remains in focus.

The state of the 45 sample subjected to the true compressive stress of ca. 43 MPa and thus being in the elastic region of the deformation is shown in the attached Fig. 6.8 a). The first observation of twin nucleation in this sample was made around the true compressive stress value of 65 MPa and is therefore in agreement with the experimentally obtained values of true compressive yield

stress for this sample orientation, cf. Tab. 4.1. Along with the twin nucleation, a movement of two distinct material bands, in which the nucleation occurred, oriented perpendicularly to the loading direction, can be observed. The bands shifted parallel to the loading direction – this phenomenon is illustrated by the dashed lines outlining the bands and arrows indicating their movement in Fig. 6.8 b).

Throughout the increase of stress from 65 to 73 MPa, multiple other twins have nucleated. These twins tended to be oriented perpendicularly to the loading direction but compared to the RD sample (and to a certain extent also to the nucleation which took place in the 45 sample around the yield point), the collective band-like character of the nucleation was significantly less pronounced, and the overall number of nucleated twins was lower. The above-described twins are indicated in Fig. 6.8 c).

It should be noted that all of the observed twinning activity took place in the upper half of the monitored sample surface area, whereas the lower half remained visibly less deformed. The evolution with the increase in load pronounces this behaviour even more – cf. Fig. 6.8 c) with Figs. 6.8 d) and e), corresponding to ca. 97 and 121 MPa, respectively. In Fig. 6.8 f), corresponding to the sample state loaded to ca. 147 MPa, one can observe that the bottom part of the previously less deformed region exhibits a defocusation also linked to the formation of relief, leaving an in-focus horizontal band of significantly less deformed and reliefed material in the bottom half of the figure.

The common factor of the deformation behaviour of the RD and 45 sample (besides the observed twinning activity) is the band character of deformation propagation with the bands oriented perpendicularly to the loading direction, regardless of the differences in the textures of these sample orientations.

The ND sample loaded to 74 MPa (which is well within the elastic region of deformation for this sample orientation) is shown in the attached Fig. 6.9 a). No twinning activity was observed around the expected value of compressive yield stress. However, at the true compressive stress of ca. 180 MPa (and therefore rather briefly after the macroscopic yield point), boundaries of forming deformation bands become visible – in Fig. 6.9 b), these boundaries are outlined with red dashed lines. Three distinct boundaries tilted by ca. 10° from the horizontal direction (and therefore oriented near perpendicularly to the loading direction) are visible.

With the increase in true compressive stress to ca. 205 MPa, these deformation bands become more visible due to the higher contrast of the boundaries resulting from the formation of relief. The curvature of the monitored sample surface area increases, which leads to defocusation of its edges, namely along the vertical axis, cf. Fig. 6.9 c). In Fig. 6.9 f), displaying the sample state after loading to 237 MPa (corresponding to ca. 2.2% of plastic deformation), one can observe pronunciation of the phenomena mentioned above, i.e., distinct boundaries of the deformation bands, highly reliefed sample surface and heavy defocusation along the vertical axis. Especially during the preceding ca. 20 MPa of loading, the

movement of material from the top and bottom of the monitored area towards its centre was observable, as is illustrated by the sequence of Figs 6.9 d), e) and f).

The high-speed camera imaging experiments have therefore enabled observation of the deformation processes dynamics, providing information about the band character of twin nucleation and the propagation of plastic deformation in general. It was revealed that, especially in the early stages of plastic deformation, the deformation is not uniformly distributed within the sample – its localisation varies across bands oriented perpendicularly to the loading direction. These results are consistent with previous experiments published in [65].

5. Discussion

5.1 Deformation behaviour

The deformation curves corresponding to the extension twinning-wise favourable combinations of sample orientation and loading direction (based on the detected texture) exhibit a so-called sigmoidal shape, which means that the initial low value of strain-hardening rate increases with advancing plastic deformation of the sample and after reaching an inflexion point, the flow curve becomes convex. This behaviour is indeed typical for deformation mediated by the $\{10\bar{1}2\} < 10\bar{1}1 >$ twinning system [66]. The above-described phenomenon is the most pronounced for the RD oriented sample deformed in compression and the ND sample deformed in tension. The flow curve shapes of the 45 oriented samples loaded in both modes are less distinct, though still exhibiting an inflexion in their deformation behaviour. In contrast, the samples oriented unfavourably for extension twinning, i.e., ND in compression and RD in tension, exhibit a distinct convex shape of flow curves through the whole deformation, which is a commonly observed behaviour for such oriented samples [67].

5.2 Neutron diffraction and AE data correlation

The distinct peaks of the acoustic emission activity in the vicinity of the yield points of the respective samples are typically ascribed to the synergic effect of the sudden increase in dislocation movement, rapid dislocation multiplication and, if present, nucleation of deformation twinning [34, 42]. The positions of the AE signal maxima coincide with the onset of the changes in intensities of diffraction peaks, related to extension twinning and, in the case of the 45 sample (where these data were available), also with the onset of the non-linear behaviour of their respective lattice strains. Combined with the comparatively lower peak values of the AE signal amplitudes and count rates measured for the ND sample, oriented unfavourably for extension twinning, this shows that the twinning nucleation represented a major contribution to the AE signal of the RD and 45 samples. However, to discriminate the AE events originating from twinning and dislocation slip and thus better grasp their individual contributions to the detected AE signal is difficult (though possible by statistical analysis of the signal) and beyond the scope of this thesis.

Muránsky et al. [34] reason the surge in twinning activity around the yield point by the so-called "autocatalytic" nature of twinning. This term describes the nucleation of twins in a given grain due to the locally increased stress level in the grain boundary caused by twins in the neighbouring grain impinging on it. This then leads to the formation of bands of twins penetrating several grain boundaries. Such cases are indeed present in the microstructures of the samples (namely the RD and 45 ones, i.e. the ones exhibiting the most pronounced AE response), even briefly after their yield points, as can be illustrated by Figs. 6.2 b) and 6.3 b) of the RD and 45 samples compressed to ca. 2.3% and 2.2% of true

plastic strain, respectively. It is therefore probable that the acoustic emission signal in these samples was augmented by this phenomenon.

Above the yield point, the AE activity decreases rapidly, which is is caused by a combination of two factors [42]:

i) The increase in dislocation density caused by the imposed strain leads to a reduction of the dislocation mean free path, which translates to a decline of the AE signal due to the proportionality between the dislocation flight path and the released AE energy [47].

ii) In compression, the twin nucleation is closely followed by a rapid twin growth [39], which is a process below the resolution of acoustic emission.

The twinned volume fraction keeps increasing even after the AE signal falls below the detection level, as is illustrated by the increase in the respective neutron diffraction peak intensities, cf. Figs 4.11 and 4.8. The twin growth-mediated TVF increase in these later stages of plastic deformation, undetected by the AE, therefore highlights the complementarity of the neutron diffraction and acoustic emission techniques – while the AE is sensitive only to twin nucleation, the neutron diffraction is sensitive to both nucleation and growth (exhibited by overall twinned volume) without distinguishing between the two.

One can observe that while the twinning onsets simultaneously in both of the parent grain orientations available to observation, the rate of increase in diffracted intensities corresponding to the different twin families differs, cf. Fig. 4.8. For both the RD and 45 oriented samples, the reorientation rate (diffracted intensities change as a result of lattice reorientation caused by twinning) is higher for the $\{10\bar{1}0\} - \{0002\}$ parent-daughter relation compared to the $\{11\bar{2}0\} - \{10\bar{1}3\}$ one. This can be explained in terms of the Schmid factor values for the activation of extension twinning in different parent grain orientations. The SF value for the $\{10\bar{1}2\} < 10\bar{1}1 >$ extension twinning in compression is 0.5 for the $\{10\bar{1}0\}$ parent grains, whereas for the $\{11\bar{2}0\}$ parent grains it is only 0.39, cf. Fig. 5.1. It, therefore, appears that while the onset of extension twinning in these grains is not significantly delayed (probably due to the lack of alternative readily activated deformation mechanisms), the rate with which the twinning proceeds is determined by the SF values of the parent grains. These results agree with those obtained by Muránsky et al. for the magnesium ZM20 alloy [34].

The lattice strain evolutions of only three reflections, $(10\bar{1}0)$, $(11\bar{2}2)$ and $(20\bar{2}1)$, were available for observation in the RD sample (as a result of the initial hot-rolling texture, cf. Fig. 4.4). The $(10\bar{1}0)$ plane lattice strain closely follows the theoretical elastic response line across the whole range of its detectability. A deviation above this line, as a consequence of the extension twinning in the $\{10\bar{1}0\}$ grain family, would be expected; however, that is not the observed behaviour (even though the twinning activity in this grain family was ample, as is evidenced by the evolution of corresponding peak intensities). The other two planes lattice strains, on the other hand, deviated above the linear dependence, indicating their soft orientation. In the case of the $(11\bar{2}2)$ reflection, this is likely caused by the slip of basal $< a >$ dislocations due to the high values of SF for

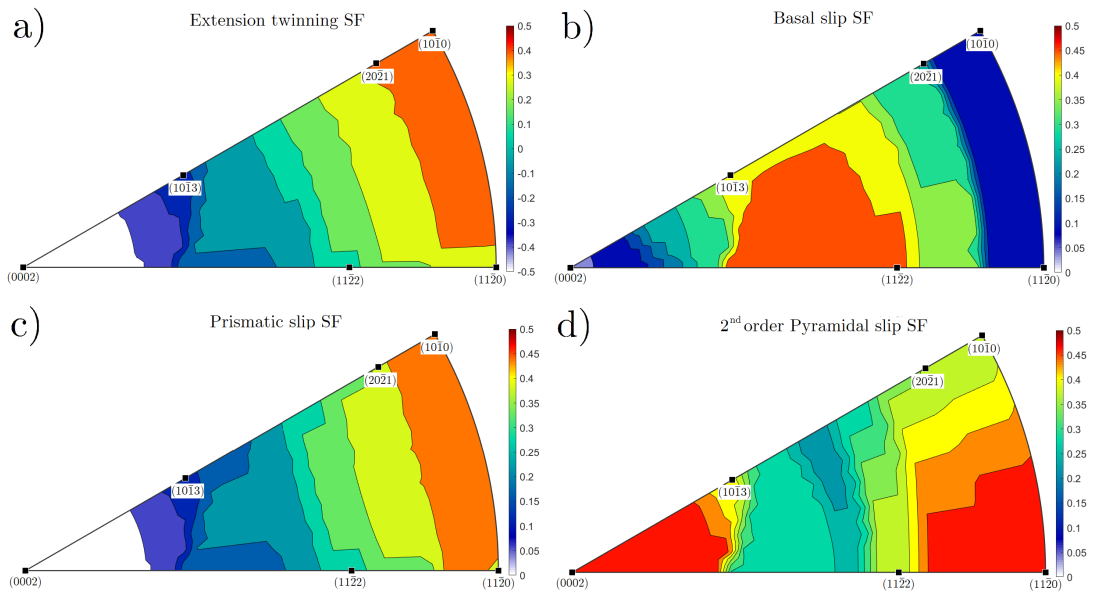

Figure 5.1: Inverse pole figures of Schmid factors for the a) $\{10\bar{1}2\} < 10\bar{1}1 >$ extension twinning in compression and the b) $\{0002\} < 11\bar{2}0 >$ basal slip, c) $\{1\bar{1}00\} < 11\bar{2}0 >$ prismatic slip and d) $\{11\bar{2}2\} < 11\bar{2}3 > 2^{\text{nd}}$ order pyramidal slip. The figures were generated using a modified script, accessible from [68], employing the MTEX 5.2.8 toolbox of the Mathworks MATLAB R2020a software.

basal slip (0.45) [69]. Considering the $(20\bar{2}1)$ planes, the basal slip SF values are lower (0.28); however, the contribution of the prismatic $< a >$ slip (SF value of 0.39) and extension twinning (SF value of 0.4) also need to be taken into account. The deviations from the elastic response took place around the macroscopic yield point and, therefore, can not be perceived as a result of microplastic behaviour. Contrary to this conclusion, the acoustic emission response of the RD sample loaded within the elastic region was quite pronounced, which is typically ascribed to the microplastic behaviour of the material [70]. It is possible that, due to its high sensitivity, the AE technique revealed a microplastic behaviour undetected by the evolution of lattice strains. However, to definitively conclude this, further, more closely focused experiments would need to be performed, which unfortunately falls beyond the scope of this thesis.

The diffraction spectra captured during the deformation of the 45 sample allowed tracking of the lattice strain evolution of all of the diffraction peaks within the angular range of the detector. In this case, the most significant deviation from the elastic response is that of the (0002) reflection, exhibiting a hard orientation. These orientations, resulting from lattice reorientation during the $\{10\bar{1}2\}$ twinning, have to accommodate larger portions of load since they are rotated out of positions favourable for either basal slip, extension twinning itself or prismatic slip, cf. Fig. 5.1. Its "counterpart", the parent $\{10\bar{1}0\}$ grains, should therefore deviate above the elastic response line; however, their diffraction peaks ceased to be detectable shortly after the macroscopic yield point, and this assumption thus can not be appropriately verified. The other observable twin daughter grain family, i.e. $\{10\bar{1}3\}$, deviates slightly above the elastic response line near the yield

point and continues to do so across the whole plastic deformation. This is likely caused by its favourable orientation for the activation of basal slip (SF value is 0.4). As for the $(11\bar{2}2)$ plane lattice strain, its deviation above the elastic response can be interpreted in terms of basal slip activation similarly to the RD sample. The lattice strain of the remaining $(20\bar{2}1)$ fluctuates near the elastic response line, and its peaks cease to be detectable shortly after the macroscopic yield point. Again, no significant evidence of microplasticity (except for two outlier points, which, however, do not match further evolutions of their respective lattice strains and are thus disregarded) was observed based on the lattice strain evolutions of the 45 sample. Similarly to the RD sample, the AE measurements revealed significant activity during the elastic deformation of this sample, which leads to the same argumentation as was presented above.

The lattice strain evolutions of the $\{10\bar{1}3\}$ and (0002) reflections during the deformation of the ND oriented sample, exhibiting significant deviations from the theoretical elastic response line, can not be entirely ascribed to the activation of the $\{10\bar{1}2\}$ extension twinning since the compressive deformation of this sample exhibited a minimal amount of twinning activity (as was confirmed not only by the negligible changes of the peak diffracted intensities but also by the EBSD experiments). The $\{10\bar{1}3\}$ grains are favourably oriented for the easily activated basal slip, which led to its lattice strain deviation above the elastic response. This microyielding occurs at stress level near the yield points of the 45 and RD samples. Since the (0002) grains are not favourably oriented for activation of any of the deformation mechanisms with comparatively low CRSS values (only for the $< c+a >$ 2^{nd} order pyramidal slip, cf. Fig. 5.1), they have to accommodate higher elastic loads, and their lattice strain thus deviates below the elastic response line at the same stress level. However, the slip of basal $< a >$ dislocations is not sufficient to meet the von Mises criterion and the activation of other deformation mechanisms, providing elongation along the $< c >$ axis is necessary. In the extension twinning-wise unfavourably oriented ND sample, this mechanism is most likely the 2^{nd} order pyramidal slip. This, therefore, leads to the significantly higher value of macroscopic yield stress compared to the 45 and RD oriented samples. The microyielding behaviour, caused by the local basal slip activity, observed in the lattice strain evolutions also explains the AE activity of the ND sample (and vice versa), which was recorded long before the macroscopic yield point was reached (cf. Fig. 4.11). The comparatively lower values of acoustic emission signal amplitudes reached during this stage of deformation (cf. Fig. 4.10) are consistent with the dislocation slip character (as opposed to yielding of the RD and 45 samples governed by twinning) of the ND sample microplasticity [52]. Similar observations of microplastic behaviour based on the combination of lattice strain deviations and acoustic emission signal were also made by other authors, e.g. [39].

5.3 Schmid factor analysis

In order to gain a further insight into the character of activated deformation mechanisms in each sample, the Schmid factors for several respective deformation mechanisms were analysed based on the measured EBSD data. The mechanisms

chosen for this analysis were the $\{0002\} < 11\bar{2}0 >$ basal slip, $\{1\bar{1}00\} < 11\bar{2}0 >$ prismatic slip, $\{11\bar{2}2\} < 11\bar{2}3 >$ 2^{nd} order pyramidal slip, $\{10\bar{1}2\} < 10\bar{1}1 >$ extension twinning and the $\{10\bar{1}1\} < 10\bar{1}\bar{2} >$ contraction twinning.

The analysis itself was done using a modified script, accessible from [71], employing the MTEX 5.2.8 toolbox of the Mathworks MATLAB R2020a software. The evaluated SF distributions of the above-listed deformation mechanisms for all three sample orientations in their initial states are shown in Fig. 5.2. The presented figures display the volume fractions corresponding to the specific SF values for a given deformation mechanism.

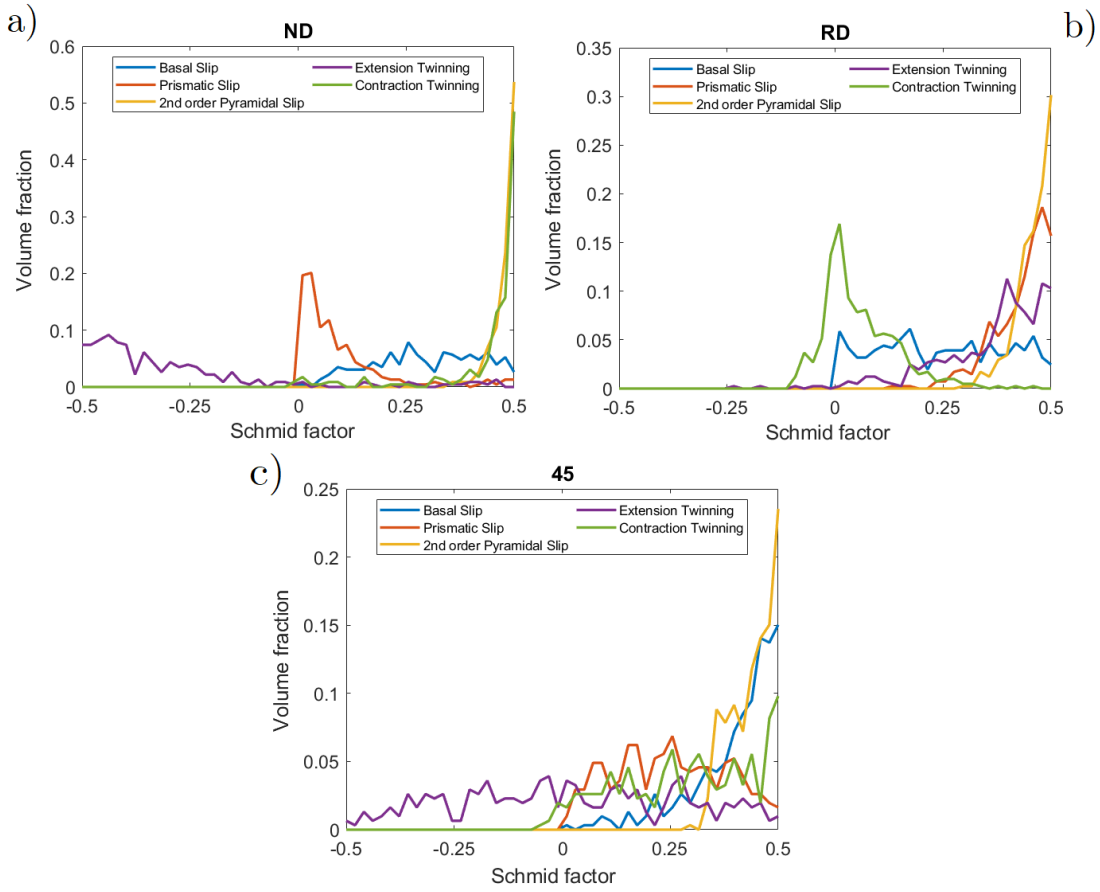

Figure 5.2: Distributions of SF for the five examined deformation mechanisms in the initial states of the a) ND oriented sample, b) RD oriented sample and c) 45 oriented sample

As expected, there is a significant difference regarding the two examined twinning mechanisms. Due to the polar nature of twinning, its Schmid factor values range from -0.5 to 0.5. Whereas the RD sample is oriented favourably for extension twinning (its SF distribution weighted average values is 0.36), the 45 sample exhibits a wide range of grains oriented both favourably and unfavourably for the activation of the $\{10\bar{1}2\} < 10\bar{1}1 >$ extension twinning (cf. Fig. 6.4 c)), yielding a weighted average SF value of 0.01. The ND sample distribution weighted average value for extension twinning is -0.19, indicating a strongly unfavourable orientation of most of its grains. In the case of the contraction twinning, it is very

much the opposite – most of the RD samples grains are oriented so that their SF values distributions form a distinct peak around the zero value (though offset very slightly towards the positive values). In contrast, in the ND sample, the contraction twinning is strongly favoured (with the distribution weighted average equal to 0.38). The orientation of grains in the 45 sample also favours the activation of the $\{10\bar{1}1\} < 10\bar{1}\bar{2} >$ contraction twinning, with the weighted average SF value of 0.29.

As for the slip mechanisms, the most significant differences are observable in the prismatic slip SF distributions, which, like the extension twinning, favours namely the RD sample. The 45 sample is favoured significantly less, and the ND sample grains are oriented quite unfavourably for the prismatic slip activation, with the weighted average values of the distributions being 0.43, 0.25 and 0.15 for the respective sample orientations. The SF distributions of the basal slip in the ND and RD samples are rather broad, yielding weighted average values of 0.31 and 0.25, respectively. In contrast, the basal slip is strongly favoured in the 45 sample (cf. Fig. 5.2 c)), averaging the SF value of 0.4. The 2$^{\text{nd}}$ order pyramidal slip is favoured in all of the studied samples.

The calculated SF values for each grain projected onto the actual sample grains (for simplicity called "SF maps" further on) in the first plastically deformed states confirmed that the extension twinning took place in the grains oriented favourably to do so, cf. the attached Figs. 6.4 a), b) and c). The extensive lattice reorientation of the RD sample, related to extension twinning affected (besides the exhaustion of the $\{10\bar{1}2\}$ twinning potential and subsequent increase in the $\{10\bar{1}1\}$ one) the Schmid factor values for basal and prismatic slip, increasing the former and decreasing the latter. This can be illustrated by the basal slip SF map of the RD sample loaded to 77 MPa shown in Fig. 6.4 d), where the twin daughter SF values are typically higher for the basal slip compared to the values of the parent grain.

The effect of lattice reorientation on Schmid factor distributions is illustrated in Fig. 5.3. These distributions correspond to the states after ca. 4.6, 5.4 and 6.2% of plastic deformation of the ND, RD and 45 samples, respectively.

The RD sample exhibits a significant change in the SF distributions of extension and contraction twinning. Due to the exhaustion of the majority of the $\{10\bar{1}2\}$ twinning potential, the high SF peak in the corresponding distribution notably diminishes. At the same time, one can observe a decrease in the area under the contraction twinning distribution peak near the zero SF value and the formation of a new peak towards the high SF values. This behaviour can be explained by the lattice reorientation connected to the extension twinning (with the daughter rotated by 86.3° respective to the parent grain), which leads to an increase in the volume of material with lattice oriented near perpendicularly to the original grains and thus being in a favourable position for the $\{10\bar{1}1\} < 10\bar{1}\bar{2} >$ contraction twinning. The fact that the extension and contraction twinning distributions of the ND sample, which exhibits only a negligible amount of twinning (and thus related lattice reorientation), show no notable change, is in accordance with this explanation. The twinning SF distributions remain virtually unaltered

also in the case of the 45 sample, which does exhibit more pronounced extension twinning activity compared to the ND sample; however, in this stage of plastic deformation, the twinned volume fraction of the 45 sample is closer to that of the ND sample, rather than that of the RD one (cf. Fig. 4.12). This means that the volume of the reoriented lattice is still quite limited and, therefore, does not lead to notable changes in the SF distributions.

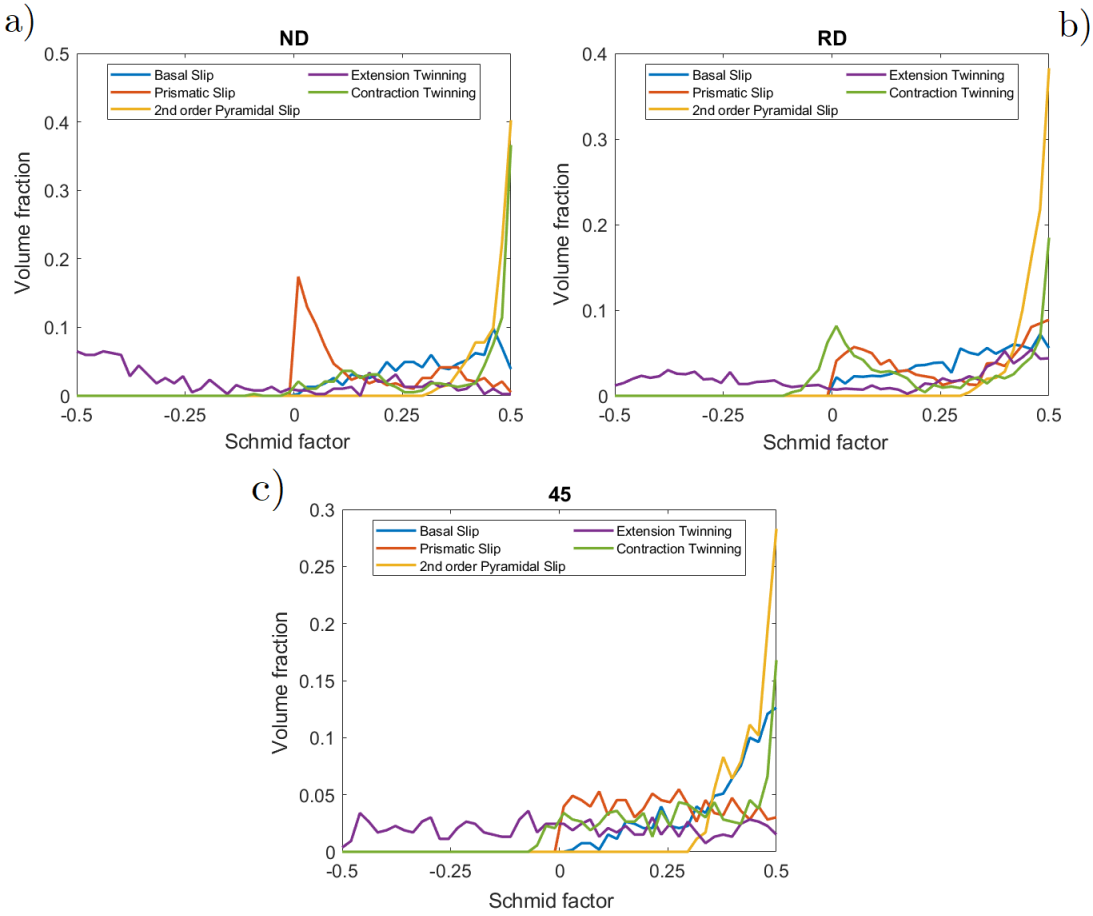

Figure 5.3: Distributions of SF for the five examined deformation mechanisms in the a) ND oriented sample loaded to 206 MPa, b) RD oriented sample loaded to 102 MPa and c) 45 oriented sample loaded to 106 MPa

The above-described observations regarding the change in the volume of material oriented favourably for basal and prismatic slip resulting from extension twinning are clearly detectable in their respective SF distributions of the RD sample. In the case of the basal slip, the weighted average value of its SF distribution increases from 0.25 to 0.31. On the other hand, the prismatic slip distribution shifts towards lower SF values – the weighted average decreases from 0.43 to 0.28 in the RD sample. As expected, the basal and prismatic SF distributions of the ND and 45 samples remain virtually unaltered. The remaining studied SF distribution, i.e., that of the 2nd order pyramidal slip, remains unchanged (and very favourable for the activation of this mechanism) across the studied range for all sample orientations.

To conclude, the Schmid factor analysis confirmed that the activation of the $\{10\bar{1}2\} < 10\bar{1}1 >$ extension twinning is closely related to the SF value of each sample grain. The lattice reorientation caused by twinning then leads to an increase in the basal slip SF distribution values, providing another readily activated mechanism, enabling further strain accommodation. This result is in agreement with the expected behaviour [21, 24]. The analysis further confirmed that the 45 sample is preferentially oriented for the basal slip. The extension twinning then provides the elongation along the $< c >$ axis necessary to sustain plastic deformation. Even though both of these samples are strongly favourably oriented for the activation of the 2$^{\text{nd}}$ order pyramidal slip, its activation is expected only in the later stages of the plastic deformation due to the comparatively high CRSS values compared to those of basal slip and extension twinning. The ND sample orientation, on the other hand, was found to significantly favour only the 2$^{\text{nd}}$ order pyramidal slip and $\{10\bar{1}1\} < 10\bar{1}\bar{2} >$ contraction twinning. Since virtually no contraction twins were observed, the macroscopic yielding of the ND sample is likely mediated by the 2$^{\text{nd}}$ order pyramidal slip, which also explains the significantly higher compressive yield stress values of the ND oriented samples compared to the RD and 45 ones.

5.4 Microstructural evolution and TVF

The EBSD microstructural observations of the loaded 45 sample have provided an insight into the dynamics of twin nucleation and growth. There was a rather small number of twinned grains observable in the state corresponding to ca. 2.2 % of plastic deformation (cf. Fig. 6.3 b), many of which contained more than one twin. The next examined state, corresponding to ca. 6.2 % of plastic deformation exhibited numerous grains which have undergone further twin nucleation, while the previously nucleated twins tended to grow. Beyond this point, virtually no further nucleations were sighted, and the twinned volume fraction increased via twin growth. This evolution agrees with the acoustic emission response of the 45 sample, which exhibited a rapid decline of AE count rate below the detectable level within the interval delimited by these two strain levels. Therefore, this rapid decline can be ascribed to the exhaustion of twin nucleation potential (coupled with the reduction of the dislocation mean free path, caused by the increased density of dislocations and twin boundaries).

Analogous reasoning can likely be applied to explain the similar (albeit more gradual) decrease in the AE activity of the RD sample. However, due to the extensive $\{10\bar{1}2\}$ twinning activity in this sample, it is impossible to differentiate between twin nucleation and growth from the EBSD microstructural observations as clearly as in the 45 sample.

Due to the above-mentioned complexity of the quantitative analysis of the deformed RD sample microstructure, the EBSD-based twinned volume fraction analysis provides only two data points, corresponding to 2.3 and 5.4% of plastic deformation, which indicate a rapid TVF increase. The evolution of the normalised integrated intensities of the twinning-related neutron diffraction peaks suggests that the twinned volume fraction continues to increase even beyond this

level of strain. However, the rate of the increase diminishes and at the 7.8% plastic strain mark, the TVF level is saturated, cf. Fig. 4.8 b).

The comparison of the peak integrated intensities evolution of the 45 sample, presented in Fig. 4.8 c), with the EBSD-based twinned volume fraction analysis (Fig. 4.12), shows that the results are in a good qualitative agreement. The gradual TVF increase reaches significantly lower values than the RD sample and saturates at ca. 12% of plastic deformation. However, to conduct a more thorough comparison of the results obtained by these methods (and thus possibly study the influence of sample surface versus bulk on the twinning behaviour), higher data point density and, namely, the quantification of the neutron diffraction-based twinned volume fraction data would be necessary. This, however, exceeds the scope of this thesis.

5.5 Symmetry within the sheet plane

The detected texture strongly resembles that of the hot-rolled magnesium alloy, cf. Figs. 4.4 and 1.10, which is caused by the specific temperature profile used in the preparation of the investigated material. This means that the distributions of the $\{10\bar{1}0\}$ and $\{11\bar{2}0\}$ poles within the sheet plane are random. The three sample orientations, RD, ND and 45° between RD and ND, have therefore been selected to study the role of sample orientation with respect to the $\{0001\}$ poles and the role of orientation within the RD × TD plane was not taken into account in this choice. However, to experimentally verify the assumption of uniform mechanical behaviour regardless of the rotation around the ND axis within the sheet plane, a control group of samples was machined and subjected to the same testing procedures. The orientation of these samples was selected to be 30° between RD and TD (further on denoted as 30 for simplicity) in order to avoid the possible effect of the hcp unit cell six-fold symmetry around the *c*-axis (leading to the six-fold symmetry of the $\{10\bar{1}0\}$ poles in the warm-rolled texture of AZ31 alloys).

The deformation curves of the RD and 30 oriented samples exhibit very similar behaviour in both compression and tension. The compressive deformation curves have the sigmoidal shape typical for extensive activation of the $\{10\bar{1}2\} < 10\bar{1}1 >$ twinning system [66]. In contrast, the tensile curves exhibit ca. double values of yield stress compared to compression and remain convex during the whole deformation process, cf. Fig. 5.4 a). The compressive and tensile yield stress values of the two sample orientations are the same within the experimental error.

Although the mechanical behaviour of the RD and 30 samples display very little difference, the results of their $\{10\bar{1}2\}$ twinning-related peak intensities changes vary quite significantly. The qualitative character of the respective evolutions is the same – the onset of the changes matches the macroscopic yield points, the rate of intensity changes follows the SF values of the individual parent grains, and the phenomenon saturates at similar stress levels. However, the normalised integrated intensities of both the $\{0002\}$ and $\{10\bar{1}3\}$ peaks saturate at lower values (by a factor of approximately 2.5) for the 30 sample compared to the RD one, which indicates that the overall twinned volume fraction is lower in the 30 sample

than in the RD. However, the neutron diffraction intensity change results do not agree with the twinned volume fraction analysis based on the EBSD twinning parent-daughter maps, cf. Figs. 5.4 b) and c), where both the 30 and RD sample exhibit a similarly rapid increase in areas corresponding to the $\{10\bar{1}2\}$ extension twins.

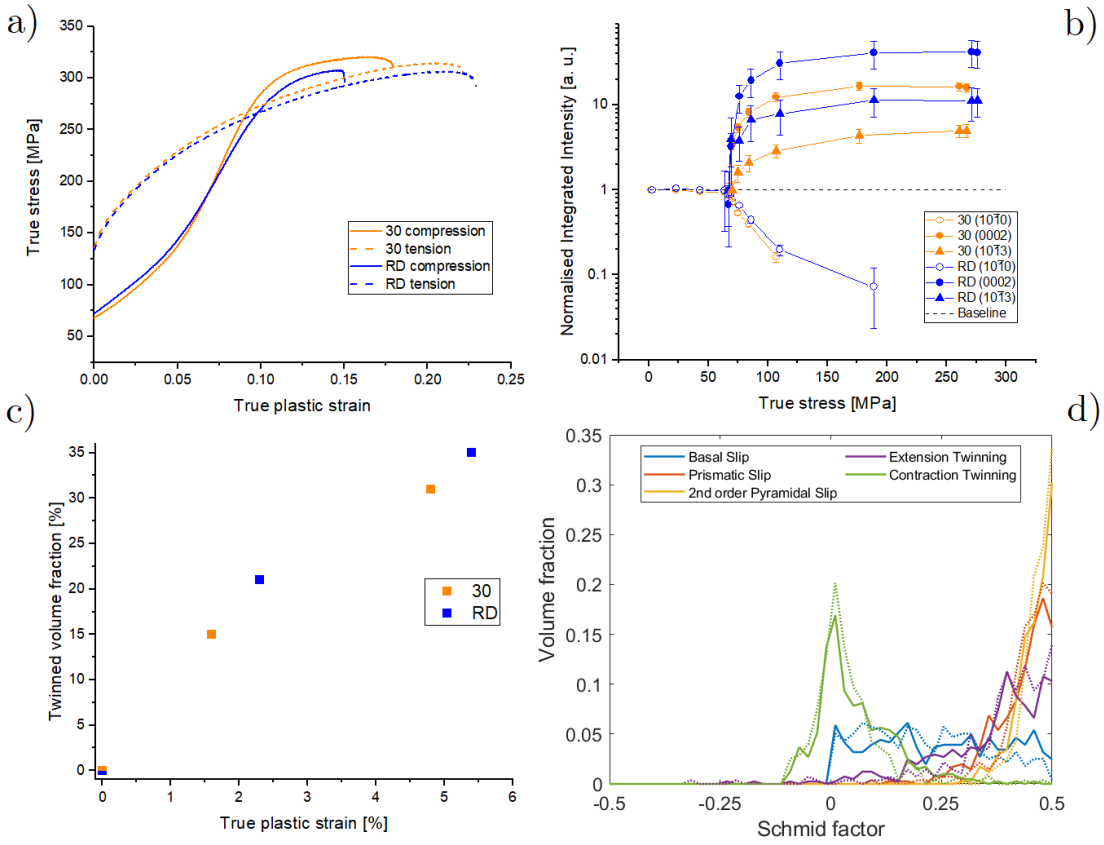

Figure 5.4: Comparison of the a) compressive and tensile deformation curves, b) normalised integrated intensities of selected diffraction peaks, c) EBSD-based twinned volume fraction analysis and d) distributions of SF for several deformation mechanisms of the RD and 30 oriented samples. The SF distributions of the RD sample in d) are marked by full lines and those of the 30 sample by dotted lines; the colour legend is the same for both samples.

To decisively conclude whether this dissent genuinely originates from the material behaviour or if it is merely a result of inaccuracy of the employed techniques and data processing, more measurements would have to be performed. This, however, falls beyond the extend of this thesis. The comparison of the SF distributions of the RD and 30 sample, presented in Fig. 5.4 d), then confirms the expected similarity of the two samples – they are both oriented favourably namely for the activation of $\{10\bar{1}2\} < 10\bar{1}1 >$ extension twinning, which is believed to govern their macroscopic yielding during the compressive deformation, and also for the activation of the $\{1\bar{1}00\} < 11\bar{2}0 >$ prismatic and $\{11\bar{2}2\} < 11\bar{2}3 >$ 2^{nd} order pyramidal slip. However, the CRSS values of these two slip systems are significantly higher than that of the extension twinning, meaning they can be

expected to play important roles only in the later stages of plastic deformation of these samples.

5.6 Deformation bands

The band-like character of twin nucleation around the yield point, advancing through the sample in the loading direction, which was observed by the high-speed camera during the deformation of the RD sample (and to a certain extent also of the 45 oriented one), was also observed during the in-situ EBSD measurements of the 45 oriented sample. A clear example of such deformation bands formed perpendicularly to the loading direction is visible in Fig. 5.5, displaying a SEM secondary electron image of the 45 sample surface after loading to 106 MPa (ca. 6.2% of plastic strain). Such behaviour is generally consistent with the Lüders phenomenon. However, the defining behaviour of the Lüders phenomenon, i.e., the presence of a plateau in the stress-strain curve following yielding, was not observed.

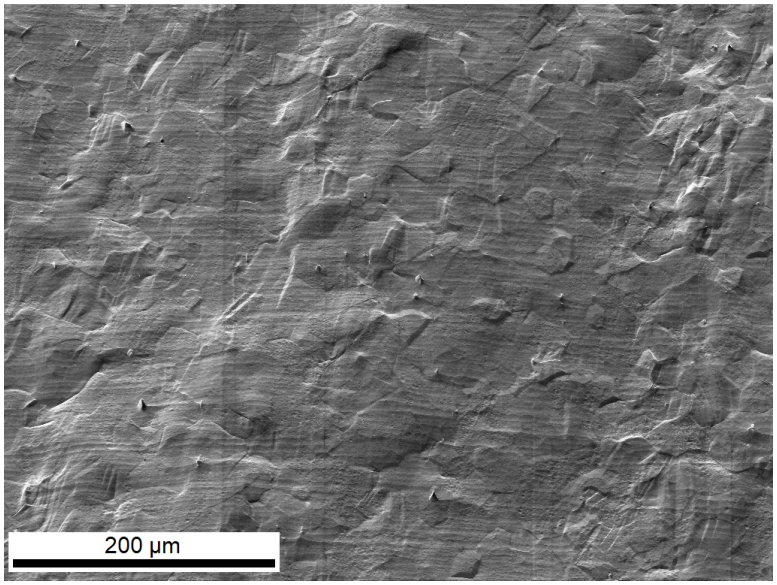

Figure 5.5: Deformation bands formed during loading of the 45 sample. The sample was compressed in the horizontal direction.

Barnett et al. made similar observations in the study [72], which focused on the influence of grain size of an extruded magnesium AZ31 alloy on the magnitude of the Lüders strain. Due to the extrusion texture, the Lüders phenomenon, observed during uniaxial compression along the extrusion direction, was linked to yielding mediated by extension twinning. The authors observed no yield plateau on the stress-strain curve of a coarse-grained sample (with an average grain diameter of 55 µm), whereas, for samples with grain sizes of 15 µm and lower, yield plateaus were observed. However, the microstructure of the coarse-grained sample exhibited a significant population of twins, propagating from the sample edges in the loading direction as the load increased. The authors reason this behaviour as follows [72, 73]:

i) The presence of friction and possible irregularities in sample dimensions leads to higher values of stress at the contact of the sample and the platens, causing an earlier formation of extension twins on the sample edges as a result of material yielding.

ii) Further formation of extension twins does not result from the necessity for stress relaxation caused by twin formation in a neighbouring grain. This is the presumed mechanism of Lüders band propagation (leading to the stress-plateau formation, since no increase in stress is necessary to further accommodate the strain).

iii) Instead, to form these additional twins (and thus accommodate the imposed strain), an increase in stress is necessary for new "sources" in the grain boundaries to be activated.

iv) The requirement for Lüders elongation, i.e., a yield plateau in the stress-strain curve, is, therefore, not met.

The same line of reasoning can be used to explain the behaviour observed by the high-speed camera during the compressive deformation of the RD and 45 samples and the absence of Lüders elongation (considering the average grain size of the studied material is 31 µm). On the other hand, the ND sample exhibits no observable twinning due to its yielding being mediated by slip mechanisms.

It is, however, true for all of the studied sample orientations that rather significant inhomogeneities of plastic deformation were observed. It is quite possible that the deformation would be more uniform should another sample geometry be used (e.g., cylindrical samples, such that were employed in the above mentioned study [72]); however, experiments comparing these influences fall beyond the scope of this study.

The influence of such inhomogeneities could potentially skew the results obtained by local methods, such as the in-situ EBSD (especially if several different samples or surface areas are not examined). On the other hand, the "bulk" methods, averaging data from the whole sample volume (such as the neutron diffraction), should not be severely affected by possible inhomogeneities of the plastic behaviour. This fact, therefore, needs to be taken into question when an experiment aiming to comprehensively investigate the deformation behaviour of any given material is devised.

Conclusion

In the present work, the correlation between texture and the activity of deformation mechanisms in a rolled magnesium AZ31 alloy was investigated, using a combination of advanced in-situ experimental techniques, including neutron diffraction, acoustic emission, electron backscatter diffraction and high-speed camera imaging.

The most important results of this investigation can be summarised as follows:

- The detected texture of the AZ31 magnesium sheet has exhibited the typical features of the hot-rolled magnesium alloy textures. The experiments presented in this thesis have proven the crucial role of sample orientation with respect to the $\{0001\}$ poles on mechanical behaviour. The independence of sample behaviour on its orientation within the sheet plane, suggested by the detected texture, was also experimentally verified.
- A combination of direct and indirect observations has confirmed that the macroscopic yielding during compressive deformation of the RD and 45 samples was mediated by the extension twinning, while in the ND oriented sample, the yielding was mediated by the 2^{nd} order pyramidal slip. This difference was, among other aspects, manifested by more than double values of compressive yield stress observed for the ND sample compared to those of the RD and 45 samples, which were very similar to each other.
- A consistent link between the AE response, neutron diffraction changes of diffracted intensities and EBSD-based observations of microstructural changes, describing the evolution of twinning in the RD and 45 samples, was found.
- The twinned volume fraction was analysed utilising the neutron diffraction and in-situ EBSD measurements. In accordance with the AE response, it was confirmed that the rapid TVF increase in the early stages of plastic deformation could be ascribed to twin nucleation. The increase caused by twin growth, on the other hand, is more gradual and does not produce a detectable AE signal.
- While the activity of the $\{10\bar{1}2\}$ extension twinning was ample in the RD and 45 samples and observable in the ND sample as well, virtually no $\{10\bar{1}1\}$ contraction or $\{10\bar{1}1\} - \{10\bar{1}2\}$ double twinning was observed in any of the studied samples.
- The microplastic behaviour of the ND sample was observed both by acoustic emission and neutron diffraction techniques. The AE signal suggested similar behaviour also in the 45 and RD samples. However, this was not confirmed by the neutron diffraction-based lattice strain analysis.
- Formation of deformation bands, oriented perpendicularly to the loading direction, was observed during the compressive loading of the samples. Such inhomogeneities may lead to skewed results when only local experimental techniques are employed.

Future prospects

The obtained results demonstrate the great promise of employing mutually complementary in-situ methods to analyse the deformation behaviour of metals. Several areas could be the subject of future research to provide answers for the remaining open questions. The following research options may be of particular interest:

- Quantification of the twinned volume fraction from the neutron diffraction experiments (similarly to, e.g. [74]), allowing the comparison with results obtained from the EBSD data, and discussion of the role of sample surface versus bulk on the twinning behaviour.
- Application of a spectrum-based analysis of the acoustic emission signal (such as the adaptive sequential $k-$means procedure [55]), enabling the differentiation of different AE signal sources and thus providing further insight into the role of individual deformation mechanisms.
- Utilising the digital image correlation (DIC) technique to study the heterogeneities during deformation of polycrystalline materials (such as the deformation bands observed in this thesis), arising from incompatibilities between grains. Such a DIC-based study was recently performed on the AZ31 magnesium alloy by Orozco-Caballero et al. [75].
- Investigation of the role of local microstructure on the activation of different deformation modes by employing the EBSD-assisted trace analysis during the in-situ SEM testing. An example of such a study, performed on magnesium single crystals, is the work of Cepeda-Jiménez et al. [76].

Bibliography

[1] Nai Mui Ling Gupta. *Magnesium, Magnesium Alloys, and Magnesium Composites*. John Wiley & Sons, 2011.

[2] B. L. Mordike and T. Ebert. Magnesium. *Materials Science and Engineering: A*, 302(1):37–45, April 2001.

[3] Matthew A. Steiner, Jishnu J. Bhattacharyya, and Sean R. Agnew. The Relative Contributions of Deformation Modes to AZ31 Rolling Textures in Different Temperature Regimes. In *The Minerals, Metals & Materials Series*, pages 555–561. Springer International Publishing, 2017.

[4] M.R. Barnett, A. Sullivan, N. Stanford, N. Ross, and A. Beer. Texture selection mechanisms in uniaxially extruded magnesium alloys. *Scripta Materialia*, 63(7):721–724, October 2010.

[5] A. A. Yaroshevsky. Abundances of Chemical Elements in the Earth's Crust. *Geochemistry International*, 44(1):48–55, January 2006.

[6] F. W. von Batchelder and R. F. Raeuchle. Lattice Constants and Brillouin Zone Overlap in Dilute Magnesium Alloys. *Physical Review*, 105(1):59–61, January 1957.

[7] Charles Kittel. *Introduction to Solid State Physics*. WILEY, 2004.

[8] Jianguo Lin. *Microstructure evolution in metal forming processes : modelling and applications*. Woodhead Pub, Cambridge, 2012.

[9] K. H. J. Buschow. *Encyclopedia of Materials : Science and Technology*. Elsevier, Amsterdam, 2001.

[10] Z. Yang, J. Li, J. Zhang, G. Lorimer, and J. Robson. Review on Research and Development of Magnesium Alloys. *Acta Metallurgica Sinica (English Letters)*, 21(5):313–328, October 2008.

[11] William Hosford. *Mechanical Behavior of Materials*. Cambridge University Press, Cambridge New York, 2010.

[12] Günter Gottstein. *Physical Foundations of Materials Science*. Springer Berlin Heidelberg, Berlin, Heidelberg, 2004.

[13] M. H. Yoo. Slip, Twinning, and Fracture in Hexagonal Close-Packed Metals. *Metallurgical Transactions A*, 12(3):409–418, March 1981.

[14] T. B. Britton, F. P. E. Dunne, and A. J. Wilkinson. On the mechanistic basis of deformation at the microscale in hexagonal close-packed metals. *Proceedings of the Royal Society A: Mathematical, Physical and Engineering Sciences*, 471(2178):20140881, June 2015.

[15] E. Schmid and G. Wassermann. Über die Textur gezogener Magnesium- und Zinkdrähte. *Die Naturwissenschaften*, 17(18-19):312–314, May 1929.

[16] J. Koike and R. Ohyama. Geometrical criterion for the activation of prismatic slip in AZ61 Mg alloy sheets deformed at room temperature. *Acta Materialia*, 53(7):1963–1972, April 2005.

[17] Sean R. Agnew and Özgür Duygulu. Plastic anisotropy and the role of non-basal slip in magnesium alloy AZ31B. *International Journal of Plasticity*, 21(6):1161–1193, June 2005.

[18] Adrien Chapuis and Julian H. Driver. Temperature dependency of slip and twinning in plane strain compressed magnesium single crystals. *Acta Materialia*, 59(5):1986–1994, March 2011.

[19] Jan Čapek, Michal Knapek, Peter Minárik, Jan Dittrich, and Kristián Máthis. Characterization of Deformation Mechanisms in Mg Alloys by Advanced Acoustic Emission Methods. *Metals*, 8(8):644, August 2018.

[20] R. von Mises. Mechanik der plastischen Formänderung von Kristallen. *ZAMM - Zeitschrift für Angewandte Mathematik und Mechanik*, 8(3):161–185, 1928.

[21] J.W. Christian and S. Mahajan. Deformation twinning. *Progress in Materials Science*, 39(1-2):1–157, 1995.

[22] B. A. Bilby and A. G. Crocker. The Theory of the Crystallography of Deformation Twinning. *Proceedings of the Royal Society of London. Series A. Mathematical and Physical Sciences*, 288(1413):240–255, October 1965.

[23] Akio Ishii, Ju Li, and Shigenobu Ogata. Shuffling-controlled versus strain-controlled deformation twinning: The case for HCP Mg twin nucleation. *International Journal of Plasticity*, 82:32–43, July 2016.

[24] M. R. Barnett. Twinning and the ductility of magnesium alloys: Part I: "Tension" twins. *Materials Science and Engineering: A*, 464(1-2):1–7, 2007.

[25] M. R. Barnett. Twinning and the ductility of magnesium alloys: Part II: "Contraction" twins. *Materials Science and Engineering: A*, 464(1-2):8–16, 2007.

[26] Wei Wu, Chih Pin Chuang, Dongxiao Qiao, Yang Ren, and Ke An. Investigation of deformation twinning under complex stress states in a rolled magnesium alloy. *Journal of Alloys and Compounds*, 683:619–633, October 2016.

[27] E. W. Kelley and W. F. Hosford. The Deformation Characteristics of Textured Magnesium. *Transactions of the Metalurgical Society of Aime*, 242:654–661, April 1968.

[28] M.R. Barnett. A rationale for the strong dependence of mechanical twinning on grain size. *Scripta Materialia*, 59(7):696–698, October 2008.

[29] J. Wang, I.J. Beyerlein, and C.N. Tomé. An atomic and probabilistic perspective on twin nucleation in Mg. *Scripta Materialia*, 63(7):741–746, October 2010.

[30] A. Vinogradov, E. Vasilev, M. Seleznev, K. Máthis, D. Orlov, and D. Merson. On the limits of acoustic emission detectability for twinning. *Materials Letters*, 183:417–419, November 2016.

[31] Colleen Bettles. *Advances in wrought magnesium alloys: Fundamentals of processing, properties and applications*. Woodhead Pub, Philadelphia, Pa, 2012.

[32] Eitaro Yukutake, Junichi Kaneko, and Makoto Sugamata. Anisotropy and Non-Uniformity in Plastic Behavior of AZ31 Magnesium Alloy Plates. *Materials Transactions*, 44(4):452–457, 2003.

[33] Aravindha R. Antoniswamy, Jon T. Carter, Louis G. Hector, and Eric M. Taleff. Static Recrystallization and Grain Growth in AZ31B-H24 Magnesium Alloy Sheet. In *Magnesium Technology 2014*, pages 139–142. Springer International Publishing, 2014.

[34] O. Muránsky, M.R. Barnett, D.G. Carr, S.C. Vogel, and E.C. Oliver. Investigation of deformation twinning in a fine-grained and coarse-grained ZM20 mg alloy: Combined in situ neutron diffraction and acoustic emission. *Acta Materialia*, 58(5):1503–1517, March 2010.

[35] George Edward Bacon. *Neutron Diffraction*. Clarendon Press, Oxford England, 1975.

[36] W. L. Bragg. The Structure of Some Crystals as Indicated by Their Diffraction of x-rays. *Proceedings of the Royal Society of London. Series A, Containing Papers of a Mathematical and Physical Character*, 89(610):248–277, September 1913.

[37] B. K. Vainshtein. *Fundamentals of Crystals: Symmetry, and Methods of Structural Crystallography*. Springer, Berlin, 1994.

[38] Michael Hutchings. *Introduction to the Characterization of Residual Stress by Neutron Diffraction*. Taylor & Francis, Boca Raton, FL, 2005.

[39] Jan Čapek, Kristián Máthis, Bjørn Clausen, Jitka Stráská, Přemysl Beran, and Petr Lukáš. Study of the loading mode dependence of the twinning in random textured cast magnesium by acoustic emission and neutron diffraction methods. *Materials Science and Engineering: A*, 602:25–32, April 2014.

[40] S.R. Agnew, C.N. Tomé, D.W. Brown, T.M. Holden, and S.C. Vogel. Study of slip mechanisms in a magnesium alloy by neutron diffraction and modeling. *Scripta Materialia*, 48(8):1003–1008, April 2003.

[41] Y.B. Chun and C.H.J. Davies. Texture effect on microyielding of wrought magnesium alloy AZ31. *Materials Science and Engineering: A*, 528(9):3489–3495, April 2011.

[42] K. Máthis, J. Čapek, B. Clausen, T. Krajňák, and D. Nagarajan. Investigation of the dependence of deformation mechanisms on solute content in polycrystalline Mg–Al magnesium alloys by neutron diffraction and acoustic emission. *Journal of Alloys and Compounds*, 642:185–191, September 2015.

[43] Mikhail A. Krivoglaz. *X-Ray and Neutron Diffraction in Nonideal Crystals*. Springer Berlin Heidelberg, 2011.

[44] H. J. Bunge. Advantages of Neutron Diffraction in Texture Analysis. *Textures and Microstructures*, 10(4):265–307, January 1989.

[45] D. Copley, John R. *The Fundamentals of Neutron Powder Diffraction*. National Institute of Standarts and Technology, November 2001.

[46] C. R. Heiple, S. H. Carpenter, and M. J. Carr. Acoustic emission from dislocation motion in precipitation-strengthened alloys. *Metal Science*, 15(11-12):587–598, November 1981.

[47] M. Friesel and S. H. Carpenter. Determination of the Source of Acoustic Emission Generated during the Deformation of Magnesium. *Journal of acoustic emission*, 3:11–17, 1984.

[48] C.R. Heiple and S.H. Carpenter. Acoustic Emission Produced by Deformation of Metals and Alloys - A review: Part I. *Journal of Acoustic Emission*, 6:177–204, 1987.

[49] C.R. Heiple and S.H. Carpenter. Acoustic Emission Produced by Deformation of Metals and Alloys - A review: Part II. *Journal of Acoustic Emission*, 6:177–204, 1987.

[50] Michal Knapek. *Study of cooperative dislocation phenomena in solids by the acoustic emission technique*. PhD thesis, Charles University, 2016.

[51] Jan Čapek. *Investigation of basic deformation mechanisms of magnesium alloys by means of advanced in-situ methods and theoretical modeling*. PhD thesis, Charles University, 2017.

[52] Daria Drozdenko, Jan Bohlen, František Chmelík, Pavel Lukáč, and Patrik Dobroň. Acoustic emission study on the activity of slip and twin mechanisms during compression testing of magnesium single crystals. *Materials Science and Engineering: A*, 650:20–27, January 2016.

[53] Enrique Meza-García, Patrik Dobroň, Jan Bohlen, Dietmar Letzig, František Chmelík, Pavel Lukáč, and Karl Ulrich Kainer. Deformation mechanisms in an AZ31 cast magnesium alloy as investigated by the acoustic emission technique. *Materials Science and Engineering: A*, 462(1-2):297–301, July 2007.

[54] C. Scruby, H. Wadley, and J. E. Sinclair. The origin of acoustic emission during deformation of aluminium and an aluminium–magnesium alloy. *Philosophical Magazine A*, 44(2):249–274, August 1981.

[55] Eraldo Pomponi and Alexei Vinogradov. A real-time approach to acoustic emission clustering. *Mechanical Systems and Signal Processing*, 40(2):791–804, July 2013.

[56] Gergely Farkas. *Investigation of residual stresses and deformation mechanisms of magnesium-based composites by means of neutron diffraction and acoustic emission methods*. PhD thesis, Charles University, 2017.

[57] Anwar Ul-Hamid. *A Beginners' Guide to Scanning Electron Microscopy*. Springer-Verlag GmbH, 2018.

[58] István Zoltán Jenei. Scanning electron microscopy (SEM) analysis of tribofilms enhanced by fullerene-like nanoparticles, 2012.

[59] Wikimedia Commons. Interaction volume in scanning electron microscopy, 2015. File: Pear interaction SEM english.png.

[60] B. Fultz and J. Howe. *Transmission Electron Microscopy and Diffractometry of Materials*. Springer-Verlag GmbH, 2012.

[61] David B. Williams and C. Barry Carter. *Transmission Electron Microscopy*. Springer-Verlag GmbH, 2009.

[62] Richard O. Duda and Peter E. Hart. Use of the Hough Transformation to Detect Lines and Curves in Pictures. *Communications of the ACM*, 15(1):11–15, January 1972.

[63] Stuart I. Wright and Brent L. Adams. Automatic Analysis of Electron Backscatter Diffraction Patterns. *Metallurgical Transactions A*, 23(3):759–767, March 1992.

[64] I. J. Beyerlein, J. Wang, M. R. Barnett, and C. N. Tomé. Double twinning mechanisms in magnesium alloys via dissociation of lattice dislocations. *Proceedings of the Royal Society A: Mathematical, Physical and Engineering Sciences*, 468(2141):1496–1520, February 2012.

[65] Jan Čapek, Jan Dittrich, and Peter Minárik. Effect of the loading mode and orientation on the development of deformation mechanisms in the rolled AZ31. In *Proceedings 27th International Conference on Metallurgy and Materials*, pages 1513 – 1519, October 2018.

[66] K. Eswar Prasad, B. Li, N. Dixit, M. Shaffer, S. N. Mathaudhu, and K. T. Ramesh. The Dynamic Flow and Failure Behavior of Magnesium and Magnesium Alloys. *JOM*, 66(2):291–304, January 2014.

[67] Y.R. Zhao, L.L. Chang, J. Guo, and Y.P. Jin. Twinning behavior of hot extruded AZ31 hexagonal prisms during uniaxial compression. *Journal of Magnesium and Alloys*, 7(1):90–97, March 2019.

[68] MTEX script for the PF and IPF of Schmid factor in Mg. `https://gist.github.com/jhiscocks/cb20963900ea010aa9927d464cf896ba`. Accessed: 15. 05. 2021.

[69] S.R. Agnew, C.N. Tomé, and D.W. Brown. Validating a polycrystal model for the elastoplastic response of magnesium alloy AZ31 using in situ neutron diffraction. *Acta Materialia*, 54(18):4841–4852, October 2006.

[70] Alexei Vinogradov, Dmitry Orlov, Alexei Danyuk, and Yuri Estrin. Effect of grain size on the mechanisms of plastic deformation in wrought Mg–Zn–Zr alloy revealed by acoustic emission measurements. *Acta Materialia*, 61(6):2044–2056, April 2013.

[71] MTEX – The Schmid Factor. `https://mtex-toolbox.github.io/SchmidtFactor.html`. Accessed: 02. 04. 2021.

[72] Matthew R. Barnett, Mark D. Nave, and Alireza Ghaderi. Yield point elongation due to twinning in a magnesium alloy. *Acta Materialia*, 60(4):1433–1443, February 2012.

[73] D.W. Moon. Considerations on the Present State of Lüders Band Studies. *Materials Science and Engineering*, 8(4):235–243, October 1971.

[74] B. Clausen, C.N. Tomé, D.W. Brown, and S.R. Agnew. Reorientation and stress relaxation due to twinning: Modeling and experimental characterization for Mg. *Acta Materialia*, 56(11):2456–2468, June 2008.

[75] Alberto Orozco-Caballero, David Lunt, Joseph D. Robson, and João Quinta da Fonseca. How magnesium accommodates local deformation incompatibility: A high-resolution digital image correlation study. *Acta Materialia*, 133:367–379, July 2017.

[76] C.M. Cepeda-Jiménez, J.M. Molina-Aldareguia, and M.T. Pérez-Prado. EBSD-Assisted Slip Trace Analysis During In Situ SEM Mechanical Testing: Application to Unravel Grain Size Effects on Plasticity of Pure Mg Polycrystals. *JOM*, 68(1):116–126, July 2015.

List of Figures

List of Tables

List of Abbreviations

30	orientation of 30° between rolling and transversal direction
45	orientation of 45° between rolling and normal direction
AE	acoustic emission
AZ31	magnesium alloy (3 wt. % Al, 0.8 wt. % Zn, 0.2 wt. % Zn)
BSE	backscattered electrons
CI	confidence index
CRSS	critical resolved shear stress
DIC	digital image correlation technique
EBSD	electron backscatter diffraction
fcc	face-centred cubic structure
FEG	field emission gun
FWHM	full width at half maximum
GOS	grain orientation spread
hcp	hexagonal close-packed structure
HDT	hit definition time of an acoustic emission event
HLT	hit lockout time of an acoustic emission event
IPF	inverse pole figure
ND	normal direction
PF	pole figure
RD	rolling direction
RT	room temperature
SE	secondary electrons
SEM	scanning electron microscopy
SF	Schmid factor
TD	transversal direction
TVF	twinned volume fraction

6. Attachments

6.1 IPF orientation maps

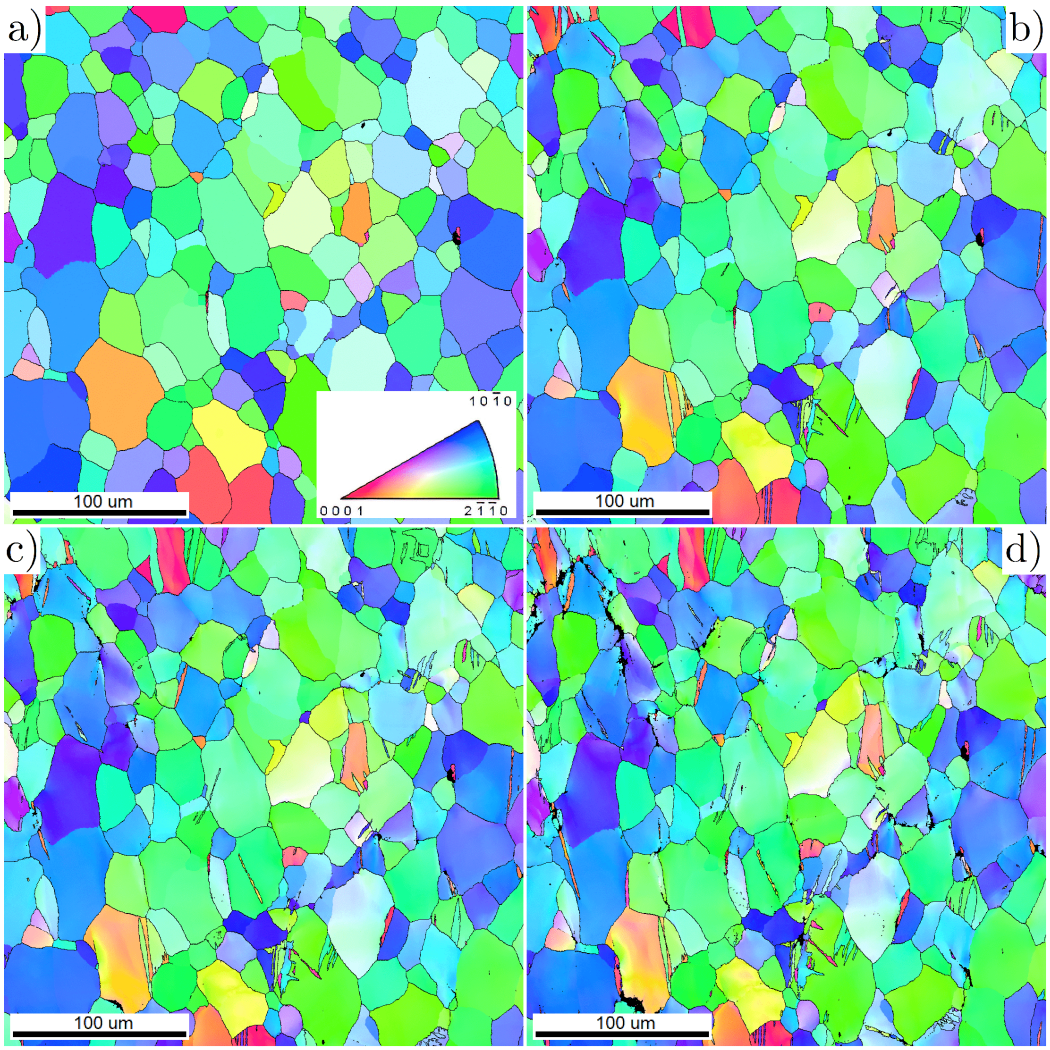

Figure 6.1: IPF orientation maps of the ND oriented sample, corresponding to a) the initial state, i.e., preloaded to 9 MPa, b) the state after loading to 163 MPa, c) the state after loading to 188 MPa and d) the state after loading to 206 MPa. The colour legend shown in a) is the same for all of the figures. The sample was compressed in the horizontal direction.

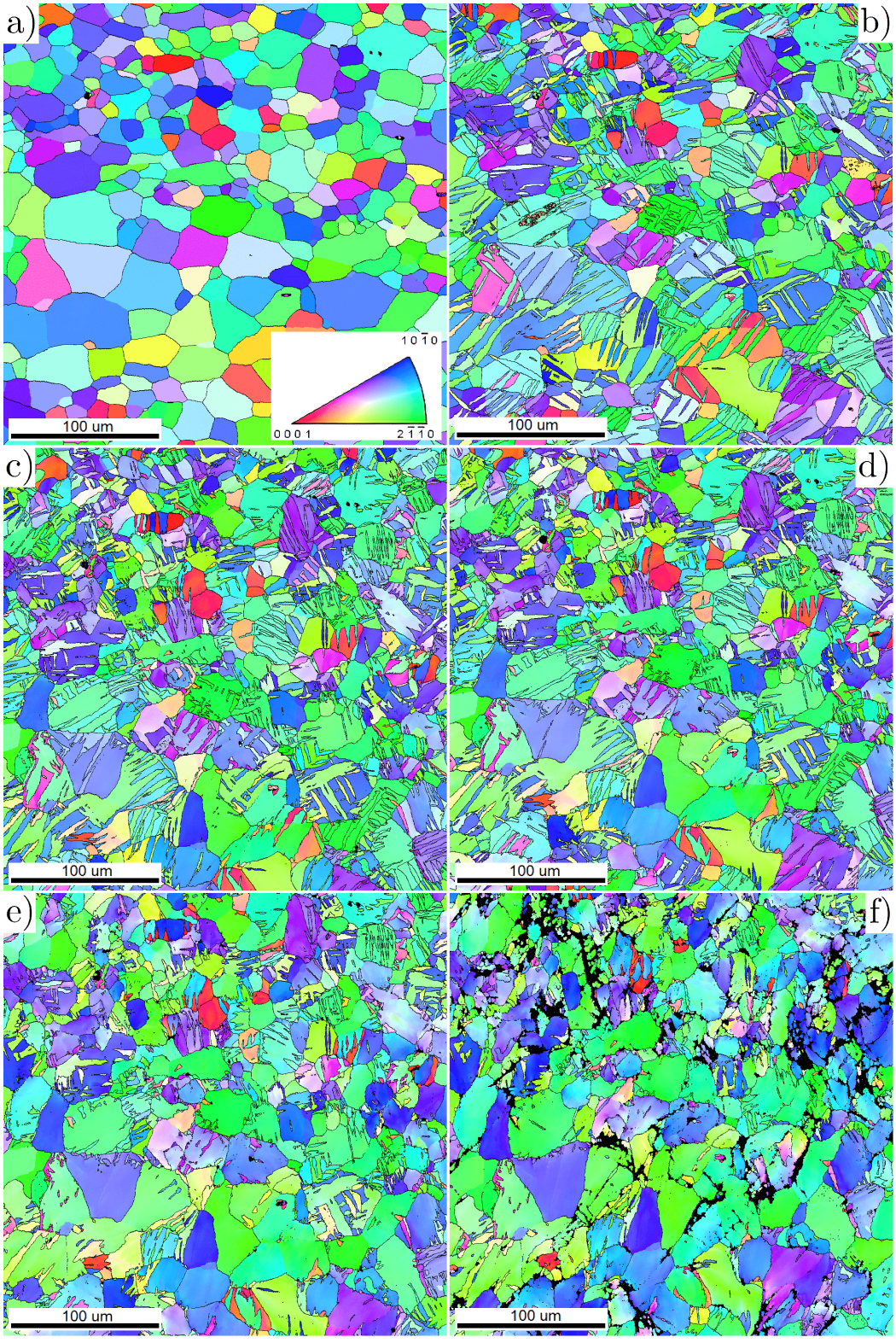

Figure 6.2: IPF orientation maps of the RD oriented sample, corresponding to a) the initial state, i.e., preloaded to 11 MPa, b) the state after loading to 77 MPa, c) the state after loading to 102 MPa, d) the state after loading to 127 MPa, e) the state after loading to 190 MPa and f) the state after loading to 230 MPa. The colour legend shown in a) is the same for all of the figures. The sample was compressed in the horizontal direction.

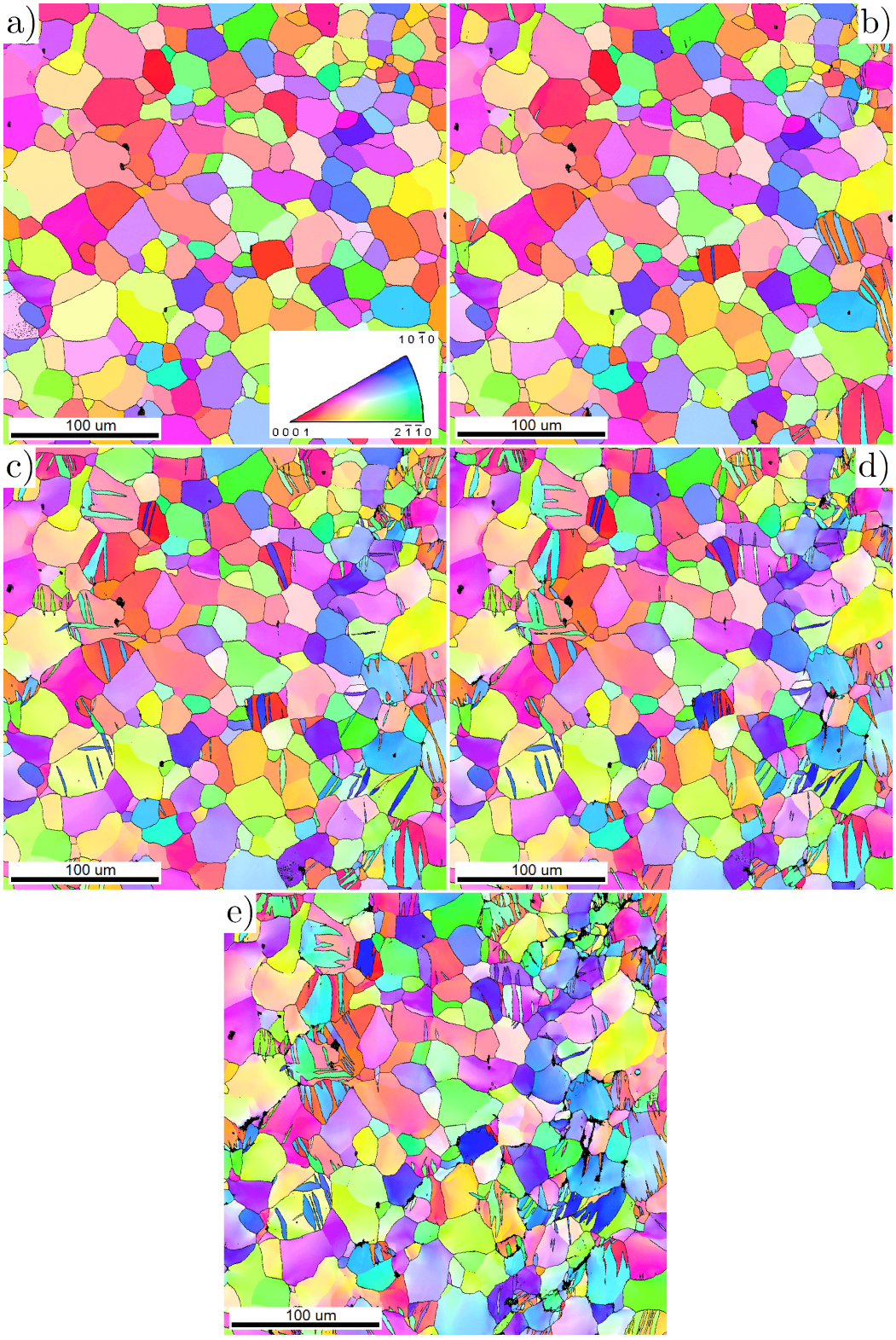

Figure 6.3: IPF orientation maps of the 45 oriented sample, corresponding to a) the initial state, i.e., preloaded to 7 MPa, b) the state after loading to 77 MPa, c) the state after loading to 106 MPa, d) the state after loading to 129 MPa and e) the state after loading to 170 MPa. The colour legend shown in a) is the same for all of the figures. The sample was compressed in the horizontal direction.

6.2 Schmid factor maps

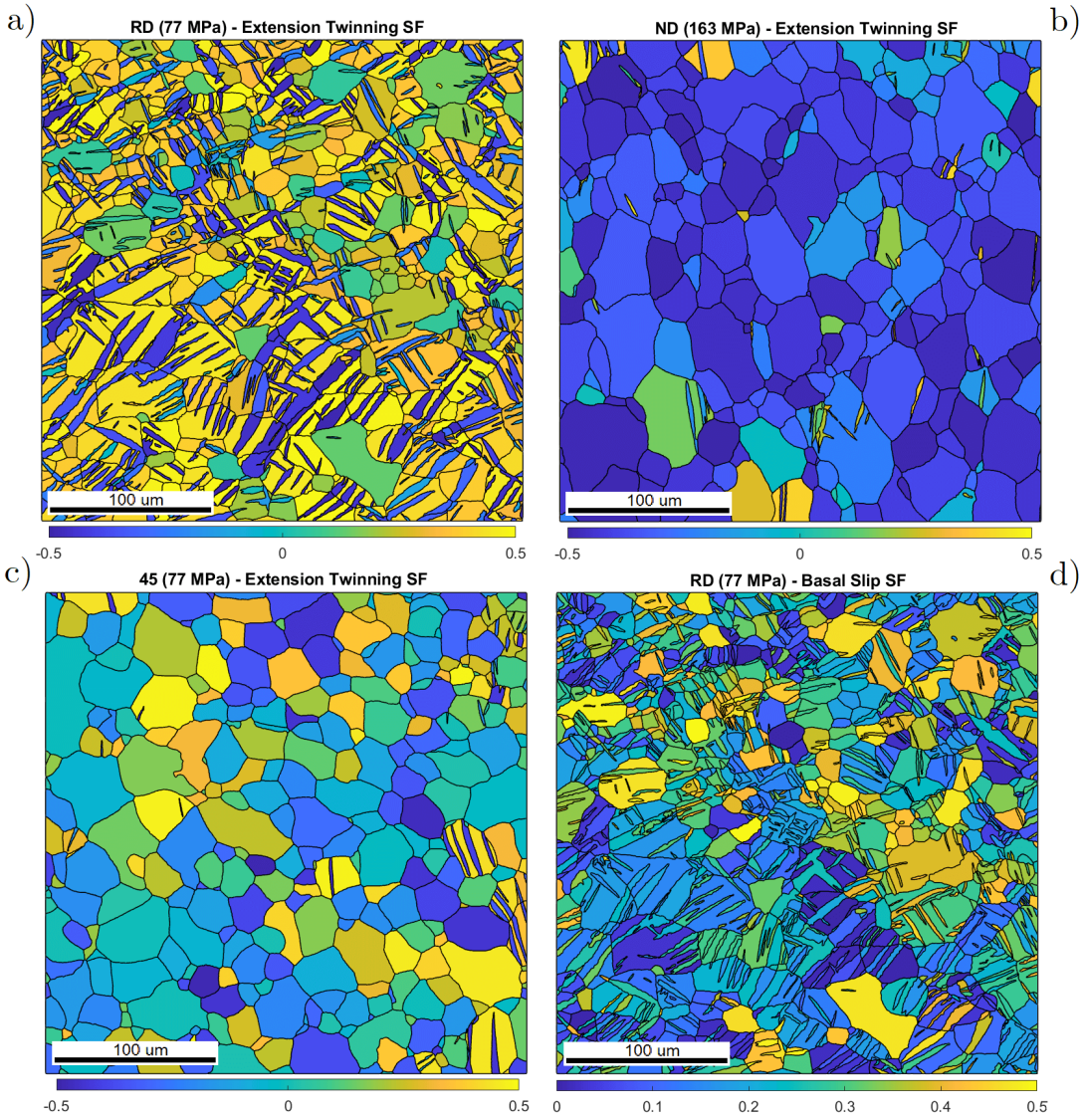

Figure 6.4: Schmid factor maps for a) extension twinning in the RD sample loaded to 77 MPa, b) extension twinning in the ND sample loaded to 163 MPa, c) extension twinning in the 45 sample loaded to 77 MPa and d) basal slip in the RD sample loaded to 77 MPa. The displayed values correspond to compression in the horizontal direction.

6.3 Twin parent-daughter maps

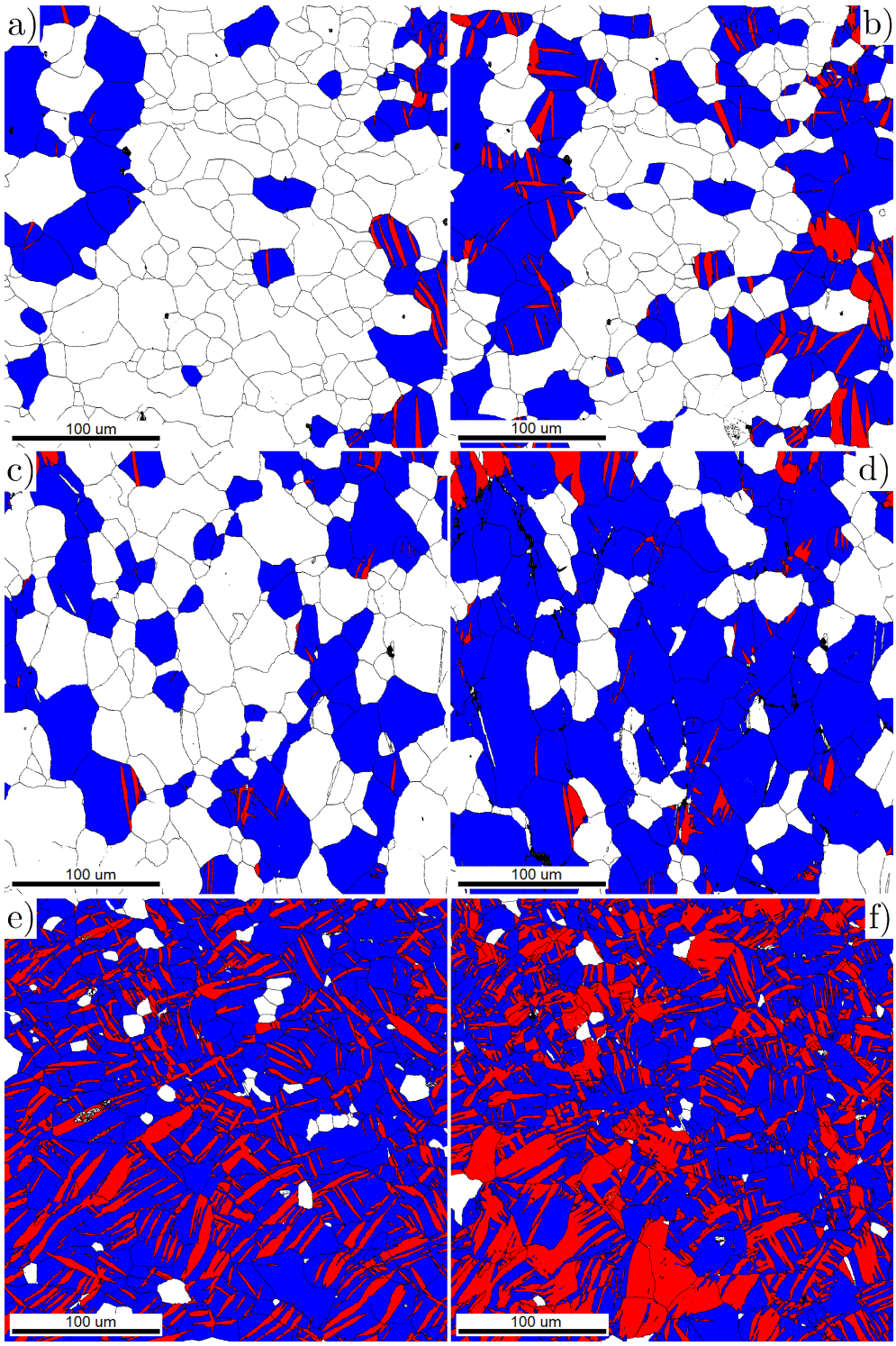

Figure 6.5: Twin parent-daughter relation maps of the a) 45 sample loaded to 77 MPa, b) 45 sample loaded to 106 MPa, c) ND sample loaded to 163 MPa, d) ND sample loaded to 206 MPa, e) RD sample loaded to 77 MPa and f) RD sample loaded to 102 MPa. Blue areas correspond to twin parents, red areas to twin daughters and white areas to untwinned grains. The samples were compressed in the horizontal direction.

6.4 High-speed camera images

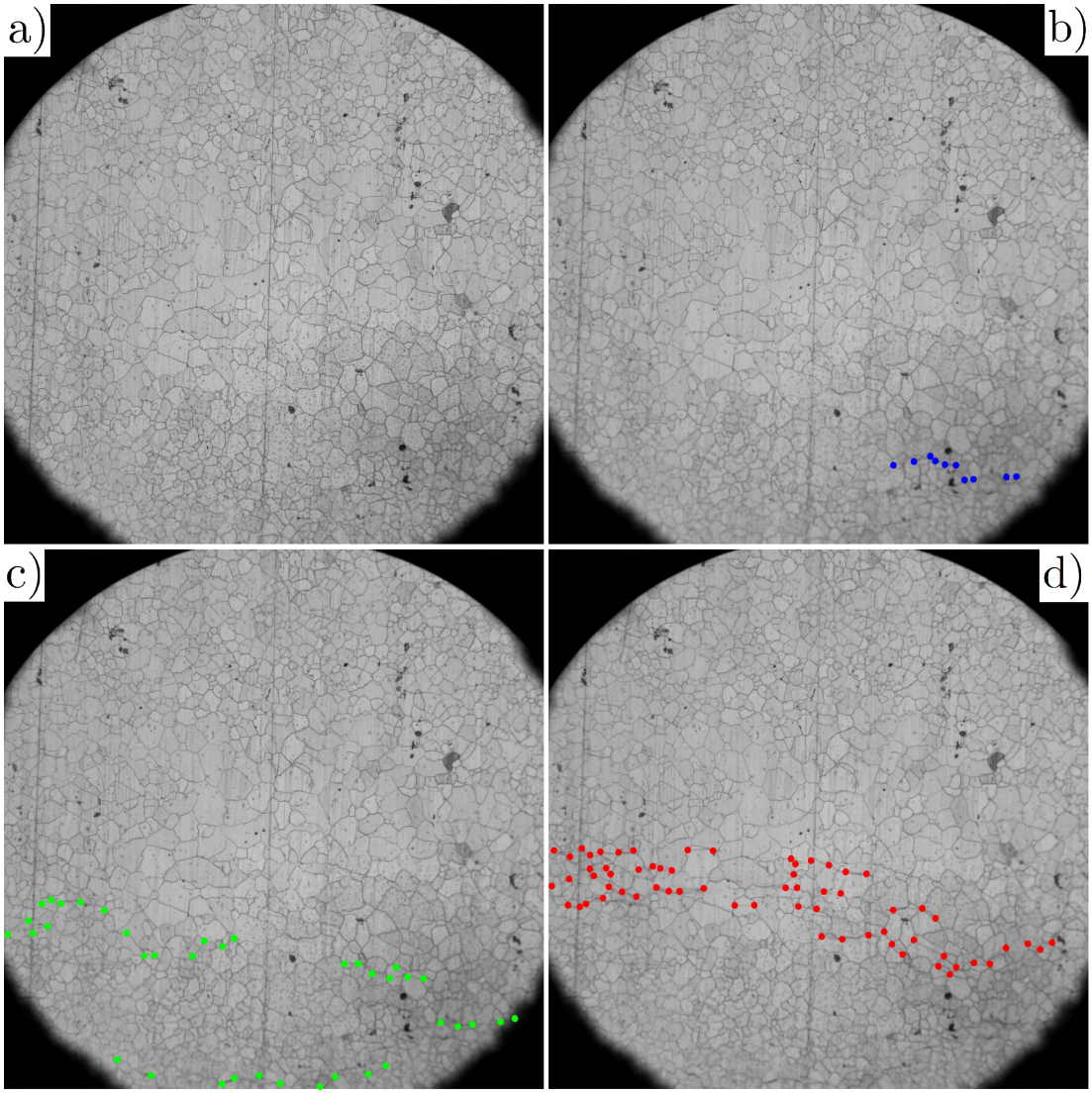

Figure 6.6: High-speed camera images of the RD sample depicting a) the sample initial state, i.e., preloaded to ca. 16 MPa, b) the sample loaded to 72 MPa with the first nucleated twins indicated by blue markers, c) the sample loaded to 73 MPa with the newly nucleated twins indicated by green markers and d) the sample loaded to 73 MPa with a band of newly nucleated twins indicated by red markers. The sample was compressed in the vertical direction.

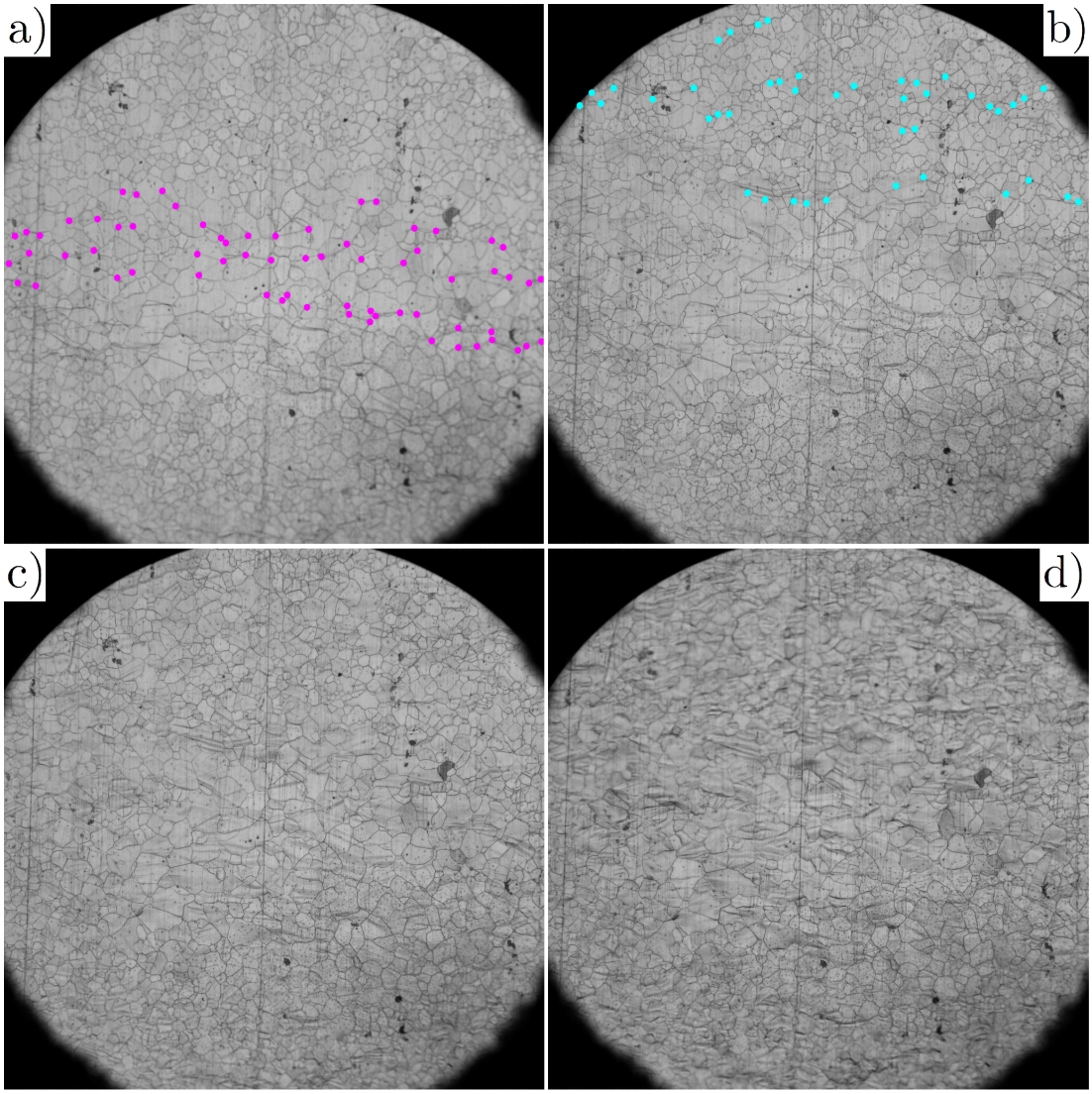

Figure 6.7: High-speed camera images of the RD sample depicting a) the sample loaded to 75 MPa with the newly nucleated twins indicated by purple markers, b) the sample loaded to 81 MPa with the newly nucleated twins indicated by cyan markers, c) the sample loaded to 103 MPa and d) the sample loaded to ca. 165 MPa. The sample was compressed in the vertical direction.

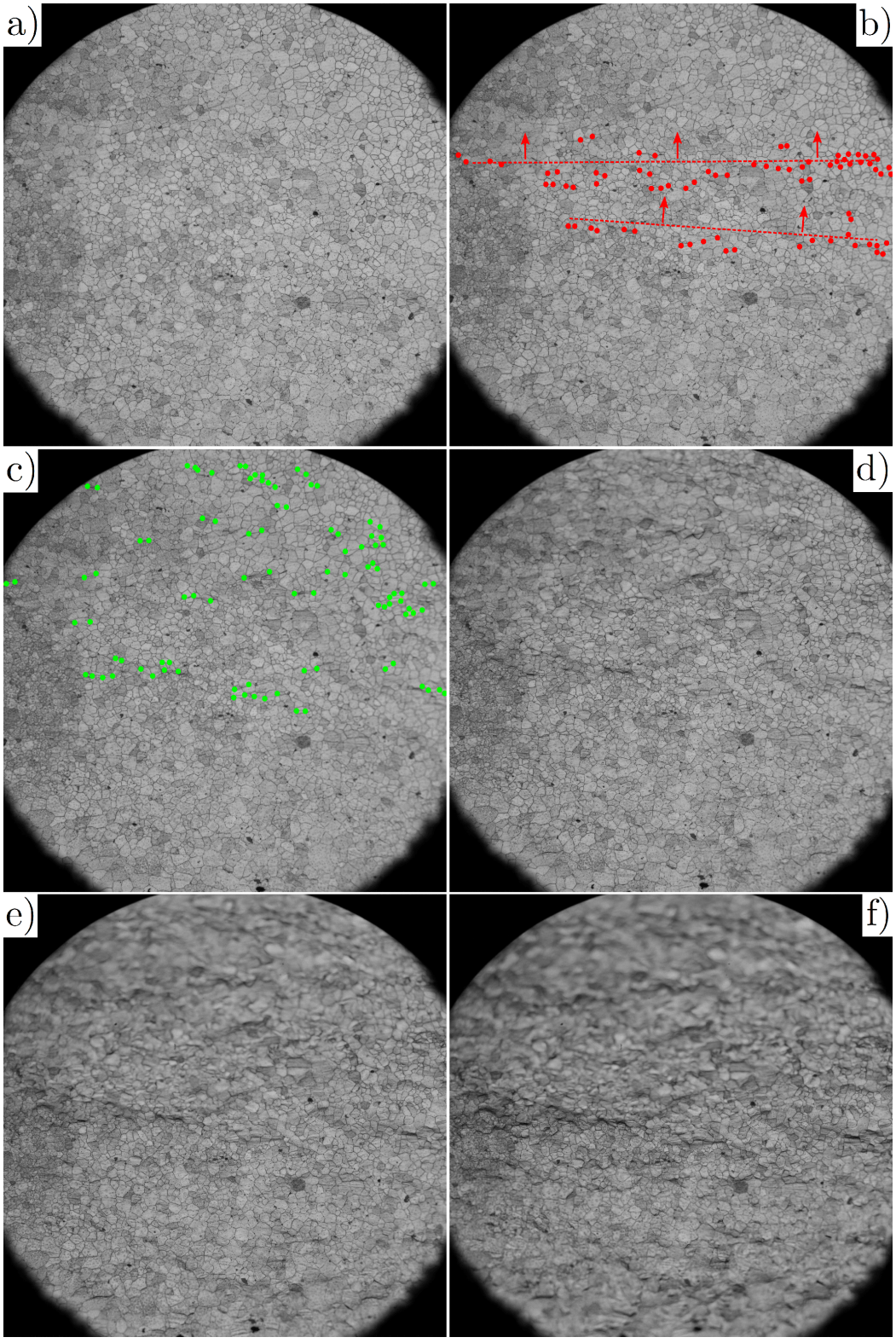

Figure 6.8: High-speed camera images of the 45 sample depicting a) the sample state in the elastic region loaded to 43 MPa, b) the sample loaded to 65 MPa with the newly nucleated twins indicated by red markers and indicated material movement by red lines and arrows, c) the sample loaded to 73 MPa with the newly nucleated twins indicated by green markers, d) the sample loaded to 97 MPa, e) the sample loaded to 121 MPa and f) the sample loaded to 147 MPa. The sample was compressed in the vertical direction.

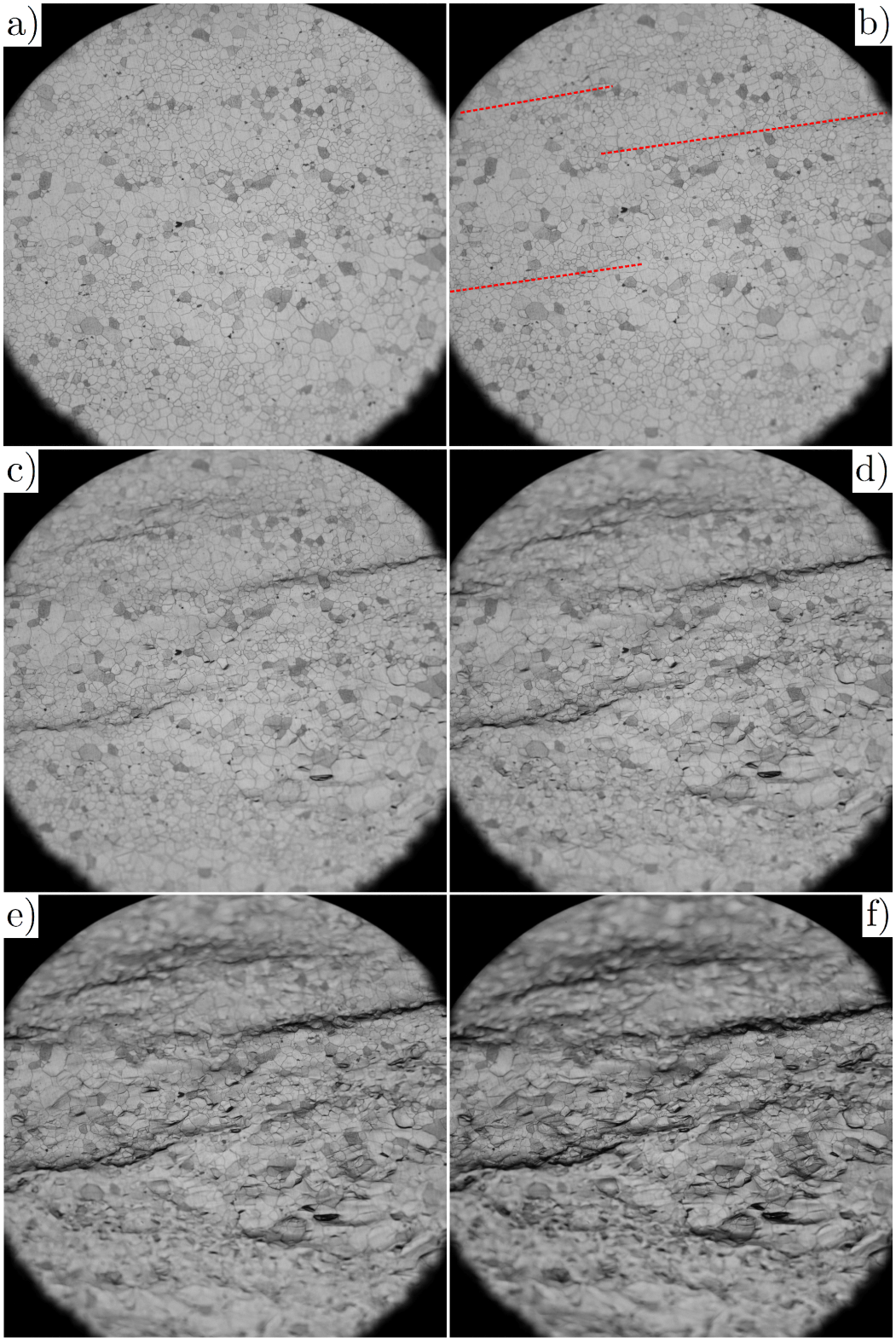

Figure 6.9: High-speed camera images of the ND sample depicting a) the sample state in the elastic region loaded to 73 MPa, b) the sample loaded to 178 MPa with the boundaries of deformation bands marked by red dashed lines, c) the sample loaded to 204 MPa, d) the sample loaded to 218 MPa, e) the sample loaded to 228 MPa and f) the sample loaded to 236 MPa. The sample was compressed in the vertical direction.